

918
NONEQUILIBRIUM RADIATION AND CHEMISTRY MODELS

FOR AEROCAPTURE VEHICLE FLOWFIELDS



aerospace engineering department

Semiannual Progress Report
January 1990 -- June 1990

TEXAS A&M UNIVERSITY

TAMRF Report No. 6382-90-02

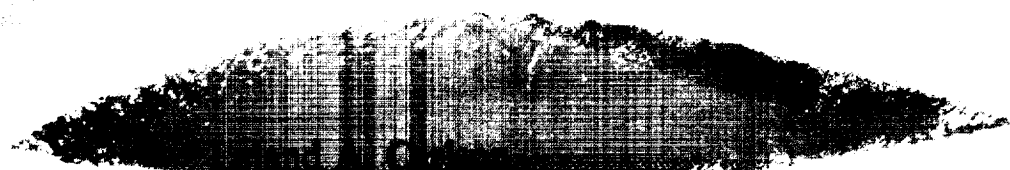
June 1990

(NASA-CR-186728) NONEQUILIBRIUM RADIATION
AND CHEMISTRY MODELS FOR AEROCAPTURE VEHICLE
FLOWFIELDS Semiannual Progress Report, Jan.
- Jun. 1990 (Texas A&M Univ.) 91 pCSCL 200

N90-27973

Unclas
H1/34 0291061

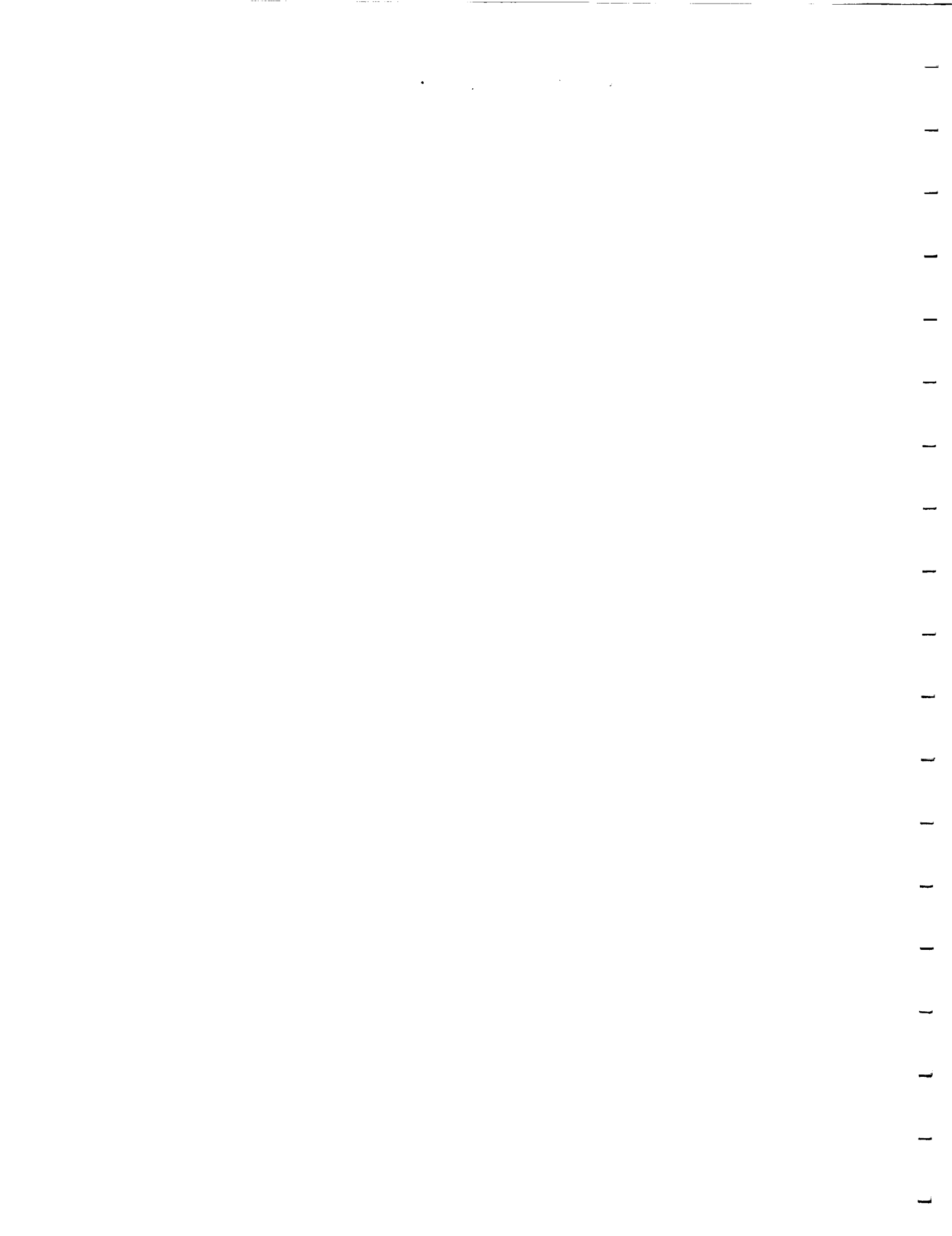
NASA Grant No. NAG-1-1003



Professor of Aerospace Engineering
Texas A&M University
College Station, Texas 77843-3141



TEXAS ENGINEERING EXPERIMENT STATION



**NONEQUILIBRIUM RADIATION AND CHEMISTRY MODELS
FOR AEROCAPTURE VEHICLE FLOWFIELDS**

**Semiannual Progress Report
January 1990 -- June 1990**

**TAMRF Report No. 6382-90-02
June 1990**

NASA Grant No. NAG-1-1003

**Leland A. Carlson
Professor of Aerospace Engineering
Texas A&M University
College Station, TX 77843-3141**

NONEQUILIBRIUM RADIATION AND CHEMISTRY MODELS FOR AEROCAPTURE VEHICLE FLOWFIELDS

I. Introduction

This report covers approximately the period January 1990 thru June 1990. The primary tasks during this period have been the development and evaluation of various electron and electron-electronic energy equation models, the continued development of improved nonequilibrium radiation models for molecules and atoms, and the continued development and investigation of precursor models and their effects. In addition, during this period work has been initiated to develop a vibrational model for the viscous shock layer (VSL) nonequilibrium chemistry blunt body engineering code. Also, an effort has been started associated with the effects of including carbon species, say from an ablator, in the flowfield. It should be noted that the individuals involved with these last two efforts, while associated with the project, are currently supported by the department.

II. Personnel

The staff associated with this project during the present reporting period have been Dr. Leland A. Carlson, Principal Investigator, and Thomas A. Gally and Scott Stanley, Graduate Research Assistants. It should be noted that Mr. Gally is currently supported by a NASA Graduate Student Researchers Fellowship from NASA Johnson Space Center and will use the results of his research on this project in his PhD dissertation. Mr. Stanley, who is supported entirely by this project, will use the results of his research for his masters thesis. In addition, two additional graduate students, Derek Green and Rajeev Koteswarar, have recently initiated their masters' research work in areas associated with the project. Currently, they are supported by departmental funds; but outside support will have to be found in the near future.

III. Electron Energy Modeling

In the results presented in the previous progress report and in Appendix I of this report, the electron temperature was determined using a quasi-equilibrium free electron equation; and the electronic temperature was assumed to be equal to the free electron temperature. While it is believed that this approach is a good approximation for most conditions of interest in aerocapture, efforts have continued to improve the modeling of electron energy, and hence temperature, due to its importance in determining nonequilibrium ionization chemistry and radiative transfer. Specifically, studies are currently in progress using a combined electron-electronic energy differential equation which includes the effects of convection, conduction, and diffusion in addition to the production and loss of electron energy through elastic and inelastic collisions. The current full electron-electronic energy equation for the stagnation line is

$$\rho u c_{pe} \frac{\partial T_e}{\partial n} - \frac{\partial}{\partial n} \left(\lambda_e \frac{\partial T_e}{\partial n} \right) - \left(\sum_i \rho D_i c_{pe_i} \frac{\partial c_i}{\partial n} \right) \frac{\partial T_e}{\partial n} - u \frac{\partial p_e}{\partial n} + \sum_i \dot{w}_i h_{e_i} = \sum_i \dot{z}_{e_i} + \dot{w}_{e,ea} E_I / m_e \quad (E-1)$$



where c_{pe} is defined as

$$c_{pe} = \frac{p_e}{\rho} c_{pe,e} + \sum_i c_{palec,i} \quad (E-2)$$

In this equation, the viscous work terms have not been included due to the fact that they are of lower order. In addition, radiation effects on electron-electronic energy have been neglected as has electron-vibrational coupling and diffusion effects on collisional energy exchange. The latter is expected to be small in most cases due to the rapid dissociation of N_2 and the assumption of ambipolar diffusion. However, it might be important at some of the lower AFE velocities.

It should be noted that Eqs. (E-1) is equivalent to that presented by Gnoffo (Ref. 1) and J. H. Lee (Ref. 2). However, it differs slightly from that presented in Ref. (3 and 4) in that the latter contains the additional terms

$$\dot{W}_e \frac{u^2}{2} + U_e \frac{\partial p_e}{\partial n}$$

which arise as a result of the differences in the derivation of the species energy and momentum equations. It is believed that these additional terms occur as a result of using the more detailed approach of Chapman and Cowling (Ref. 5), and an outline of the derivation is shown in Appendix II. In any event, these two terms are expected to be small, and their neglect in the present study should not affect the results.

This full electron equation is included in the VSL solution sequence at the same location as the algebraic quasi-equilibrium electron equation was previously; and, after linearizing the right hand side and finite differencing along the normal coordinate, the resulting set of tridiagonal equations can be solved for the electron temperature. While this procedure is convergent, methods to improve the convergence rate are under investigation.

Results comparing temperature profiles computed with the quasi-equilibrium method with those obtained using the full electron equation are presented for a series of velocities on Figures 1 thru 4. These results, which do not include radiation cooling or coupling, indicate that the primary effect of using the full electron equation is to slightly delay the rise in electron temperature and to move the location of peak electron temperature to a position slightly further from the shock front.

One of the advantages of the new full equation formulation is that in the wall thermal layer the addition of the convection, conduction, and diffusion terms interact with the collisional terms to maintain the electron temperature equal to the translational temperature. In the quasi-equilibrium approach this expected behavior was not directly achieved but was forced by requiring T_e to be less than or equal to heavy particle translational temperature.

As shown on Figure 4, the full electron equation result for 8.915 km/sec is considerably different and cooler than the profile predicted by the quasi-equilibrium method. While



this result is still under investigation, it could be due to the low degree of ionization for this case and the subsequent dominance of the electronic portion of the equation. In evaluating this result, it should be noted that the present results do not yet include vibration electronic coupling or photochemistry effects on electron electronic temperature, which could change this particular profile.

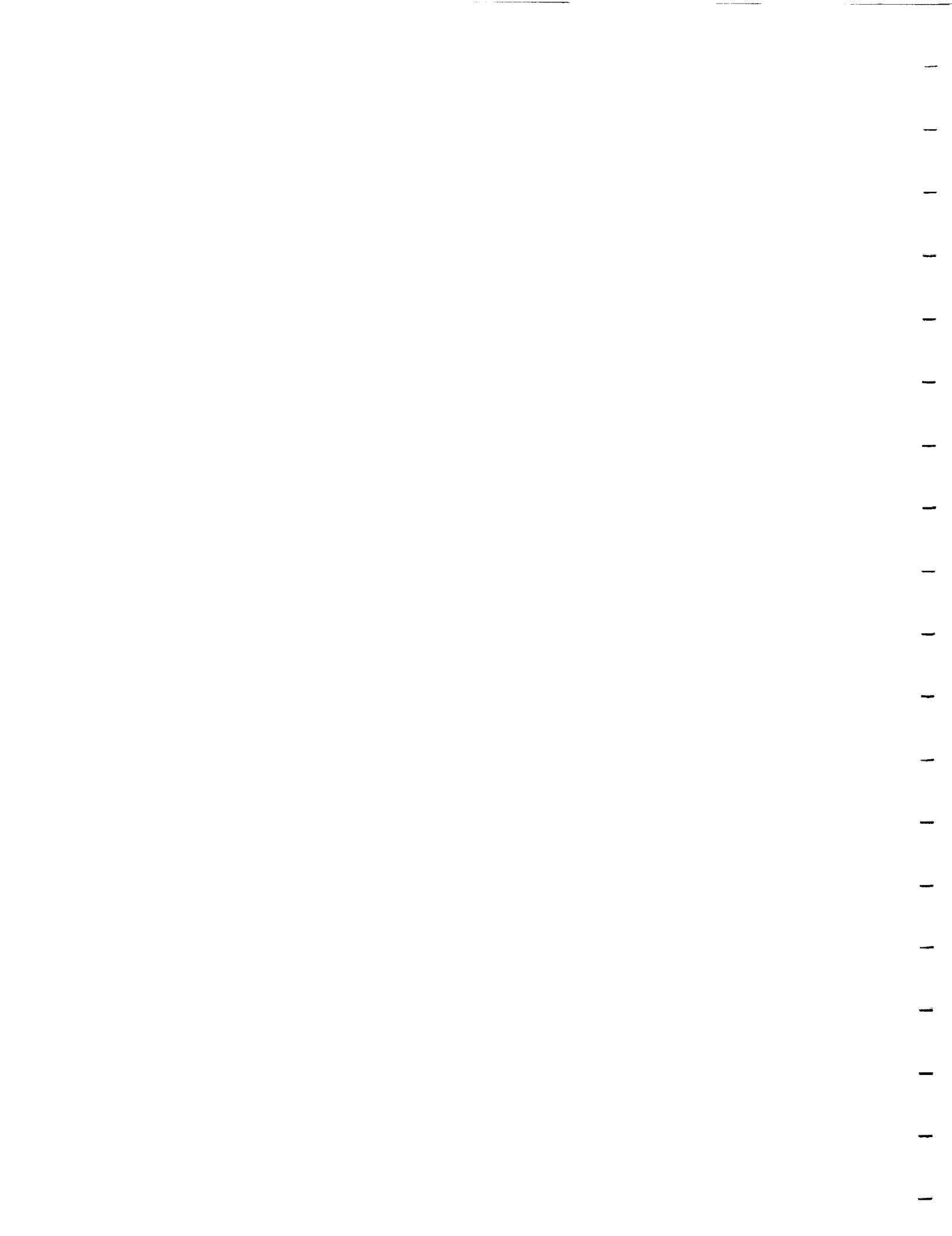
It is believed that considerable progress has been made during this reporting period in electron-electronic energy modeling. However, efforts will continue to improve it. In particular, studies are in progress to determine the importance of diffusion in collisional energy exchange, to assess the magnitude of photochemistry processes in the shock layer, to improve the solution scheme, and to include electron vibration coupling.

IV. Nonequilibrium Molecular Radiation Models

In the present engineering approach, nonequilibrium radiation is computed by using the RADICAL radiative analysis code and absorption coefficient model with actual species concentrations and correction factors to account for local thermodynamic nonequilibrium effects (LTNE), i.e. non-Boltzmann state populations. Previously, approximate correction factors for molecular radiation had been developed by Greendyke et al (Ref. 6). However, as alluded to in the last progress report, it is now believed that these approximate factors overcorrect and underestimate the actual molecular radiation. This belief is reinforced by the fact that experimental measurements made in molecular radiation dominated shock flows show a radiation intensity peak behind the shock in conjunction with the predicted electron temperature peak. Thus, significant depletion of the excited molecular states, as predicted by the theory of Ref. 6, is not expected. Consequently, it was decided to develop new improved molecular correction factors for molecular nonequilibrium radiation.

After examining various approaches, a quasi-steady approach similar to that of Park (Ref. 7) has been developed which computes the electronic state populations associated with the radiating bands. Specifically, for N_2 , the populations of the X, A, B, a, and C states are computed; while for N_2^+ the X, A, B, and D are included. This approach has been developed and incorporated into the VSL code and is currently being tested. Note that there is no assumption concerning the existence of equilibrium between excited states and atoms as there was in the original factors. Thus, in this new model, both source functions and absorption coefficients associated with molecular band radiation will have corrections factors.

The resultant molecular correction factors for the stagnation streamline of a 230 cm nose radius vehicle entering at 12 km/sec at 80 km are shown on Figures 5 and 6. This case was selected because almost the entire shock layer is in chemical nonequilibrium and a significant portion is in thermal nonequilibrium. Considering that unity implies no correction, it can be seen that for the N_2 Birge-Hopfield band the correction for the absorption coefficient is minor but that for the corresponding source function is quite large in the nonequilibrium portion of the shock layer immediately behind the shock front. This behavior is what would "normally" be expected since $N_2(BH)$ involves absorption to the ground state. Likewise $N_2(1+)$ displays only a slight correction for the source function but a significant change in the absorption coefficient (from Boltzmann). This trend is also "expected" since $N_2(1+)$ involves the two excited states B and A. On the other hand, while the absorption coefficient factor for $N_2(2+)$ is similar to that for $N_2(1+)$, the source factor for $N_2(2+)$ is significantly small in the chemical and thermal nonequilibrium region behind



the shock front, indicating that pre-dissociation is significantly depleting the population of the C electronic state.

The most interesting result, however, is that the $N_2(1-)$ radiation is only slightly affected by nonequilibrium phenomena, with the correction factors being essentially unity, or in the case of the source function, slightly above unity. This lack of correction is in agreement with experiments which, at least at lower velocities, have indicated a strong $N_2(1-)$ contribution. However, the results on Figs. 5-6 for N_2+ are somewhat deceiving in that the number density of N_2+ is only significant in the region immediately behind the shock front ($0.9 < x/L < 1.0$) where the electron temperature is still increasing. Thus, most of the $N_2(1-)$ radiation originates from the region immediately behind the shock front.

Figure 7 compares, for the 12 km/sec 80 km case, the continuum radiation to the wall with and without the molecular nonequilibrium radiation corrections. (The dashed line is the result including molecular LTNE corrections.) While atomic line radiation has been included in the calculation, the plot only shows the atomic and molecular continuum for clarity; and, as can be seen, the primary effect of nonequilibrium is to essentially eliminate the $N_2(BH)$ contribution between 6.5 eV and 12.77 eV, leaving primarily only atomic continuum radiation in that region. Also, nonequilibrium reduces the $N_2(1+$ and $2+)$ bands between .75 and 4.5 eV; although, the essentially unaffected $N_2(1-)$ emission dominates this region. It should be noted that these trends are in agreement with the Fire II flight data which detected molecular radiation, particularly from the $N_2(1+$ and $2+)$ bands, significantly below values predicted assuming local thermodynamic equilibrium.

Another interesting phenomena displayed on Figures 5 and 6 is that in the thermal boundary layer near the wall, several of the factors exceed unity and become large. This behavior indicates an overpopulation of excited states above values which would be predicted by a Boltzmann distribution when intuitively an equilibrium distribution would be expected due to the increased density near the wall. However, in actuality, the thermal boundary layer is in significant nonequilibrium in that the chemical reaction rates are finite and cannot keep up with true local equilibrium, which leads to atom and ion concentrations above equilibrium. In addition, diffusion tends to perturb the species population densities and also leads to atom and ion densities above equilibrium values, which in turn leads to enhanced molecular excited state populations. This enhancement, however, does not lead to increased radiative emission near the wall; and, in fact, probably due to the low electron-electronic temperature in that region, it does not appear to affect the wall radiative heat transfer.

A significant question, of course, is how important is molecular radiation at 12 km/sec since originally it was believed that molecular radiation would be unimportant at this condition. Radiation uncoupled stagnation point results obtained using the present method with various nonequilibrium radiation assumptions are given in Table I.

Obviously, molecular radiation at this condition, while small, comprises about fifteen percent of the total and should be included in predictions; and molecular LTNE effects slightly reduce the molecular contribution. Thus, the suggestion in the last report that for AFE conditions a conservative prediction could be obtained by including both molecular and atomic radiation but utilizing only atomic LTNE corrections appears to be a reasonable approach.

(At this point, it should be noted that the value listed in Table I for the the case including only atomic radiation with LTNE corrections is slightly higher than values listed for the same condition in the last report. Since that time, an error in the radiative analysis portion of the code which was introduced during the modifications to include LTNE effects has been discovered and corrected. It is planned to recompute the cases presented in the last report in the near future.)

Results using the new electron-electronic energy and the new nonequilibrium radiation molecular formulations have also been obtained for the 16 km/sec, 80 km case, and temperature and ionization profiles for uncoupled and radiatively coupled cases are presented on Figures 8 and 9. For this case, chemical and thermal nonequilibrium phenomena dominate the outer thirty-five percent of the shock layer; and, as can be seen by comparison of the two results, radiation cooling significantly cools and changes the chemistry in the remainder of the shock layer. Stagnation point radiative transfer predictions obtained with these new models are presented in Table II.

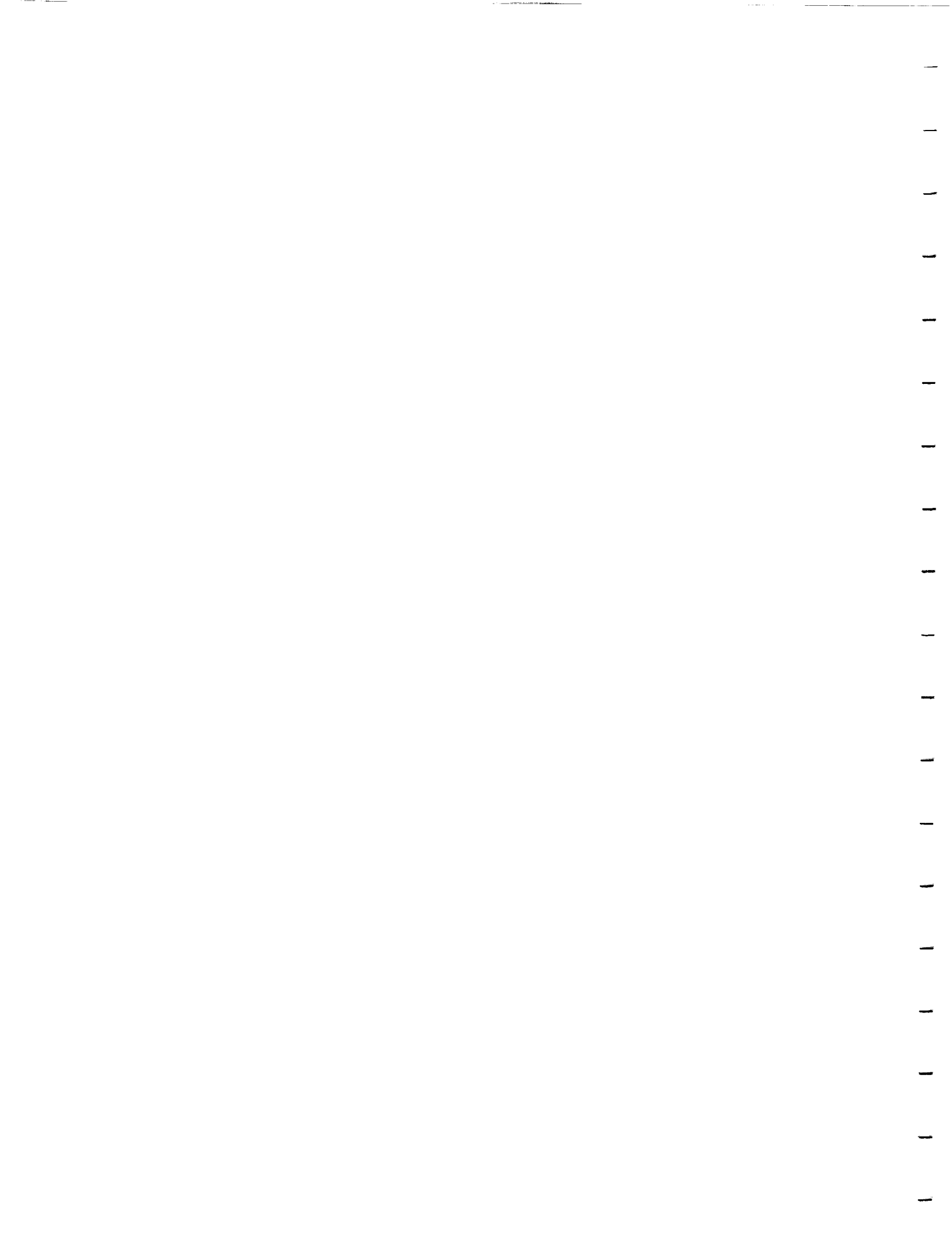
Comparison of these results indicates that at this condition molecular radiation is insignificant and probably could be neglected in approximate calculations. However, radiation coupling and cooling is very important and needs to be included in any radiative heating predictions at this condition.

Results using the new molecular correction approach have also been obtained for AFE CFD Points 2 and 4, and stagnation point radiative heat transfer results for various cases are presented in Tables III and IV. However, due to the uncertainty of the applicability of the full electron-electronic energy equation in its present form to these conditions, these results have been obtained using the quasi-equilibrium electron energy equation formulation. In addition, unlike the results at higher velocities, these required limitations on the molecular LTNE factors at the computational point adjacent to the wall. As mentioned elsewhere, diffusion phenomena appear to be causing excessive atom concentrations in that region. As a result, investigations of the present diffusion model in the VSL code are currently in progress.

As can be seen, radiation cooling effects in both of these cases is small; and the inclusion of molecular LTNE corrections does reduce the radiative heating, which for these low speed conditions is primarily molecular. Finally it should be noted, that these values are similar to those reported in the last progress report.

V. Nonequilibrium Atomic Radiation Models

In the results obtained to date, local thermodynamic nonequilibrium effects (LTNE) on atomic radiation have been computed by applying correction factors to the absorption coefficient and source function values computed by the radiative analysis code RADICAL. The current correction factors are what should probably be termed first order approximations, and their form and the logic behind them is given in References 3, 6, and 8. Briefly, these factors assume that atomic ionization proceeds by excitation from the three low ground states to the high excited states followed by rapid ionization. Consequently, the model assumes that excitation from the ground states to the higher states is a rate limiting step for the ionization process and that the excited states, because of their energy proximity to the ionized state, are in equilibrium with the free ions and electrons.



In contrast, Park (Ref. 7 and 9) and Kunc et al (Ref. 10) handle LTNE by using a quasi-steady analysis in which, while rate processes between all the bound states and between the bound states and the ionized state are assumed finite, they are assumed to be fast relative to changes induced by the flowfield. Thus, at any point in a flowfield an equilibrium between the states will exist which is perturbed from a Boltzmann distribution due to radiative effects. Kunc et al have performed calculations in which they specify the electron temperature and the total number of charged particles (defined as 2 times the number of atoms plus the number of ions plus the number of electrons), leaving the actual number of ions and free electrons to be determined as part of the unknown populations.

Park, on the other hand, in the application of his method assumes the number of ions and electrons to be given by a flowfield solution (Ref. 9). Under this approach, a non-Boltzmann distribution can be achieved even in the absence of radiation, if the number of ions and electrons differs from equilibrium. To be totally correct, however, the excitation and ionization rates associated with each level must overall be consistent with the ionization rate used in the flowfield solution.

Obviously, the present approach and those of Park and Kunc et al represent the extremes of modeling LTNE atomic phenomena. Unfortunately, the present approach is overly simplified in its assumptions that the rates between the excited states and the free ions and electrons are infinitely fast (i.e. local equilibrium); and the detailed quasi-steady approaches are computationally intensive because they include a large number of electronic levels. In addition, the latter are sensitive to the choice of the individual rates; and it is difficult to know which rate to adjust when comparing with experimental results and attempting to improve the correlation. Consequently, work has been initiated during this reporting period on an improved LTNE atomic model.

After extensively reviewing the work on argon of Foley and Clarke (Ref. 11), Nelson (Ref. 12), etc. and the air and nitrogen work of Park (Ref. 7), Kunc and Soon (Ref. 10), and others, it has been decided to model high temperature nitrogen by subdividing atomic nitrogen into two species. The first, termed Ng, for N ground, represents the nitrogen atoms in the first three low lying electronic states of nitrogen. The second, termed N* or N excited, represents those nitrogen atoms populating the remaining upper electronic states. The relative densities of these subspecies will then be determined by appropriate reaction rates between themselves, N+, e-, etc. It is believed that this approach will be a significant improvement over the present model in that it will allow a finite rate of ionization from excited states while retaining the fundamental two step ionization process. In addition, by determining the excited state number densities directly from the flowfield computation, the appropriate atomic LTNE factors should be "directly" obtainable and more accurate.

Initially, it is planned to use the collisional reaction rate system shown in Table V. In general, reaction rates for the first seven reactions are well known. However, the rates for the electron-atom excitation and electron-atom ionization reactions, numbers 8 - 10, need to be determined. Currently, atom-atom excitation and photo-excitation photo-ionization are not included since it is believed that these reactions are of second order in the stagnation region. However, it is planned to include them later.

In this system, care must be taken to properly formulate the species enthalpy of Ng and N*. Specifically,



$$h_{N_g} = \frac{5}{2} \frac{kT}{m_a} + \frac{\sum_{l=1}^3 g_l \frac{E_l}{k} e^{-E_l/kT_e}}{\sum_{l=1}^3 g_l e^{-E_l/kT_e}} \frac{k}{m_a} + h_{N_g}^0 \quad (A-1)$$

$$h_{N^*} = \frac{5}{2} \frac{kT}{m_a} + \frac{\sum_{l=4}^{MAX} g_l \frac{E_l - E_4}{k} e^{-(E_l - E_4)/kT_e}}{\sum_{l=4}^{MAX} g_l e^{-(E_l - E_4)/kT_e}} \frac{k}{m_a} + h_{N^*}^0 \quad (A-2)$$

where

$$h_{N_g}^0 = 3.36 \times 10^{11} \text{ ergs/gm}$$

$$h_{N^*}^0 = 1.05 \times 10^{12} \text{ ergs/gm}$$

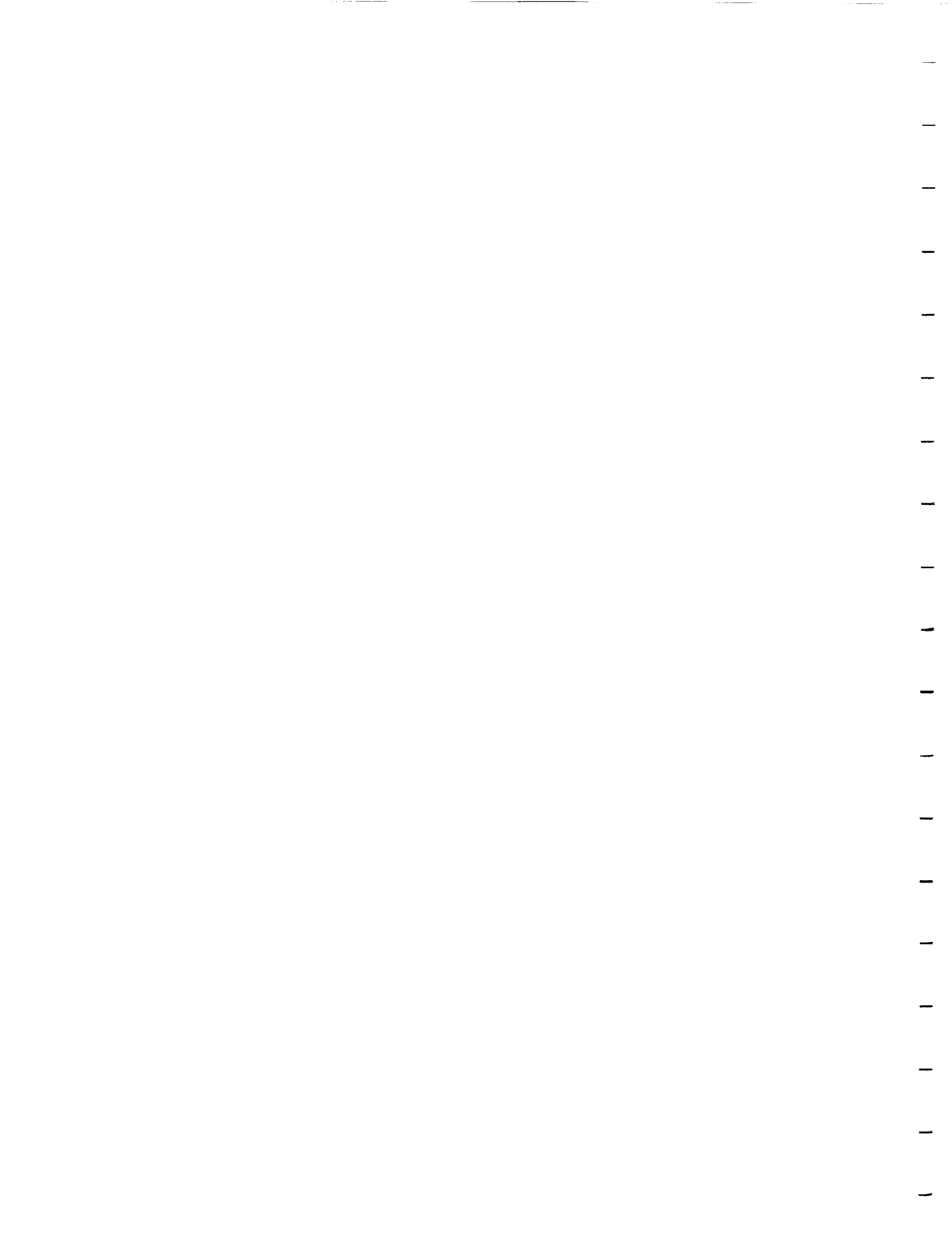
$$E_4 = 83337 \text{ cm}^{-1}$$

For equilibrium conditions, these expressions reduce to the proper forms where

$$h = \sum_{i=1}^S \frac{P_i}{P} h_i \quad (A-3)$$

As mentioned above, effective reaction rates have to be obtained for reactions (8) - (10). While in principle, these could be extracted from the work of Park (Ref. 13), the work in Ref. 10) appears to contain information based upon more recent data. Furthermore, it appears to yield excitation rates more compatible with relaxation data behind shock waves. Consequently, a method has been developed and a computer program written to determine from the detailed data of Ref. 10, effective forward rates for reactions (8)-(10). While complete details of the method and results will be presented later, a preliminary set of results is presented in Figure 10.

Also shown on Figure 10 is the rate of Wilson successfully used in Ref. 3 in conjunction with the first order LTNE model. As can be seen the preliminary rates for the new model are faster for excitation from the ground state but are finite for ionization from the



excited state to the continuum. Thus, they appear to have the right trend and magnitude. In addition, included on the figure is the effective ionization rate from the ground state directly to the continuum. As previously postulated, this rate is considerably slower than the excitation rate. Finally, the ground to excited forward rate is about two orders of magnitude slower than that which it is believed would be obtained from using the detailed rates in Ref. 13.

Currently, various methods of curve fitting these rates and incorporating them into the radiation coupled nonequilibrium VSL code are being investigated. It is anticipated that the results of these studies will be reported in the next progress report.

Once the chemistry model involving excited species has been developed, the next step is to determine the appropriate LTNE factors which should be utilized in the radiative analysis code. Considerable progress has been made in obtaining these factors during this period. However, since they are still under development and being "checked", the results which follow should be considered preliminary. The derivation of these factors will be presented at a later date.

For continuum processes involving absorption by an excited state, the absorption coefficient factor is

$$\frac{N_{N^*}}{N_N} = \frac{Q_{N_g}^{elec} + Q_{N^*}^{elec} e^{-E_4/kT_e}}{Q_{N^*}^{elec} e^{-E_4/kT_e}}$$

and the factor on the source function is

$$\frac{N_e N_{N^*}}{N_{N^*}} = \frac{Q_{N^*}^{elec} e^{(I-E_4)/kT_e}}{Q_{N^*}^{elec} Q_e}$$

Similarly, for continuum absorption involving a "ground" state, the absorption LTNE factor is

$$\frac{N_{N_g}}{N_N} = \frac{Q_{N_g}^{elec} + Q_{N^*}^{elec} e^{-E_4/kT_e}}{Q_{N_g}^{elec}}$$

and the corresponding source function factor is

$$\frac{N_e N_{N^*}}{N} = \frac{Q_{N_g}^{elec} e^{I/kT_e}}{Q_{N^*}^{elec} Q_e}$$



For line processes involving absorption into an excited state, the present theory yields an absorption LTNE factor of

$$\frac{N_{N^*}}{N_N} = \frac{Q_{N_g}^{elec} + Q_{N^*}^{elec} e^{-E_4/kT_e}}{Q_{N^*}^{elec} e^{-E_4/kT_e}}$$

while for this case the source function is unchanged. On the other hand, if the line process involves absorption into one of the ground states, the absorption factor is

$$\frac{N_{N_g}}{N_N} = \frac{Q_{N_g}^{elec} + Q_{N^*}^{elec} e^{-E_4/kT_e}}{Q_{N_g}^{elec}}$$

and the source function also has ^{the} factor

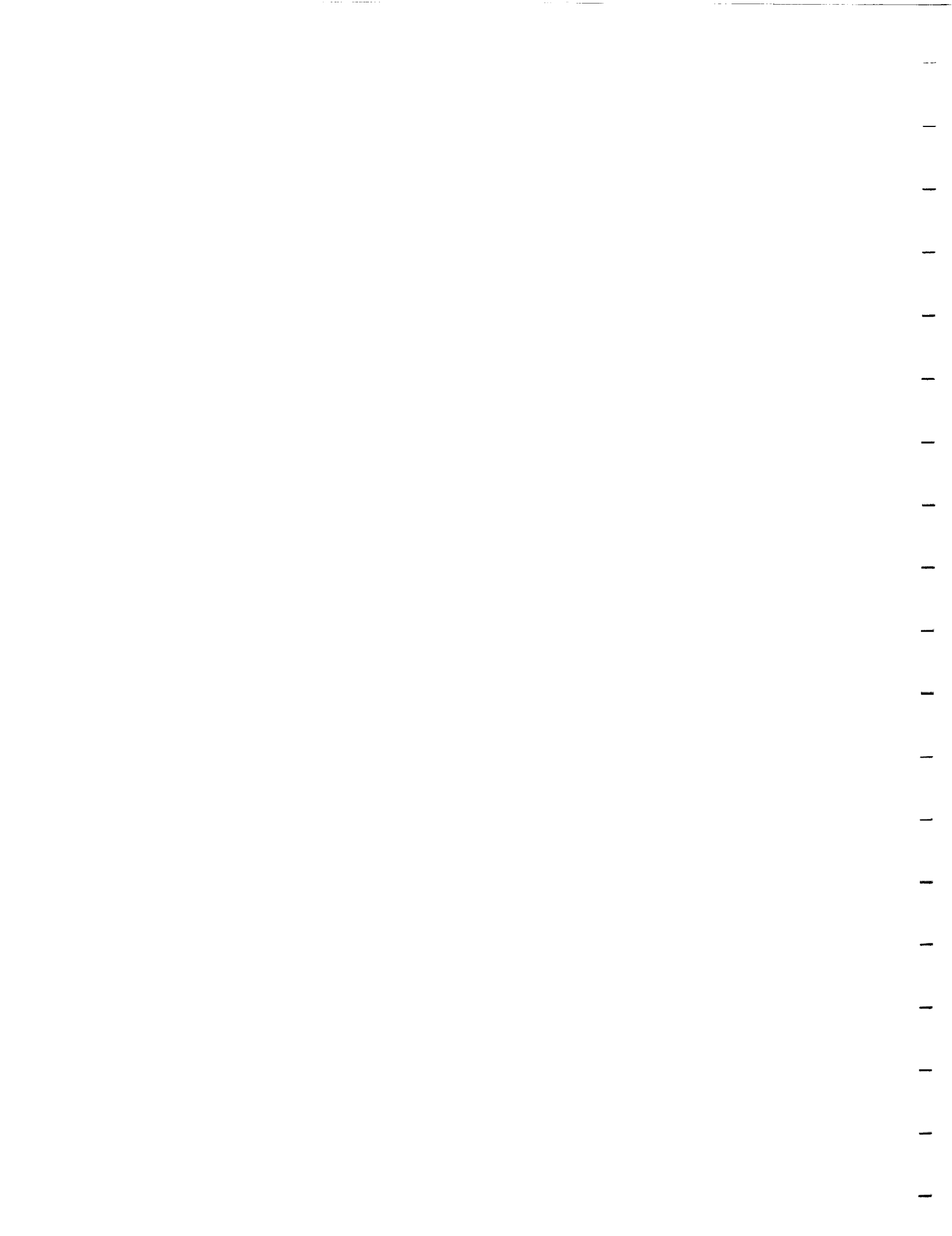
$$\frac{N_{N^*}}{N_{N_g}} = \frac{Q_{N_g}^{elec}}{Q_{N^*}^{elec} e^{-E_4/kT_e}}$$

It should be noted that if the N^* species is in equilibrium with N^+ and e^- and the number density of N_g is assumed to be that of N , these expressions reduce to those used with the first order model.

While the effects of using this new chemistry model and improved LTNE radiation model will not be known until they have been incorporated into the VSL code and extensively tested and compared to previous results, some preliminary studies of the effect of the LTNE factors have been conducted using temperatures and species densities previously obtained. These results indicate that the absorption factors are often larger than those obtained with the first order model. Since the new model has a faster excitation rate between ground and excited states and a finite rate between excited levels and the continuum, it should lead to higher population densities in the excited states. Thus, the preliminary results appear to have the correct trend. Consequently, it is quite possible that radiative heat transfer values obtained with the new LTNE model may be higher than those previously predicted. However, since these preliminary studies do not include the coupling effects on chemistry and flowfield profiles which different values of LTNE factors will induce, estimates of the magnitude of the change would be purely speculative at this time.

VI. Precursor Studies

As noted in the last progress report, precursor phenomena leads to the appearance ahead of the vehicle shock front of ionized species, free electrons, and thermal nonequilibrium each of which possibly might have an affect on the subsequent post-shock nonequilibrium phenomena. During this reporting period the effort to develop a good engineering model for precursor phenomena in nitrogen has continued and has led to



changes in the absorption coefficient model, improvements in the solution scheme, the development of appropriate radiation view factors, and the inclusion of electron thermal nonequilibrium.

Radiation View Factors

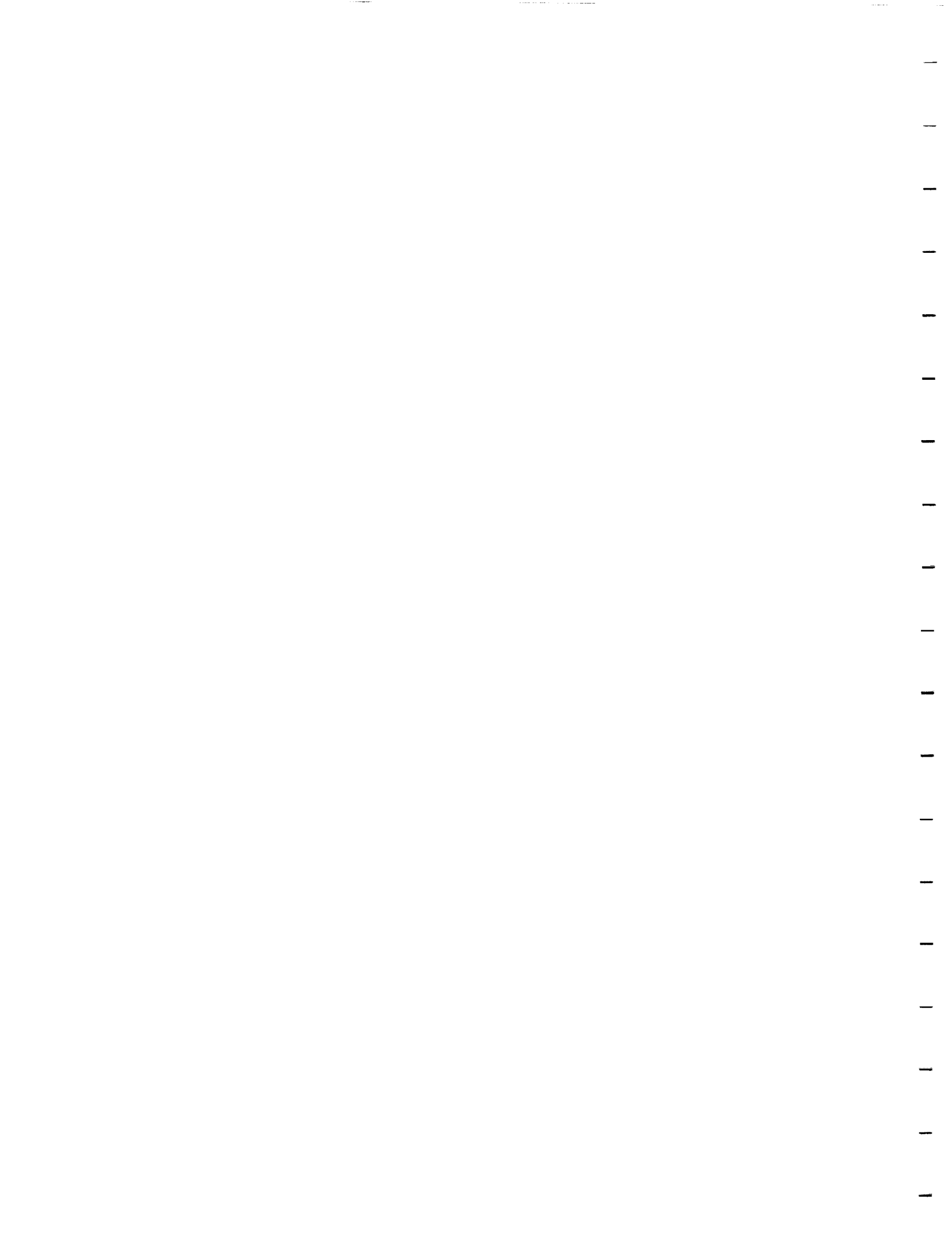
In computing shock layer radiative phenomena, the usual approach in engineering calculations is to use the tangent slab approximation. Since the ratio of shock layer thickness to vehicle radius or diameter is small, this approach is appropriate. However, in the precursor region ahead of the shock front, important phenomena occur at significant distances from the vehicle; and at those points the radiating shock layer about the vehicle only comprises a small portion of the spherical field of view. In other words, as the point of interest in the precursor moves away from the shock front, the shock and body do not appear to be infinite slabs; and the actual solid angle over which the radiation should be spacially integrated must be properly computed.

By assuming that there is no emission in the precursor, it can be shown that the appropriate radiation expression for a point in the precursor is

$$\dot{q}_{R_p} = -2\pi E_w B_{p,w} E_3(\gamma_p) \left[1 - \cos^2 \theta \frac{E_3(\gamma_p \sec \theta)}{E_3(\gamma_p)} \right] \\ - 2\pi \left(\int_0^{\gamma_s} E_2(\gamma_p - \gamma_s) d\gamma_s \right) \left[1 - \cos^2 \theta \frac{E_3((\gamma_p - \gamma_s) \sec \theta) - E_3(\gamma_p \sec \theta)}{E_3(\gamma_p - \gamma_s) - E_3 \gamma_p} \right] \quad (P-1)$$

where θ is one-half of the angle subtended by the body as viewed from the point in the precursor. The complete derivation of this expression will be given in detail at a later date.

It should be noted that Eq. (P-1) is essentially the tangent slab expression except that each term has been modified or corrected by a view factor depending upon vehicle size, location of the point of interest, and frequency. The typical magnitude and variation of these factors as a function of distance in front of the shock is shown on Figures 11 and 12. On this figure, the curve denoted "wall correction" refers to the view factor on the first term of Eq. (P-1) while that marked "shock layer correction" is the factor on the second term. Since it is anticipated that the radiation from the shock layer, rather than the "cool" wall, dominates the precursor phenomena, the present engineering precursor model utilizes the shock layer view factor on all terms as an approximation, i.e.



$$\dot{q}_{R_v} = A F_v \dot{q}_{R_v}^{TS} \quad (P-2)$$

where $A F_v$ is the view factor and $\dot{q}_{R_v}^{TS}$ is the total radiative flux at a point assuming a tangent slab.

In the energy equation, the term involving radiation appears as a divergence of the flux and is defined to account for the net absorption-emission at a point. However, simple differentiation of Eq. (P-2) would yield

$$A F_v \frac{\partial \dot{q}_{R_v}^{TS}}{\partial x} + \dot{q}_{R_v}^{TS} \frac{\partial A F_v}{\partial x} \quad (P-3)$$

In this expression, the first term is the change in the radiative flux due to absorption or emission, but the second term is the change due to geometry and should not be included in the energy equation. If it were included, an essentially transparent radiation would appear to be absorbed due to the spatial variation in the view factor. (Consider the case where \dot{q}_{R_v} is constant.)

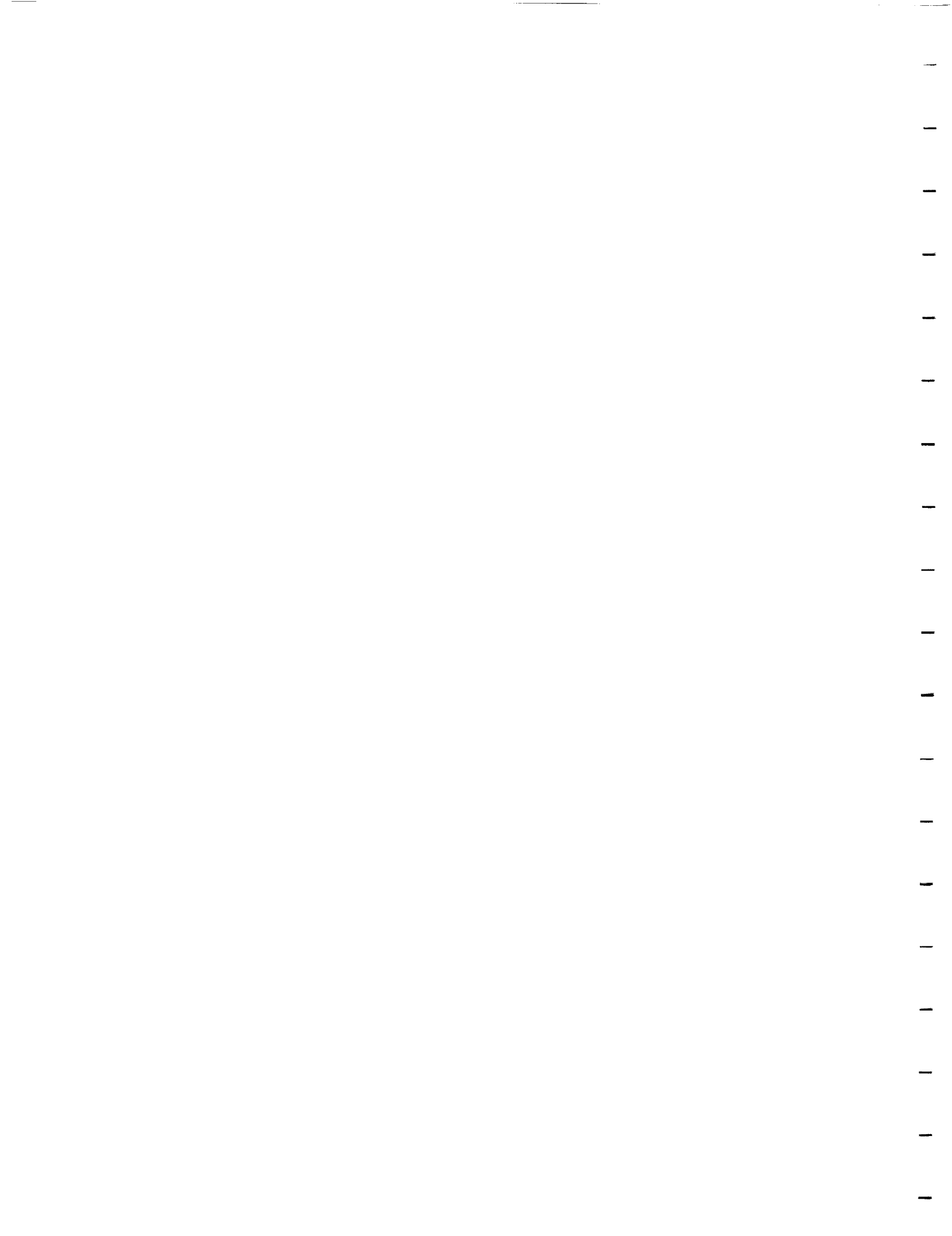
Absorption Coefficients

During this reporting period, there have only been a few minor changes in the precursor absorption coefficient model. Originally, predissociation from both the 1st and 2nd positive bands of N_2 was permitted since it was theoretically possible. However, subsequent review of the literature indicates that in the present temperature range of interest in the precursor that predissociation is involved in the the photodissociation of nitrogen only from the $\alpha\pi_g$ state following absorption (photoexcitation) in the Lyman-Birge Hopfield Band. Therefore, predissociation is no longer included through the N_2 1st and 2nd positive bands.

The second change is that the Vegard-Kaplan band is no longer included in the radiative calculations because, first, there is little evidence in the literature of its existence and, second, numerical studies conducted as part of this research have shown that it has negligible effect on precursor phenomena.

It is recognized that while these processes appear to be unimportant, they could have been retained in the model for completeness. However, their inclusion does require a measureable amount of computer time in any given case; and thus, in the interest of efficiency, they have been dropped.

Consequently, the following radiative processes are currently included in the precursor model:



Process	Frequency Range (ev)
N Low Frequency Ionization	$h\nu > 0$
N High Frequency Ionization	$h\nu > 10.8 \text{ ev}$
Free - Free	$h\nu > 0 \text{ ev}$
N2 Ionization	$h\nu > 8.24 \text{ ev}$
N2+(1-)	$2.23 < h\nu < 4.46 \text{ ev}$
N2(Birge-Hopfield)	$6.5 < h\nu < 12.77 \text{ ev}$
N2(1+)	$.75 < h\nu < 4.5 \text{ ev}$
N2(2+)	$.75 < h\nu < 4.5 \text{ ev}$
N2 (LBH)	$h\nu > 4.77 \text{ ev}$

Solution Scheme

Originally, the solution scheme for the precursor region solved the governing differential equations assuming a constant spatial step size. However, this approach in many cases either failed to provide sufficient detail in regions of high gradients or led to excessive memory and CPU requirements. Consequently, the solution scheme has been modified to allow a variable step size that is determined by changes in the flowfield properties. Typically, the step size is limited to a maximum value corresponding to a maximum of 15% percent change in any flowfield property; while the minimum value is selected to yield at least a 5% change. This approach significantly reduces solution times while placing large numbers of points in regions of high gradients.

Electron Thermal Nonequilibrium

The primary objective of the precursor research during this reporting period has been to develop and include in the nitrogen precursor model an appropriate model for electron thermal nonequilibrium. Such a model is important because the precursor radiative phenomena are strongly determined by the electron temperature.

While in the shock layer it is frequently possible to use a free electron temperature and assume that due to collisional phenomena that the electronic temperature is equivalent to the electron temperature, such an approach in the precursor is tenuous due to the overall low density and low number of free electrons. While theoretically a three temperature model, T , T_e , and T_{elec} , could be conceptualized, the electron electronic energy exchange expressions are not well known or understood. Consequently, it has been decided to utilize in the precursor model, two temperatures, T and $T_e = T_{elec}$, and a combined electron-electronic energy equation.

In the development of a combined electron-electronic energy equation, particularly considering that the dominant processes in the precursor are radiative, the manner in which each radiative process affects electron energy must be considered. Specifically, free-free processes affect the free electron translational energy, while in bound-free photoionization the energy involved is divided between that required for ionization and that associated with the translational energy of the created electron. Similarly, atomic line phenomena only affects the electronic energy, but the energy of molecular band absorption is distributed between electronic, vibrational, and rotational energy changes. Finally, bound-free photodissociation absorption involves the energy of dissociation plus the kinetic energy of the created atoms. Obviously, the inclusion of the appropriate



portions of each of these processes in the electron-electronic energy equation is somewhat subtle.

During this period, two approaches to the electron-electronic energy equation have been investigated, and in both cases thermal conduction, electron vibrational coupling, and diffusion effects have been neglected. The first approach is the "usual" technique of combining the free electron and electronic energy equations. By defining a new variable as

$$e_e''' = \frac{\rho_e}{\rho} e_e + \sum_i \frac{\rho_i}{\rho} e_{elec,i} \quad (P-4)$$

the combined equation can be written as

$$\frac{\partial}{\partial t} (\rho e_e''') + \frac{\partial}{\partial \vec{r}} \cdot (\rho e_e''' \vec{u}) = -\rho_e \frac{\partial}{\partial \vec{r}} \cdot \vec{u} + \sum_i \dot{\epsilon}_{ei} + Q_e + \dot{W}_e \frac{u^2}{2} - \frac{\partial}{\partial \vec{r}} \cdot \vec{g}_R^{FE} - \frac{\partial}{\partial \vec{r}} \cdot \vec{g}_R^{elec} \quad (P-5)$$

where $\dot{\epsilon}_{ei}$ and Q_e represent elastic and inelastic collisional effects and

$$\frac{\partial}{\partial \vec{r}} \cdot \vec{g}_R^{FE} = \underbrace{\frac{\partial}{\partial \vec{r}} \cdot \vec{g}_R^{FF}}_{\text{(Free-Free)}} + \underbrace{\frac{\partial}{\partial \vec{r}} \cdot \vec{g}_R^{BF,I}}_{\text{(Bound-Free Ionization)}} + \sum_i \dot{W}_i^{I,R} h_i^0 \quad \text{(photoionization)}$$

$$\frac{\partial}{\partial \vec{r}} \cdot \vec{g}_R^{elec} = \underbrace{\frac{\partial}{\partial \vec{r}} \cdot \vec{g}_R^{AL}}_{\text{(atomic lines)}} + \sum_{\text{molecular bands}} \int_0^\infty \frac{Y_i}{h\nu} (E_{2j} - E_{1j}) \frac{\partial}{\partial \vec{r}} \cdot \vec{g}_{R,i}^{TOT} d\nu \quad (P-5)$$

Here the last term in the first equation accounts for the radiative energy that goes into ionization in photoionization processes, while the second term in the last equation accounts for electronic energy changes due to molecular band transitions. In principle, the free-free, bound-free photoionization, and atomic line flux divergences could be

individually obtained from the radiation model, RADICAL. However, the last integral still requires the computation of total radiative flux.

The second approach is to directly utilize the total radiative flux computed by the modified version of RADICAL and eliminate from it those portions which do not directly affect electron or electronic energy. An appropriate energy equation for this case can be obtained by multiplying each species continuity equation by the species zero point energy, summing over all species and adding the resulting equation to the combined free electron electronic equation. Then by defining,

$$e_e'' = \frac{\rho_e}{\rho} e_e + \sum_i \frac{\rho_i}{\rho} (e_{elec,i} + h_i^0) \quad (P-6)$$

a combined electron-electronic energy equation is

$$\begin{aligned} \frac{\partial}{\partial t} (\rho e_e'') + \frac{\partial}{\partial \vec{r}} \cdot (\rho e_e'' \vec{u}) = & -\rho_e \frac{\partial}{\partial \vec{r}} \cdot \vec{u} + \sum \dot{S}_{ei} + Q_e + \dot{w}_e \frac{u^2}{2} \\ & + \sum \dot{w}_i h_i^0 - \frac{\partial}{\partial \vec{r}} \cdot \vec{g}_R^{Total} + \frac{\partial}{\partial \vec{r}} \cdot \vec{g}_R^{h_i^0} \\ & + \frac{\partial}{\partial \vec{r}} \cdot \vec{g}_R^{Tran} + \frac{\partial}{\partial \vec{r}} \cdot \vec{g}_R^{vib} + \frac{\partial}{\partial \vec{r}} \cdot \vec{g}_R^{Rot} \end{aligned} \quad (P-7)$$

Notice that the last four terms essentially correct the divergence of the radiative flux for those radiative portions which do not affect the electron or electronic energy. By properly examining each of the radiative flux terms, Equation (P-7) can be rewritten into the form

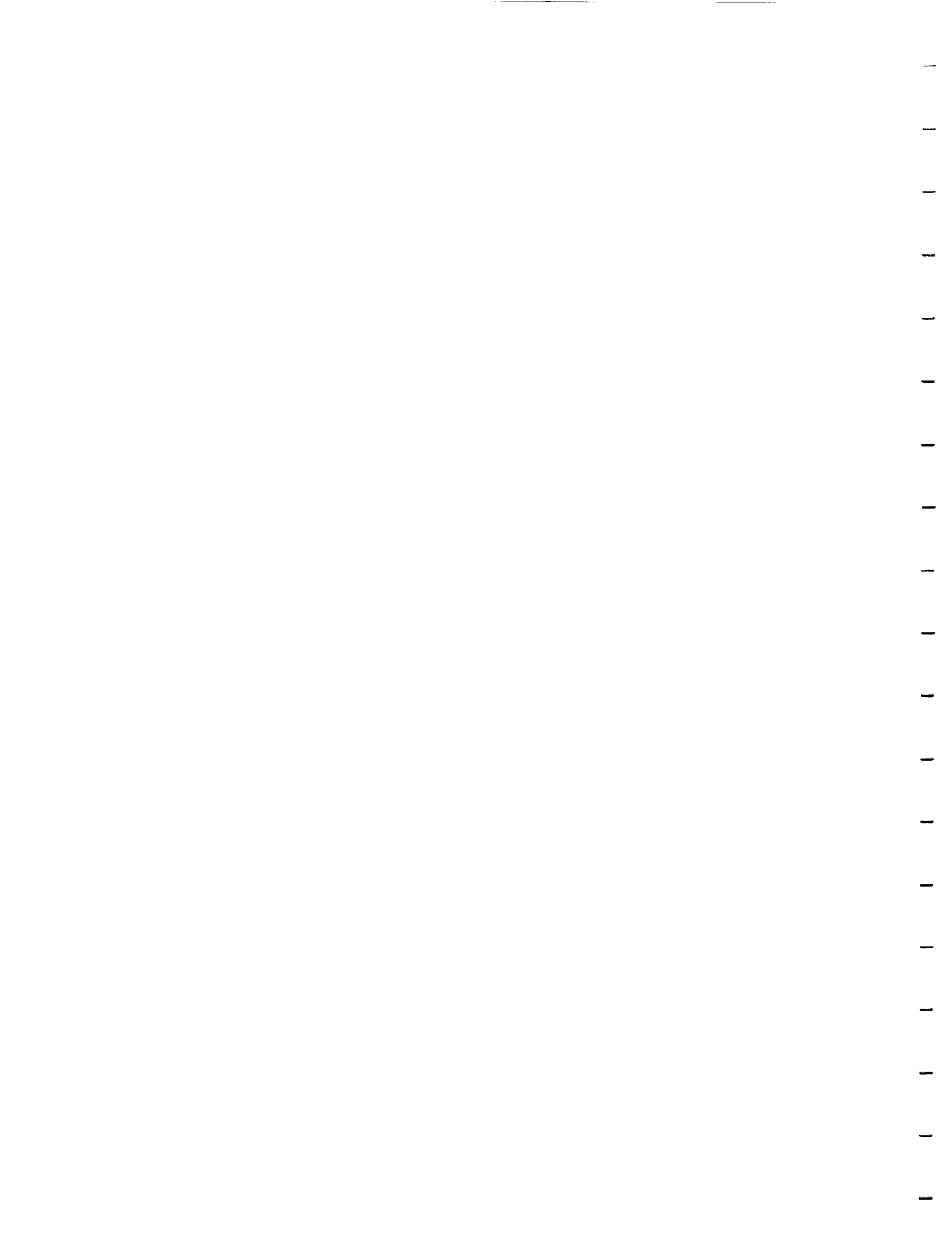
$$\frac{\partial}{\partial t} (\rho e_e'') + \frac{\partial}{\partial \vec{r}} \cdot (\rho e_e'' \vec{u}) = -\rho_e \frac{\partial}{\partial \vec{r}} \cdot \vec{u} + \sum \dot{S}_{ei} + Q_e + \dot{w}_e \frac{u^2}{2} + \sum \dot{w}_i^{collisions} h_i^0 - \frac{\partial}{\partial \vec{r}} \cdot \vec{g}_R^{Total} + A \quad (P-8)$$

where

$$A = \sum_{\text{molecular bands}} \left\{ \int_0^\infty Y_j \frac{(h\nu - E_{ij} - E_{lj})}{h\nu} \frac{\partial}{\partial \vec{r}} \cdot \vec{g}_{Rj}^{Total} d\nu ; h\nu < D_j \right. \\ \left. \int_0^\infty Y_j \frac{(h\nu - D_j)}{h\nu} \frac{\partial}{\partial \vec{r}} \cdot \vec{g}_{Rj}^{Total} d\nu ; h\nu \geq D_j \right.$$

Details of the derivation of these equations will be presented in a future report.

With respect to this electron-electronic energy equation and model the following points should be noted. First, the second approach decreases the number of required frequency integrations and modifications to RADICAL. Second, these equations are also applicable to the shock layer if it is desired to include in the shock layer the effects of photoprocesses



on electron electronic energy. Finally, it is believed that the above equation and model, when combined with our modified version of RADICAL, represents the most complete electron electronic energy and precursor model to date for a complicated diatomic gas such as nitrogen.

Test Case

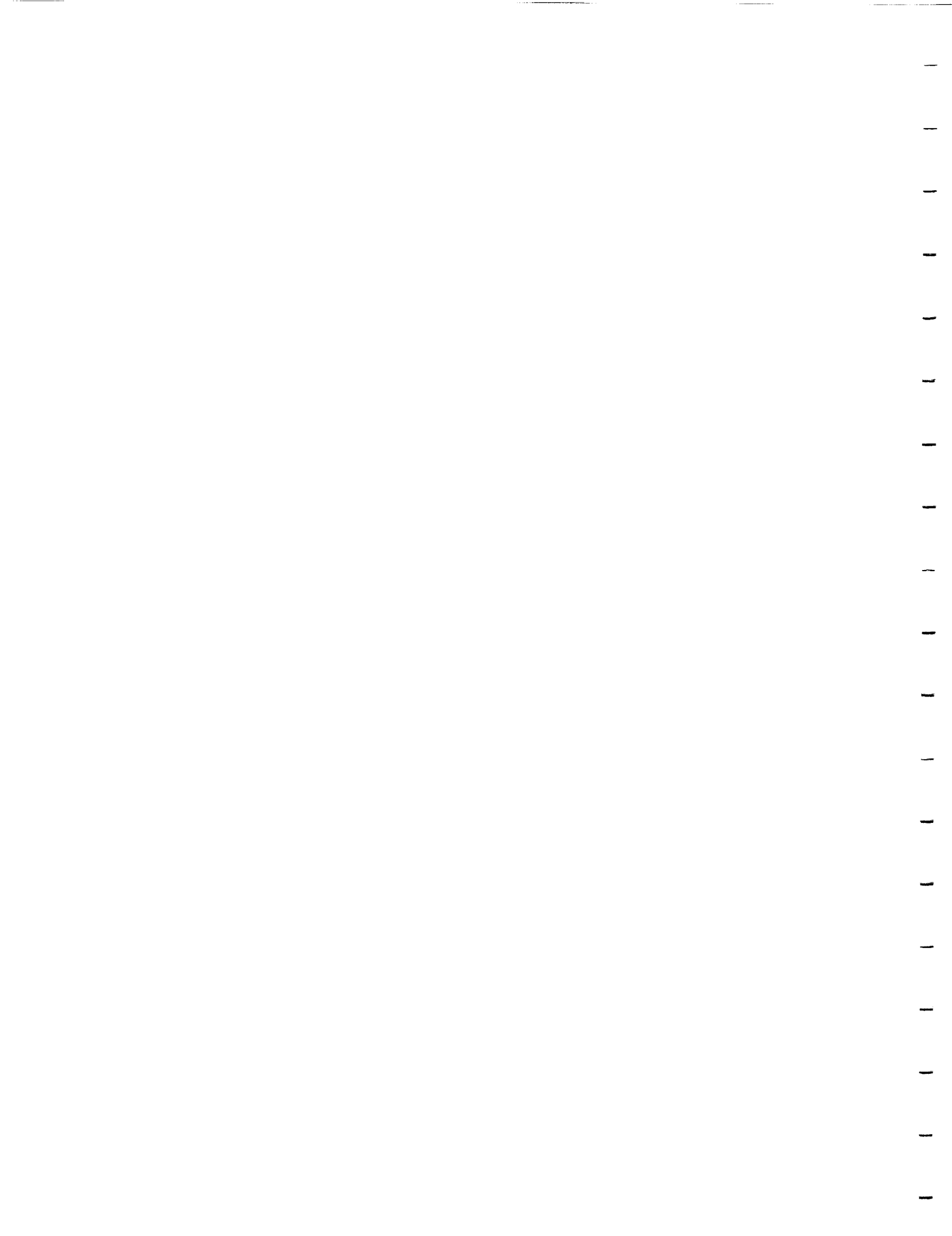
In order to develop the precursor model, it has been decided to use as a test condition the shock layer at 12 km/sec for a 230 cm nose radius body at 80 km altitude in nitrogen. In the last progress report, results were presented which neglected radiative cooling in the shock layer, assumed local thermodynamic equilibrium in the shock layer, and assumed thermal equilibrium in the precursor (i.e. $T_e = T$). During this reporting period, preliminary results have been obtained for this test condition. However, these new results include thermal nonequilibrium, radiative cooling, atomic line, atomic continuum, and molecular radiation in the shock layer. They also include local thermodynamic nonequilibrium phenomena for the atomic radiative processes in the shock layer. In the precursor, these results include radiation view factors, thermal nonequilibrium (T_e not equal to T), photodissociation and photoionization chemistry, and continuum emission and absorption processes. However, the precursor results do not yet include line effects or collisional chemistry.

Initially, the populations of excited states in the precursor were assumed to be determined by a Boltzman distribution at the electron temperature. While not strictly correct at the low densities being considered, it was believed that such an approach would be a reasonable approximation and not lead to any significant errors, particularly considering the low electron temperatures expected in the precursor zone. However, examination of the results indicated that the electron temperatures were sufficiently high to lead to emission in the region immediately in front of the shock, with a subsequent decrease in electron temperature.

Consequently, a collision limiting correction (Ref. 14) has been included in the program to more realistically predict the populations of the excited states of the molecules; and some preliminary results are shown on Figures 13 thru 18. Figure 13 shows the heavy particle temperature variation in the precursor zone; and in contrast to the results shown in the last progress report assuming thermal equilibrium, the present results indicate that heavy particle temperature is essentially constant in the precursor zone. This result is expected and is in agreement with multi-temperature calculations for argon (Ref. 11).

Likewise, the variations in pressure and density, portrayed on Figures 14 and 15, also are, for the test case, essentially constant in the precursor region. In this case, the slight increase in pressure ahead of the shock front is less than shown in the last progress report because the previous results did not include cooling or local thermodynamic nonequilibrium effects in the shock layer. Thus, the previous precursor results were for a case with a more strongly emitting shock layer, which induced more photoionization and dissociation. In the present case, the inclusion of cooling and radiative nonequilibrium effects in the shock layer results significantly reduces the radiation to the precursor zone.

The variation of the electron-electronic energy in the precursor is shown on Figure 16. As can be seen, as the flow approaches the shock front, it absorbs radiation from the bow shock layer; and the electron-electronic energy increases exponentially. Similarly, the



species concentrations, shown on Figure 17, also vary exponentially with distance from the shock front. Notice that while low, there is measurable dissociation at distances greater than 150 shock layer thicknesses, indicating that photodissociation of N_2 occurs primarily in the far precursor. In addition, there is significant ionization, on the order of $1E-04$ and primarily N_2^+ , in the near precursor immediately in front of the shock wave. Although the effect of these pre-shock ions and electrons on the post-shock flowfield has yet to be determined, it should be noted that the present results are for a relatively cool shock layer (10,000 K) and yet they indicate that immediately behind the shock front, an electron density on the order of $4E11$ particles/cubic cm could be expected. Such a level might affect both chemical and radiative nonequilibrium phenomena in the nonequilibrium zone behind the shock front.

Finally, the electron temperature variation in the precursor is shown on Figure 18. In examining this result, it should be remembered that electron temperature is a measure of the average Kinetic energy associated with each electron at a given location. Thus, the high temperature predicted for the far precursor indicates that electrons created via photoionization far away from the vehicle were created by high energy radiation. However, as shown on Figure 19, the number of electrons in the far precursor is extremely small. Then, as the flow approaches the vehicle the electron temperature slowly increases to a value above 4000 K until about 50 shock thickness, where it begins to decrease slightly.

Originally, it was suspected that this electron temperature decrease was due to emission from the near precursor created by the assumption that the electronic states of N_2^+ etc. were populated according to a Boltzmann distribution. This assumption predicts higher populations for the excited states than can be realistically maintained by collisional excitation at the freestream densities and leads to enhanced emission. This supposition has been partially verified by the introduction of the collision limiting model, which predicts electron temperatures (shown on Fig. 18) near the shock front about 500 K higher than those obtained without it. Interestingly, electron temperature is the only quantity measureably affected by the introduction of the collision limiting model.

Currently, it is believed that the electron temperature decrease shown on Figure 18 is due to the exponential growth of the number of electrons in the near precursor region combined with the fact that these electrons are created by photoionization involving radiation near and slightly above the ionization threshold. Consequently, the created electrons have "low" Kinetic energy compared to those formed in the far precursor; and the average free electron Kinetic energy or electron temperature decreases. However, when atomic line radiation is included in the precursor model, it is anticipated that the electron temperature will increase somewhat in the near precursor due to the absorption of energy into the electron bands. On the other hand, the inclusion of collision chemistry in the near precursor would lead to some ionization by electron impact, which in turn would cause a decrease in electron temperature. Thus, the present profiles may be reasonably realistic for a nitrogen freestream. In any event, these results do indicate that enhanced electron temperatures on the order of 4000 K and measurable ionization levels due to N_2^+ do exist in the region immediately in front of the shock layer.

Future Plans

During the next reporting period it is planned to obtain further precursor solutions, probably for the velocity range of 12 to 16 km/sec and for altitudes of 70 to 80 km. It is anticipated that precursor phenomena will be significantly increased as altitudes are



decreased and velocities are increased. Based upon these results, a series of parametric studies will be conducted on the stagnation region shock layer using the nonequilibrium radiation coupled multi-temperature VSL code in order to determine the effect of these precursors on the shock layer chemistry, flowfield profiles, and, in particular, the radiative heat transfer to the body. In addition, since the present precursor electron-electronic energy model has been formulated to include line radiation, consideration will be given to including atomic lines and determining their effect on the precursor. However, it is not anticipated that collisional chemistry will be included in the precursor model during the next reporting period.

VII. Publications

While no new publications associated with the project were issued during this reporting period, AIAA Paper 89-1729, "The Effect of Electron Temperature and Impact Ionization on Martian Return AOTV Flowfields," by L. A. Carlson and T. A. Gally, has been accepted for publication in the Journal of Thermophysics and Heat Transfer. It is anticipated that this article will appear during the latter part of 1990.

In addition, an abstract of a proposed paper entitled "Nonequilibrium Chemical and Radiation Coupling Phenomena in AOTV Flowfields" has been submitted and accepted for presentation at the 29th Aerospace Sciences Meeting to be held in Reno, Nevada in January 1991. A copy of this abstract is included in this report as Appendix I for your information and approval.

During the next reporting period, it is anticipated that one or more abstracts will be submitted for possible paper presentations at the AIAA Fluid and Plasmadynamics and Thermophysics Conferences to be held in June 1991 in Honolulu, Hawaii.

Table I -- Stagnation Point Radiative Heat Transfer for Test Case I
(U = 12 km/sec, Altitude = 80 km, Nose Radius = 2.3 m)

Atomic Radiation and Atomic LTNE Corrections Only	--	14.0 watts/sq cm.
Atomic and Molecular Radiation with Atomic LTNE Corrections Only	--	18.1 watts/sq cm.
Atomic and Molecular Radiation with Both Atomic and Molecular LTNE Corrections	--	16.5 watts/sq cm



Table II -- Stagnation Point Radiative Heat Transfer for Test Case III
 $U = 16 \text{ km/sec}$, $\text{Altitude} = 80 \text{ km}$, $\text{Nose Radius} = 2.3 \text{ m}$

Atomic Radiation and Atomic LTNE Corrections Only -- 331 watts/sq cm.
 No Radiation Gasdynamic Coupling

Atomic and Molecular Radiation
 with LTNE Corrections on Both -- 340 watts/sq cm.
 No Radiation Gasdynamic Coupling

Atomic and Molecular Radiation with
 Both Atomic and Molecular LTNE Corrections -- 189 watts/sq cm
 Radiation Gasdynamic Coupling Included

Table III-- Stagnation Point Radiative Heat Transfer for AFE CFD Point 2
 $U = 8.915 \text{ km/sec}$, $\text{Altitude} = 77.9 \text{ km}$, $\text{Nose Radius} = 2.3 \text{ m}$

Atomic and Molecular Radiation
 with Atomic LTNE Corrections Only -- 7.0 watts/sq cm.
 No Radiation Gasdynamic Coupling

Atomic and Molecular Radiation
 with LTNE Corrections on Both -- 1.7 watts/sq cm.
 No Radiation Gasdynamic Coupling

Atomic and Molecular Radiation
 with Atomic LTNE Corrections Only -- 5.7 watts/sq cm.
 Radiation Gasdynamic Coupling Included

Atomic and Molecular Radiation with
 Both Atomic and Molecular LTNE Corrections -- 1.7 watts/sq cm
 Radiation Gasdynamic Coupling Included



Table IV -- Stagnation Point Radiative Heat Transfer for AFE CFD Point 4
(U = 9.326 km/sec, Altitude = 75.15 km, Nose Radius = 2.3 m)

Atomic and Molecular Radiation with Atomic LTNE Corrections Only No Radiation Gasdynamic Coupling	-- 8.8 watts/sq cm.
Atomic and Molecular Radiation with LTNE Corrections on Both No Radiation Gasdynamic Coupling	-- 3.2 watts/sq cm.
Atomic and Molecular Radiation with Atomic LTNE Corrections Only Radiation Gasdynamic Coupling Included	-- 7.5 watts/sq cm.
Atomic and Molecular Radiation with Both Atomic and Molecular LTNE Corrections Radiation Gasdynamic Coupling Included	-- 3.2 watts/sq cm

Table V -- Collisional Reaction Rate System

Number	Reaction
1.	$N_2 + M \rightleftharpoons 2 N_g + M \quad (M = N_g, N^*)$
2.	$N_2 + N_2 \rightleftharpoons 2 N_g + N_2$
3.	$N_2 + M \rightleftharpoons 2 N + M \quad (M = N^+, N_2^+, e^-)$
4.	$N_2 + N^+ \rightleftharpoons N_2^+ + N_g$
5.	$N_g + N_g \rightleftharpoons N_2^+ + e^-$
6.	$N_g + N \rightleftharpoons N^+ + e^- + N$
7.	$N_g + N^+ \rightleftharpoons 2 N^+ + e^-$
8.	$N_g + e^- \rightleftharpoons N^+ + 2 e^-$
9.	$N_g + e^- \rightleftharpoons N^* + e^-$
10.	$N^* + e^- \rightleftharpoons N^+ + 2 e^-$



VIII. Technical Monitor

The NASA technical monitor for this grant is Lin C. Hartung, Aerothermodynamics Branch, Space Systems Division, NASA Langley Research Center, Hampton, Virginia.

IX. References

1. Gnoffo, P. A., Gupta, R. N., and Shinn, J. L., "Conservation Equations and Physical Models for Hypersonic Air Flows in Thermal and Chemical Nonequilibrium," NASA TP 2867, February 1987.
2. Lee, J. H., "Basic Governing Equations for the Flight Regimes of Aeroassisted Orbital Transfer Vehicles," in Thermal Design of Aeroassisted Orbital Transfer Vehicles, Progress in Astronautics and Aeronautics, Vol. 96, Ed. by H. F. Nelson, AIAA, New York, 1985, pp. 3 - 53.
3. Carlson, L. A. and Gally, T. A., "The Effect of Electron Temperature and Impact Ionization on Martian Return AOTV Flowfields," AIAA Paper 89-1729, June 1989.
4. Carlson, L. A., "Radiative Gasdynamic Coupling and Nonequilibrium Effects Behind Reflected Shock Waves," AIAA Journal, vol. 9, No. 5, May 1971, pp. 858-865.
5. Chapman, S. and Cowling, T. G., The Mathematical Theory of Non-Uniform Gases, Cambridge, 1964.
6. Carlson, L. A., Bobskill, G. J., and Greendyke, R. B., "Comparison of Vibration Dissociation Coupling and Radiative Transfer Models for AOTV/AFE Flowfields," Journal of Thermophysics and Heat Transfer, Vol. 4, No. 1, January 1990, pp. 16-26.
7. Park, C., "Calculation of Nonequilibrium Radiation in the Flight Regimes of Aeroassisted Orbital Transfer Vehicles," in Thermal Design of Aeroassisted Orbital Transfer Vehicles, Progress in Astronautics and Aeronautics, Vol. 96, Ed. by H. F. Nelson, AIAA, New York, 1985, pp. 395 - 418.
8. Carlson, L. A., "Approximations for Hypervelocity Nonequilibrium Radiating, Reacting, and Conducting Stagnation Regions," Journal of Thermophysics and Heat Transfer, Vol. 3, No. 4, October 1989, pp. 380-388.
9. Park, C., "Assesment of Two Temperature Kinetic Model for Ionizing Air," AIAA Paper 87-1574, June 1987.
10. Kunc, J. A. and Soon, W. H., "Collisional Radiative Nonequilibrium in Partially Ionized Atomic Nitrogen," Physical Review A, Vol. 40, No. 10, November 15, 1989, pp. 5822 ff.
11. Foley, W. H. and Clarke, J. H., "Shock Waves Structered by Nonequilibrium Ionizing and Thermal Phenomena," Physics of Fluids, Vol. 16, No. 3, March 1973, pp. 1612-1620.
12. Nelson, H. F., "Nonequilibrium Structure of Argon Shock Waves," Physics of Fluids, Vol. 16, No. 12, December 1973, pp. 2132 - 2142.



13. Park, C., "Nonequilibrium Air Radiation (NEQQAIR) Program: User's Manual," NASA TM B6707, July 1985.

14. Horton, T. E., "Radiative Coupled Nonequilibrium Flow Fields Associated with Aeroassisted Orbital Transfer," Final Contractors Report for NASA Grant NAG-1-496, March 1986.



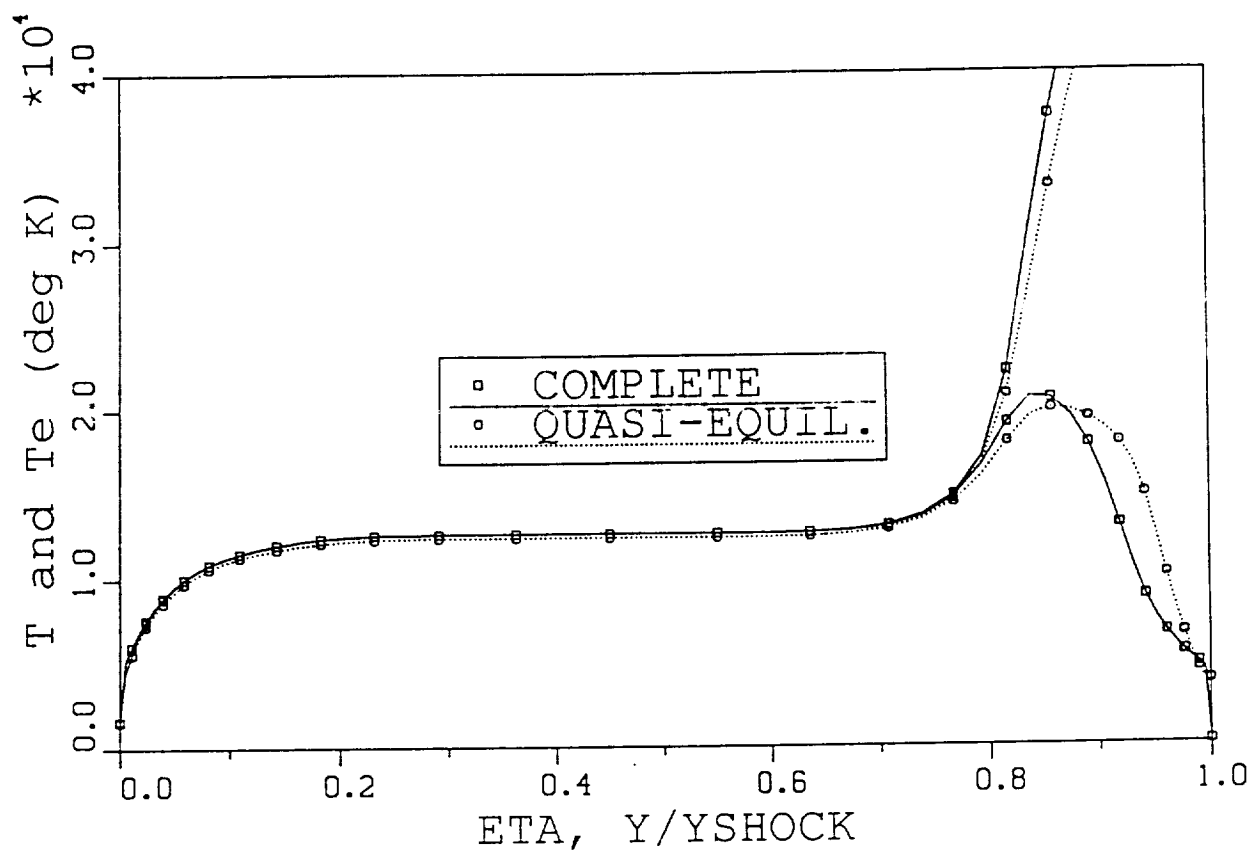


Fig. 1 -- Stagnation Line Heavy Particle and Electron Temperature Profiles Using the Complete Electron-Electronic Energy Equation and the Quasi-Equilibrium Electron Energy Equation

$U = 16 \text{ km/sec}$, $H = 80 \text{ km}$, $R_{\text{nose}} = 2.3 \text{ m}$



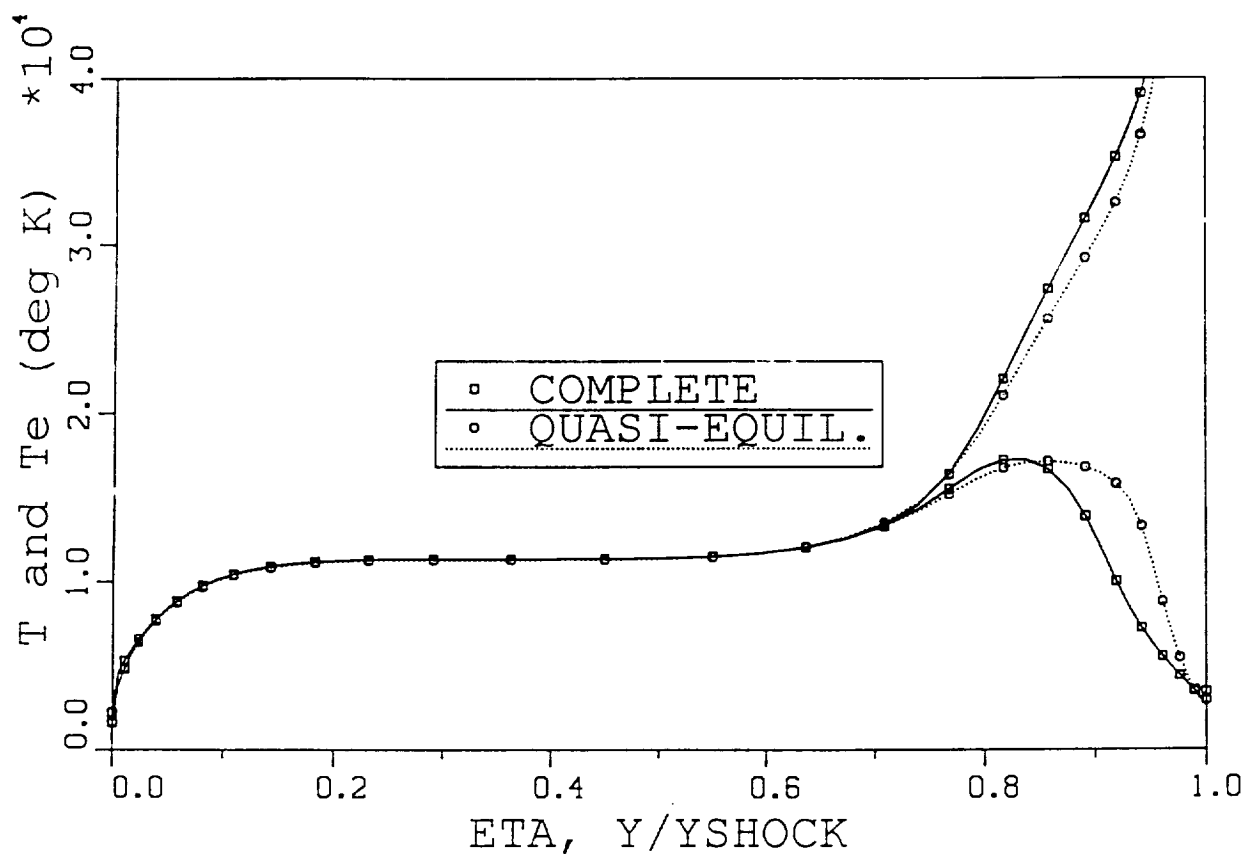


Fig. 2 -- Stagnation Line Heavy Particle and Electron Temperature Profiles Using the Complete Electron-Electronic Energy Equation and the Quasi-Equilibrium Electron Energy Equation

$U = 14 \text{ km/sec}$, $H = 80 \text{ km}$, $R_{\text{nose}} = 2.3 \text{ m}$



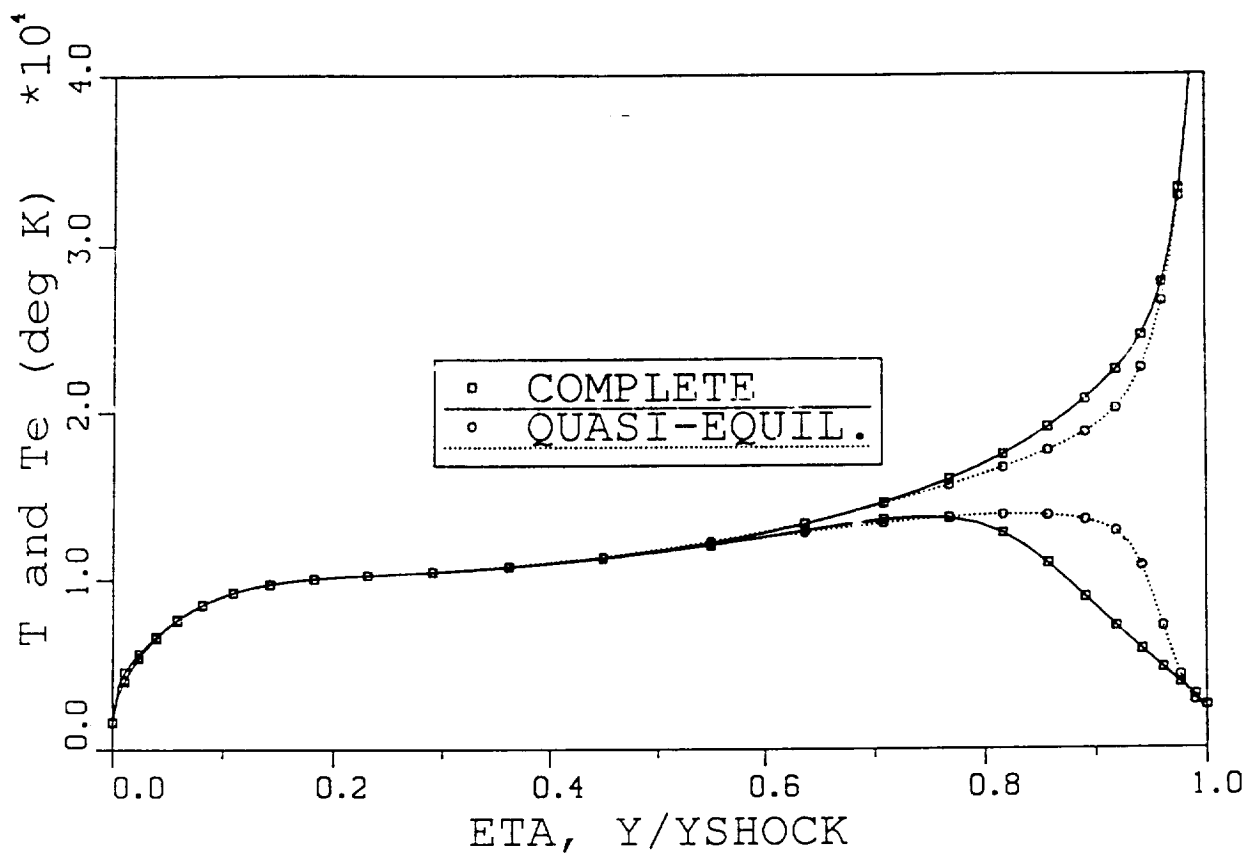
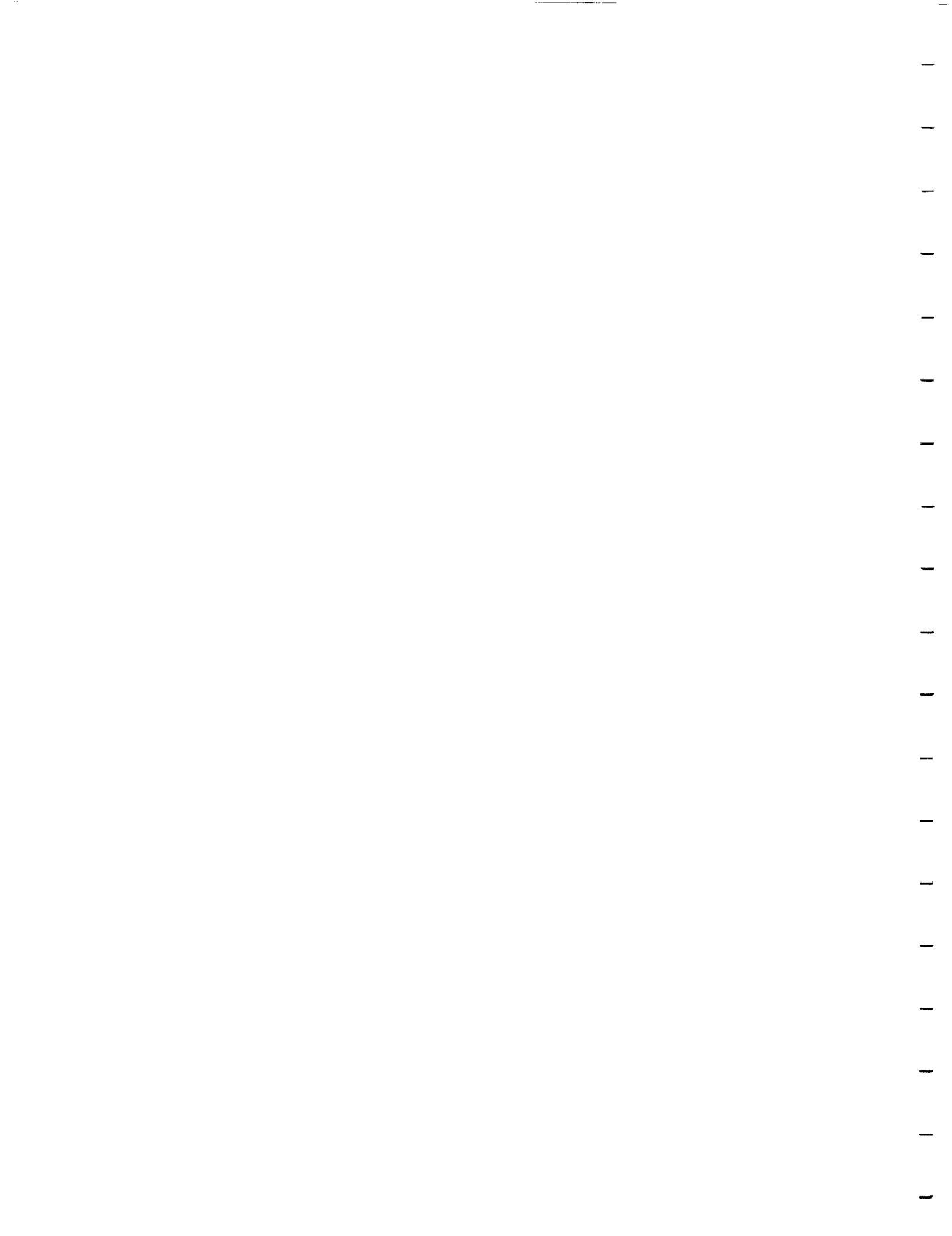


Fig. 3 -- Stagnation Line Heavy Particle and Electron Temperature Profiles Using the Complete Electron-Electronic Energy Equation and the Quasi-Equilibrium Electron Energy Equation

$U = 12 \text{ km/sec}$, $H = 80 \text{ km}$, $R_{\text{nose}} = 2.3 \text{ m}$



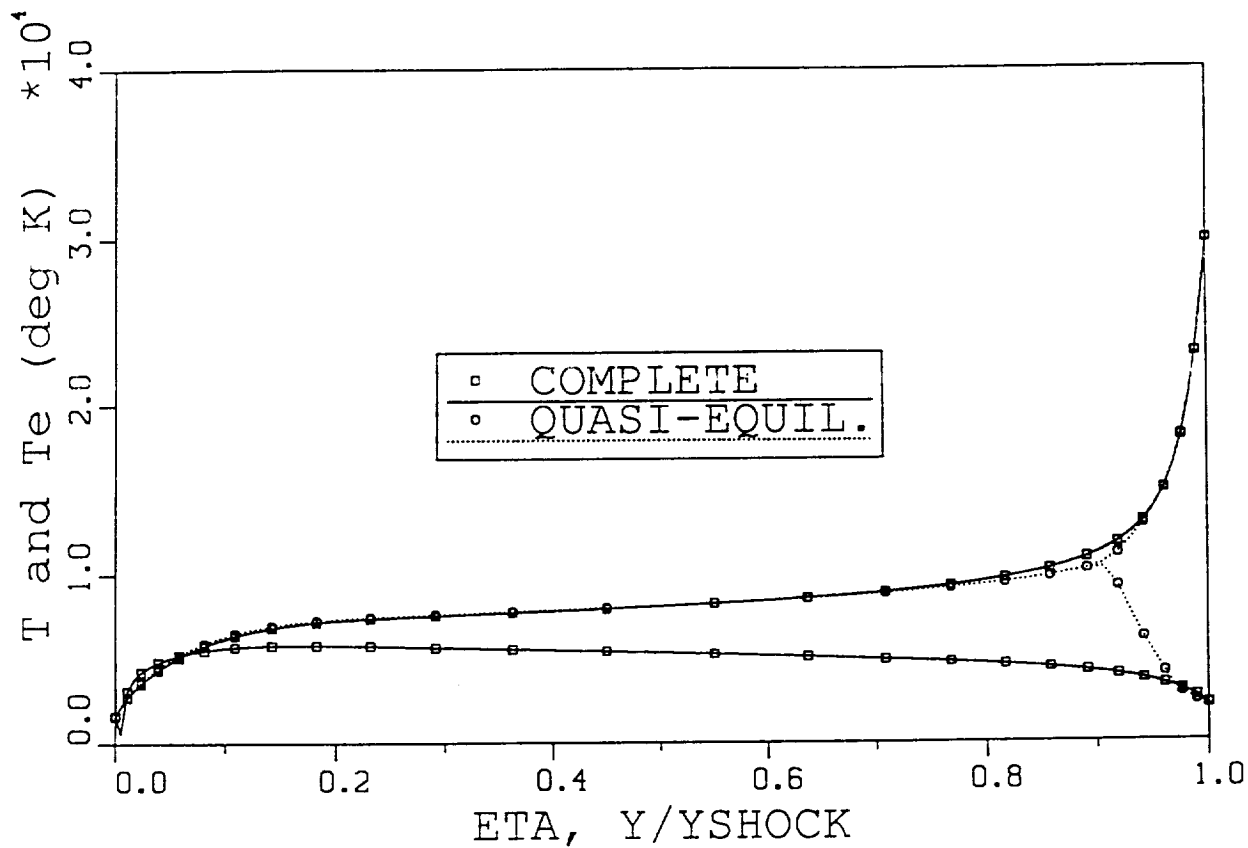


Fig. 4 -- Stagnation Line Heavy Particle and Electron Temperature Profiles Using the Complete Electron-Electronic Energy Equation and the Quasi-Equilibrium Electron Energy Equation

$U = 8.915 \text{ km/sec}$, $H = 77.9 \text{ km}$, $R_{\text{nose}} = 2.3 \text{ m}$



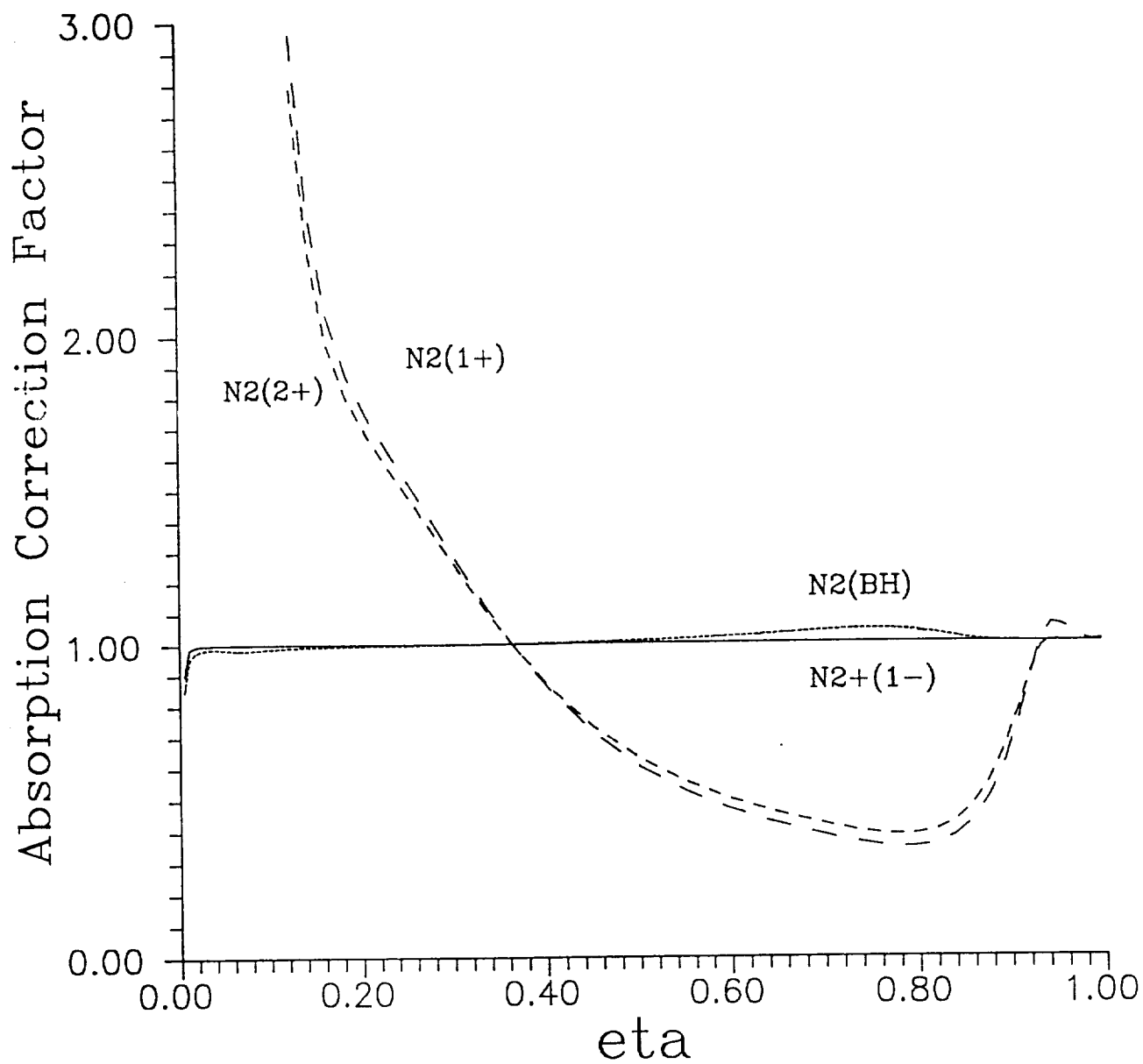


Fig. 5 -- Absorption Coefficient LTNE Factors for Molecular Radiation Along Stagnation Line
 $U = 12 \text{ km/sec}$, $H = 80 \text{ km}$, $R_{\text{nose}} = 2.3 \text{ m}$

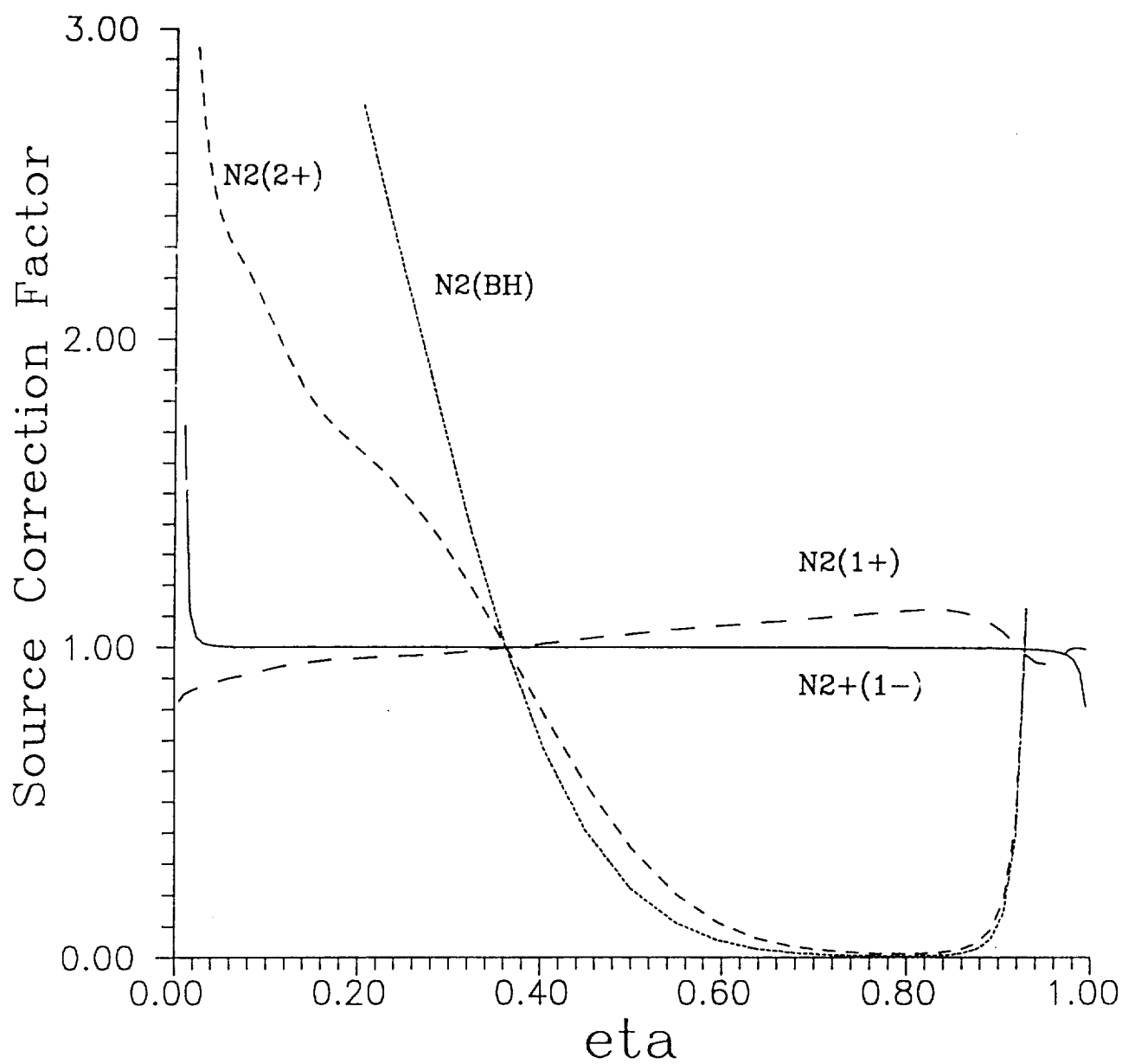


Fig. 6 -- Source Function LTNE Factors for Molecular Radiation Along Stagnation Line
 $U = 12 \text{ km/sec}$, $H = 80 \text{ km}$, $R_{\text{nose}} = 2.3 \text{ m}$

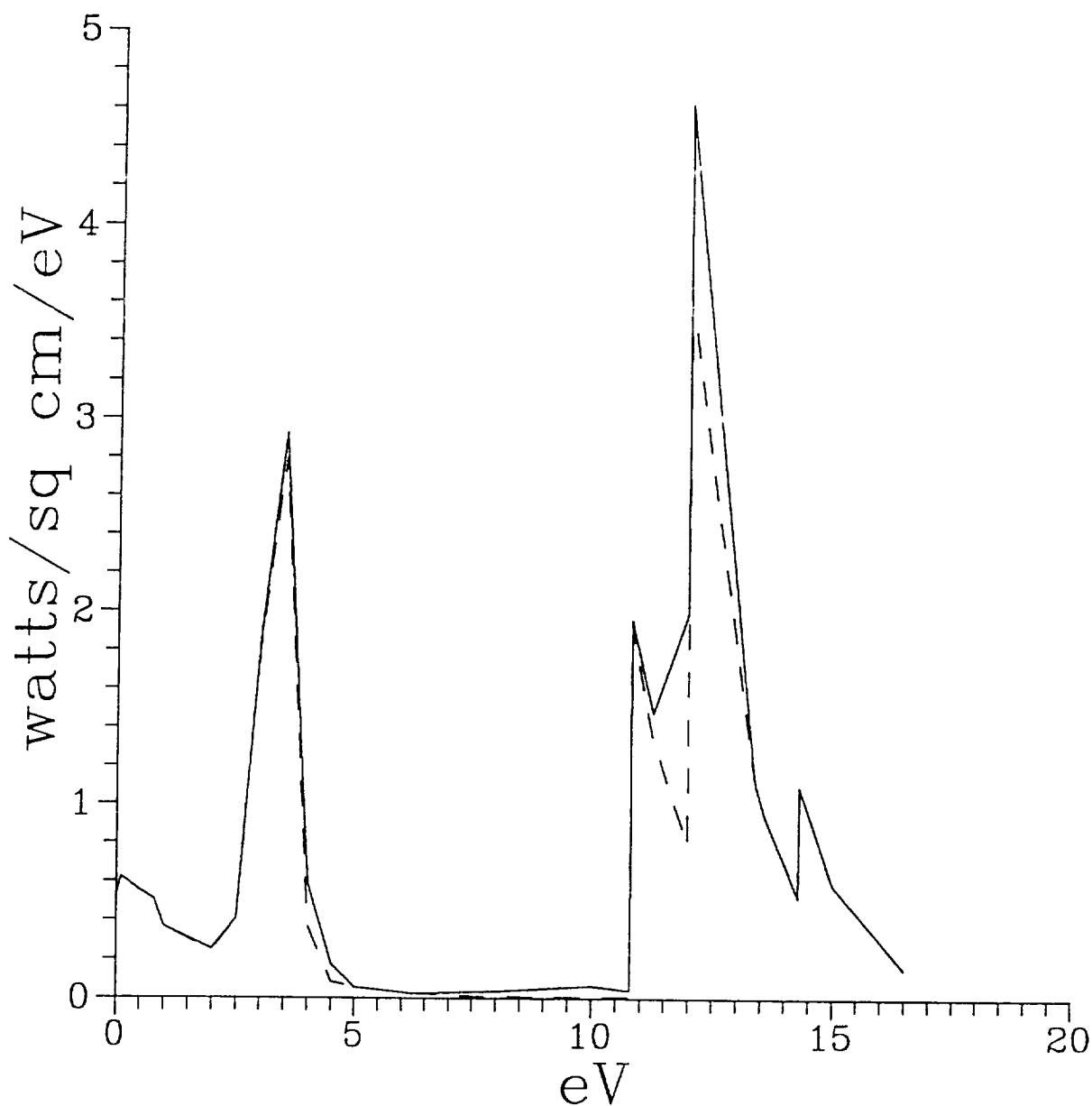


Fig. 7 -- Atomic and Molecular Continuum Stagnation Point Radiation With and Without
Molecular LTNE Factors
 $U = 12$ km/sec, $H = 80$ km, $R_{nose} = 2.3$ m



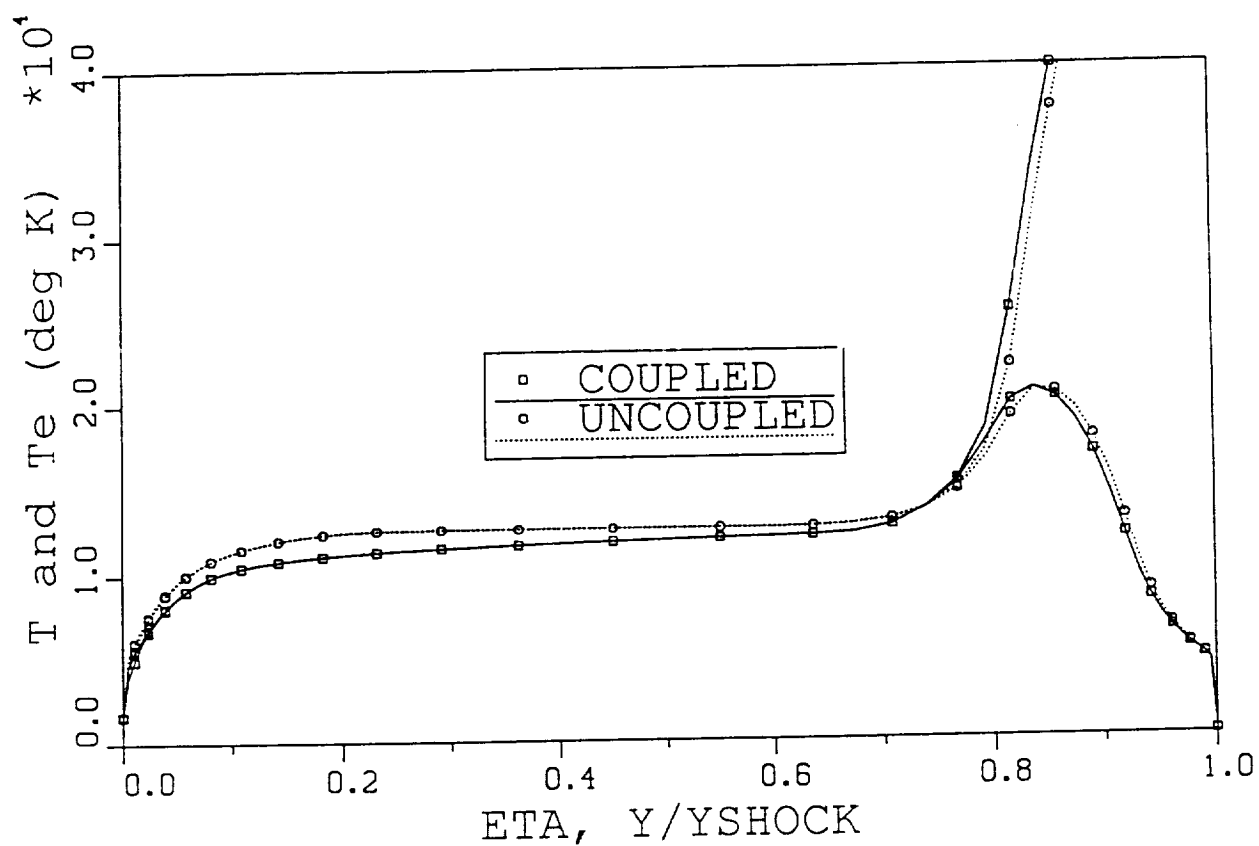


Fig. 8 -- Stagnation Line Heavy Particle and Electron-Electronic Temperatures
With and Without Radiation Gasdynamic Coupling
 $U = 16 \text{ km/sec}$, $H = 80 \text{ km}$, $R_{\text{nose}} = 2.3 \text{ m}$



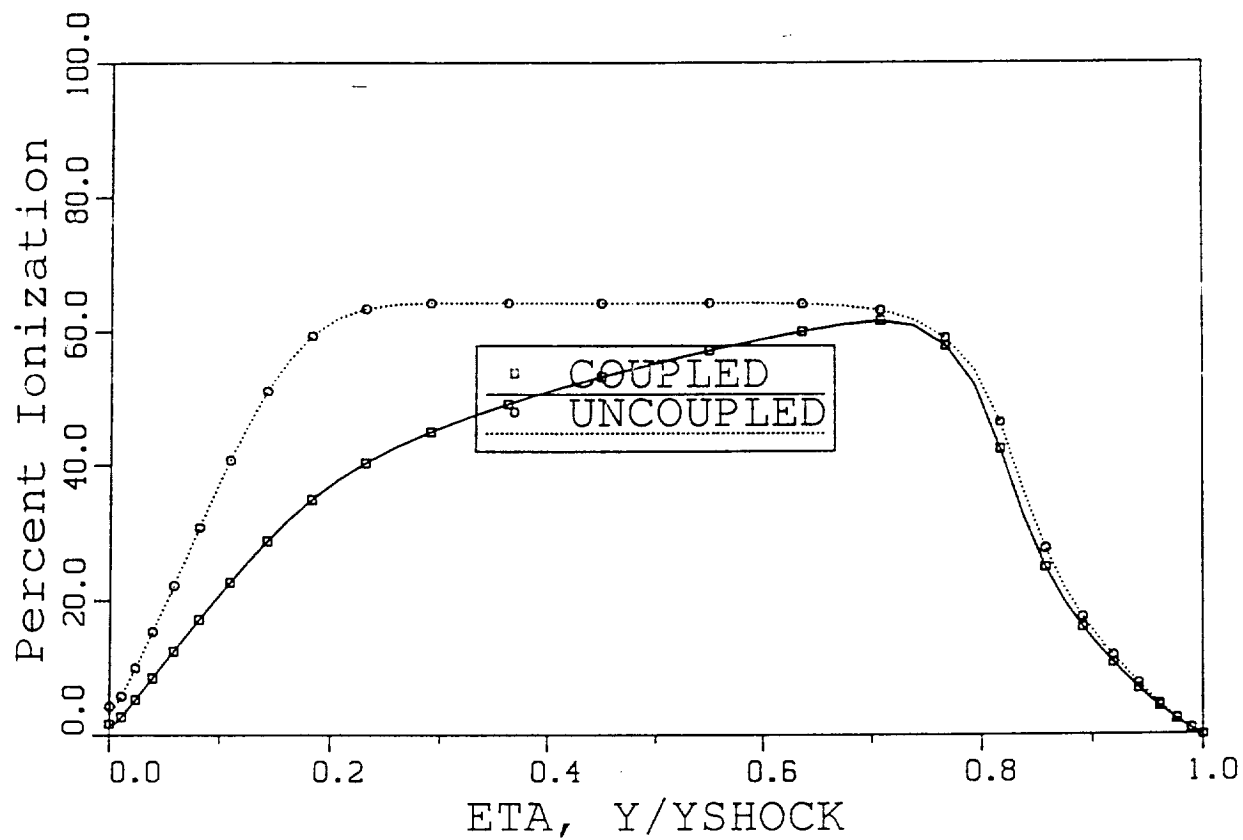
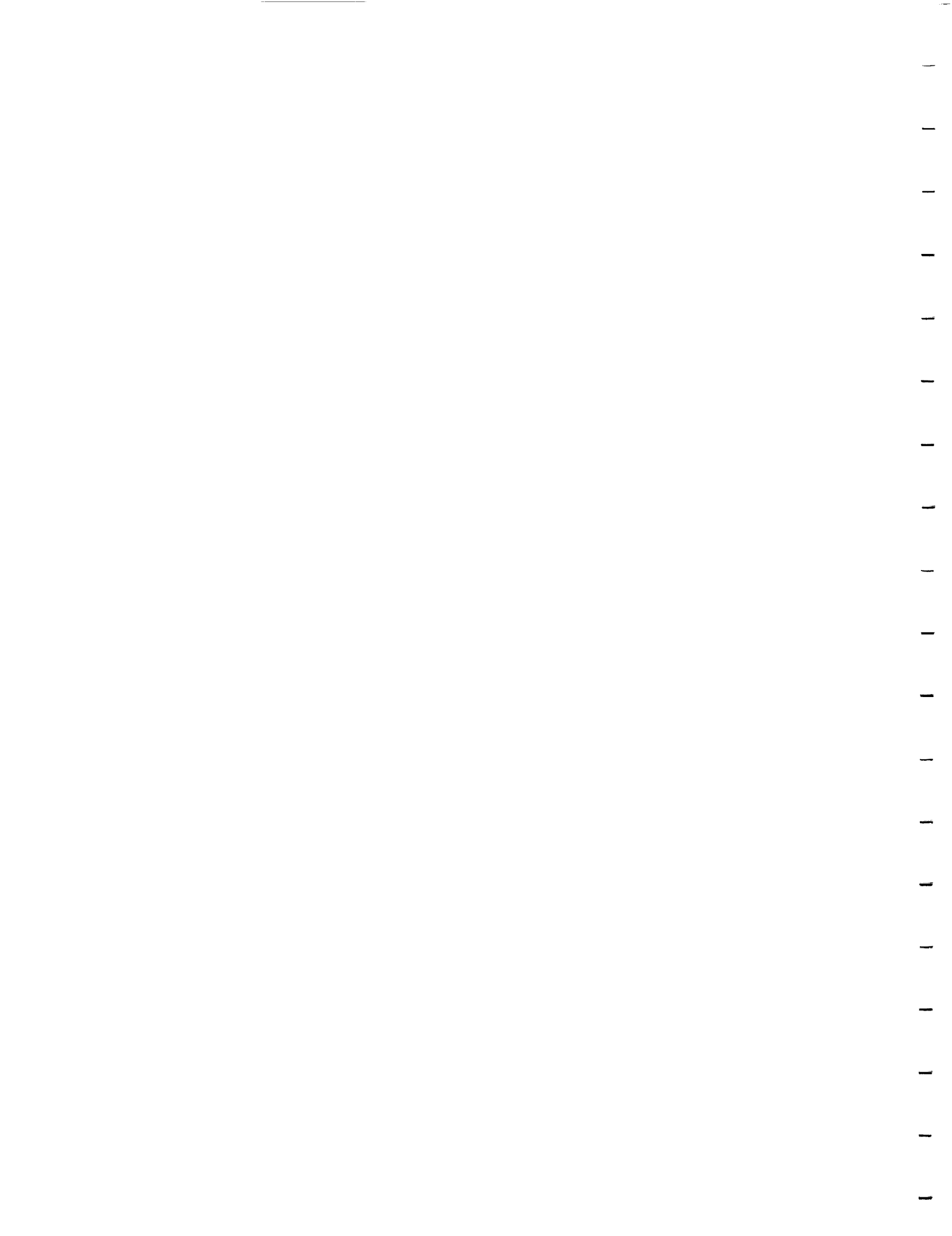


Fig. 9 -- Stagnation Line Degree of Ionization With and Without Radiation Gasdynamic Coupling

$U = 16 \text{ km/sec}$, $H = 80 \text{ km}$, $R_{nose} = 2.3 \text{ m}$



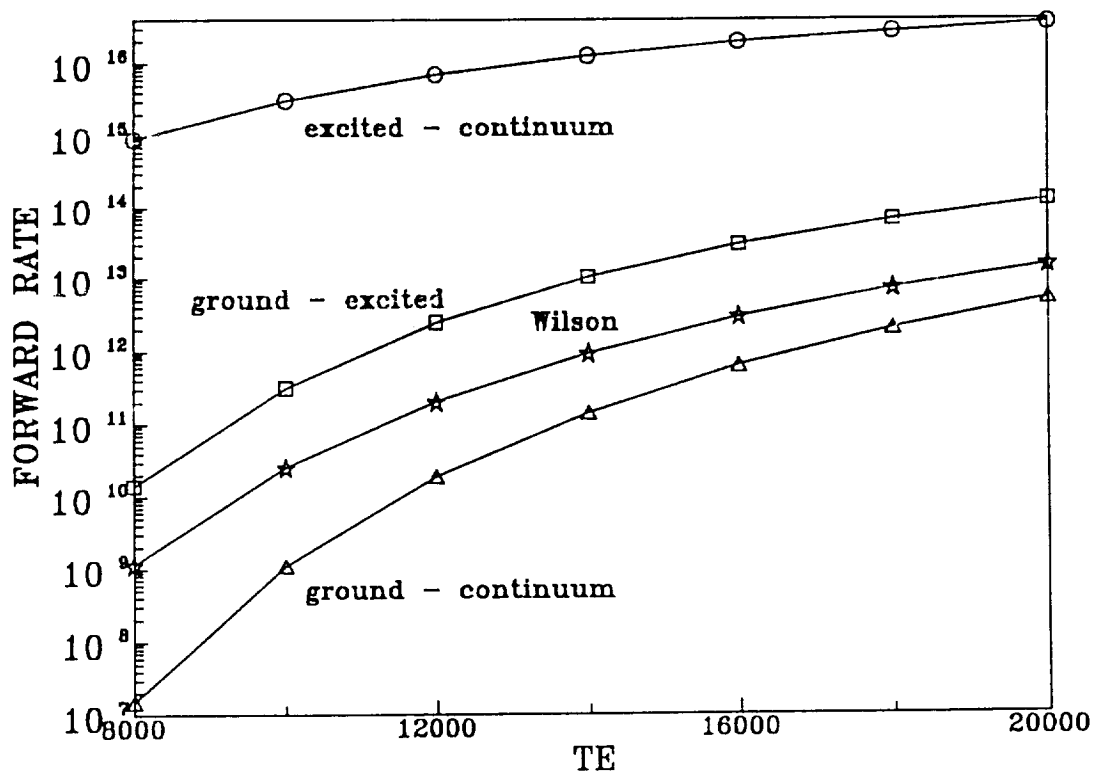


Fig. 10 -- Effective Forward Reaction Rates for Excitation and Ionization From N(ground) and N(excited)



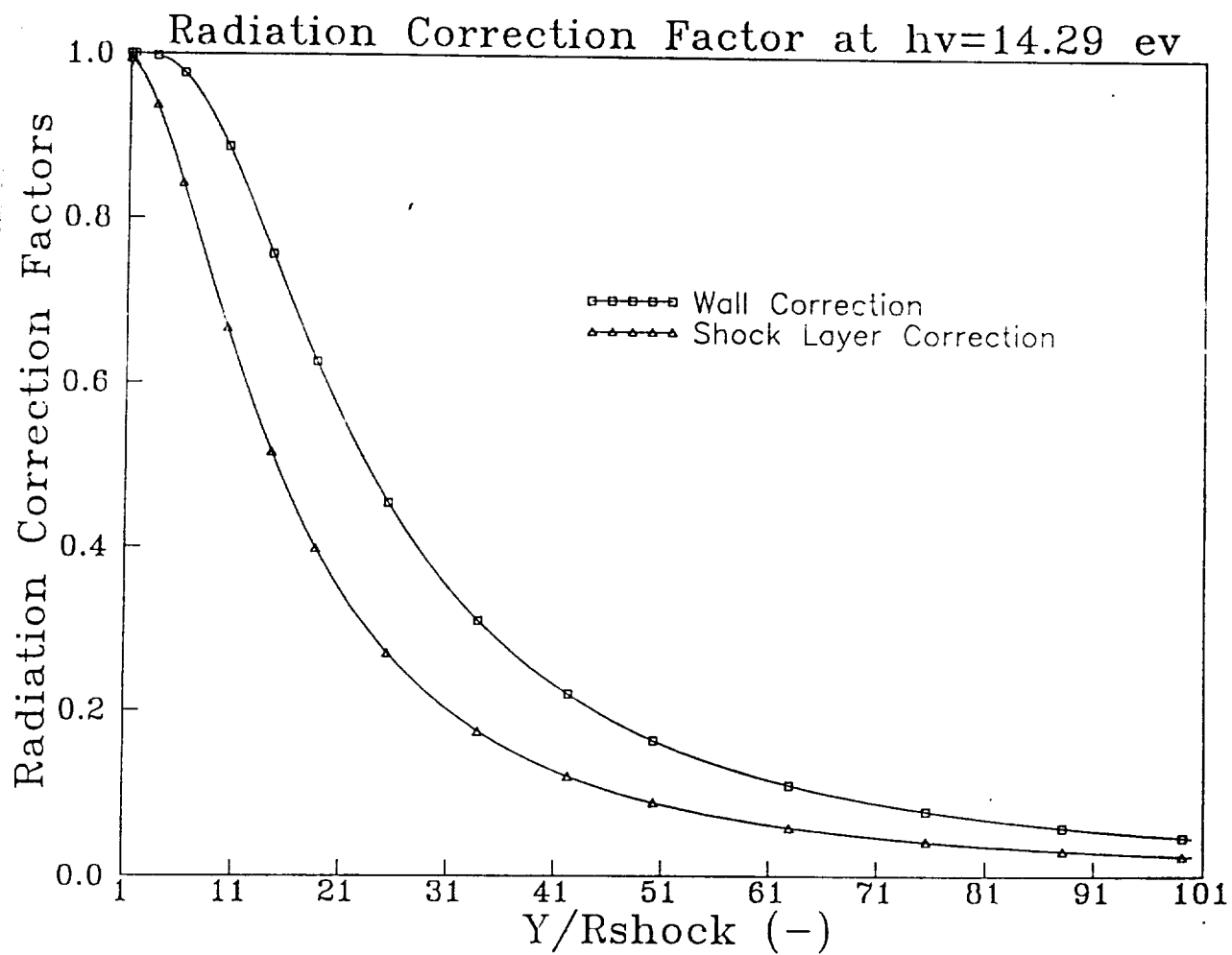


Fig. 11 -- Radiation View Factors at 14.29 eV
 $R_{\text{nose}} = 2.3$ m



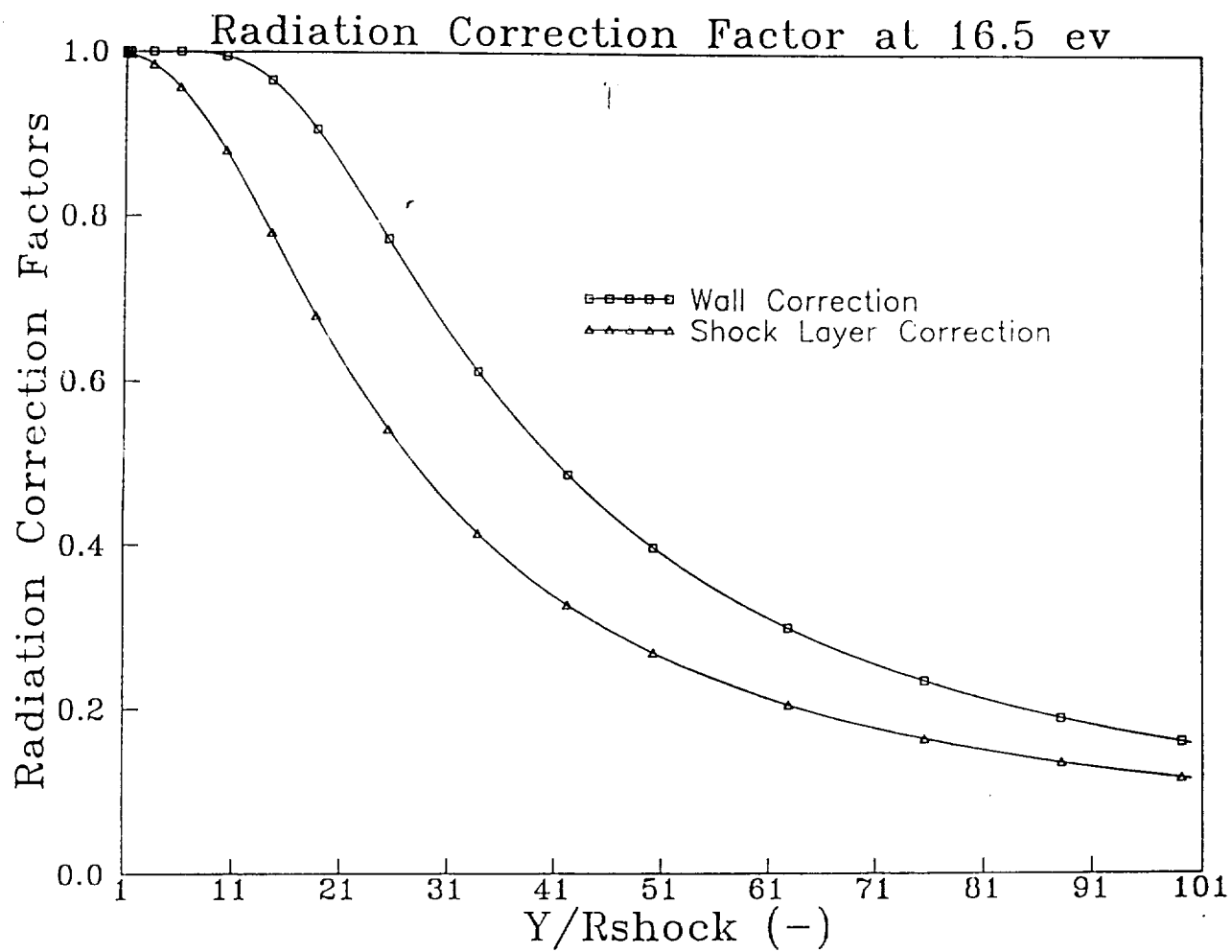


Fig. 12 -- Radiation View Factors at 16.5 ev
Rnose = 2.3 m



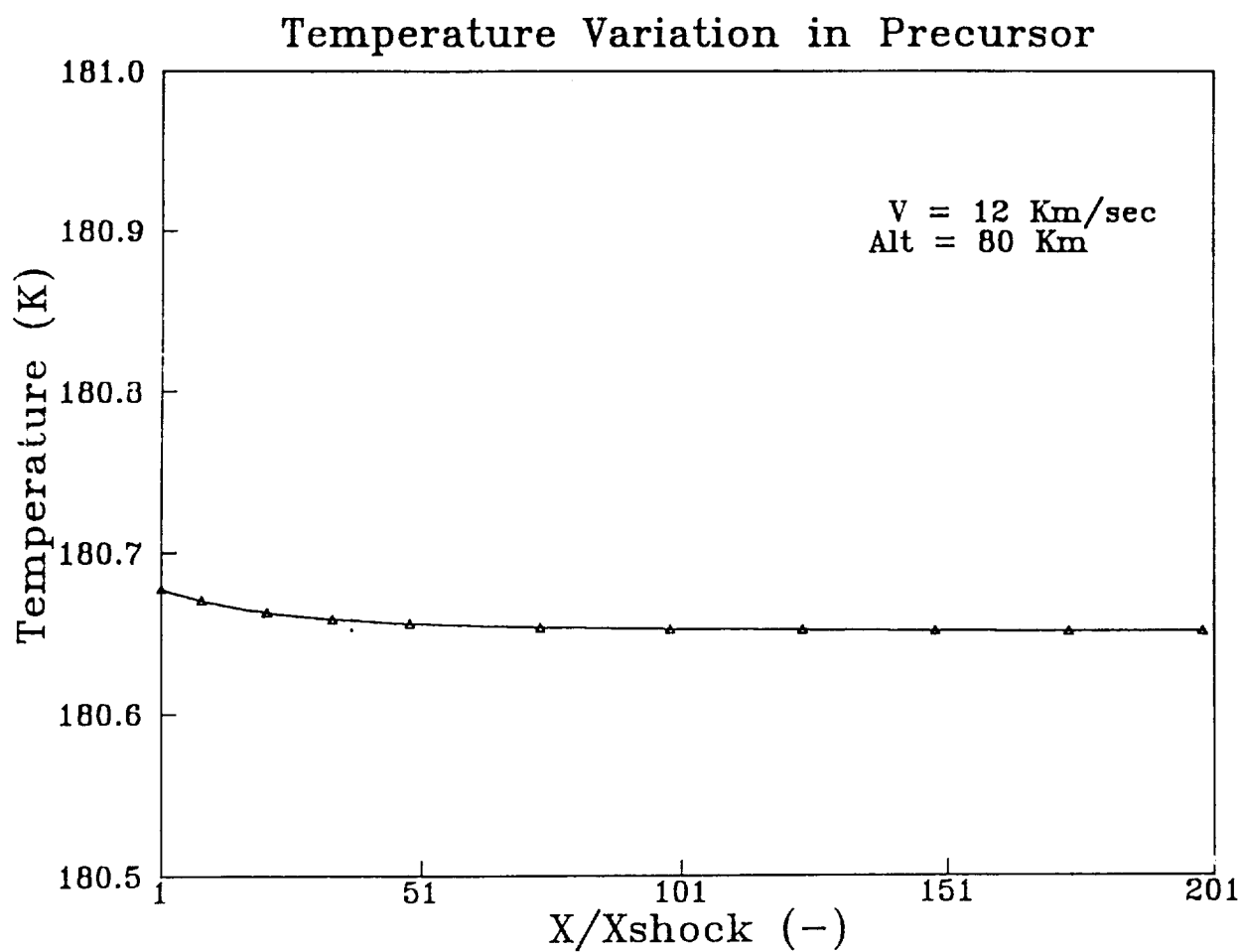


Fig. 13 -- Heavy Particle Temperature Variation in the Precursor
U = 12 km/sec, H = 80 km, Rnose = 2.3 m



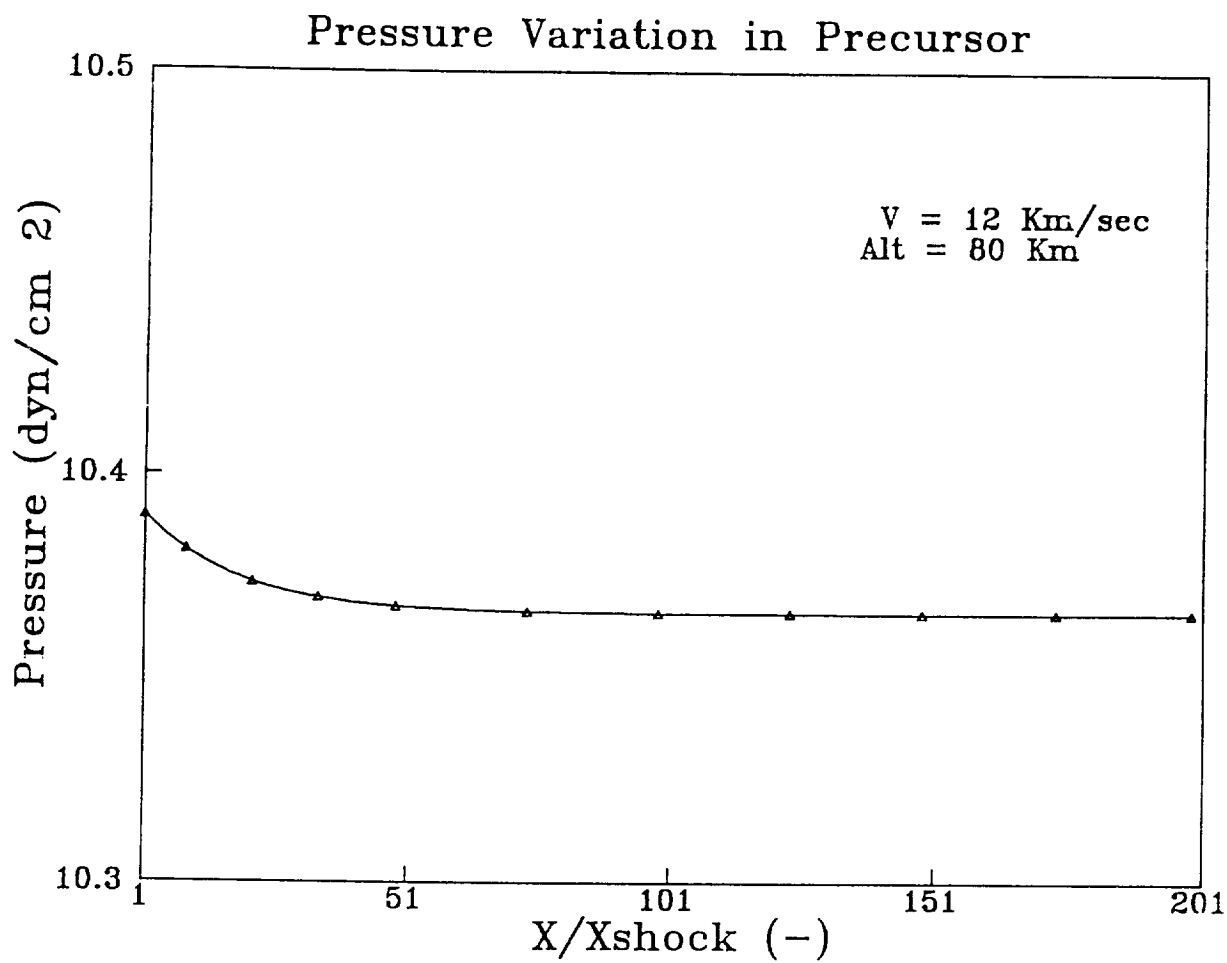


Fig. 14 -- Pressure Variation in the Precursor
 $U = 12 \text{ km/sec}$, $H = 80 \text{ km}$, $R_{\text{nose}} = 2.3 \text{ m}$



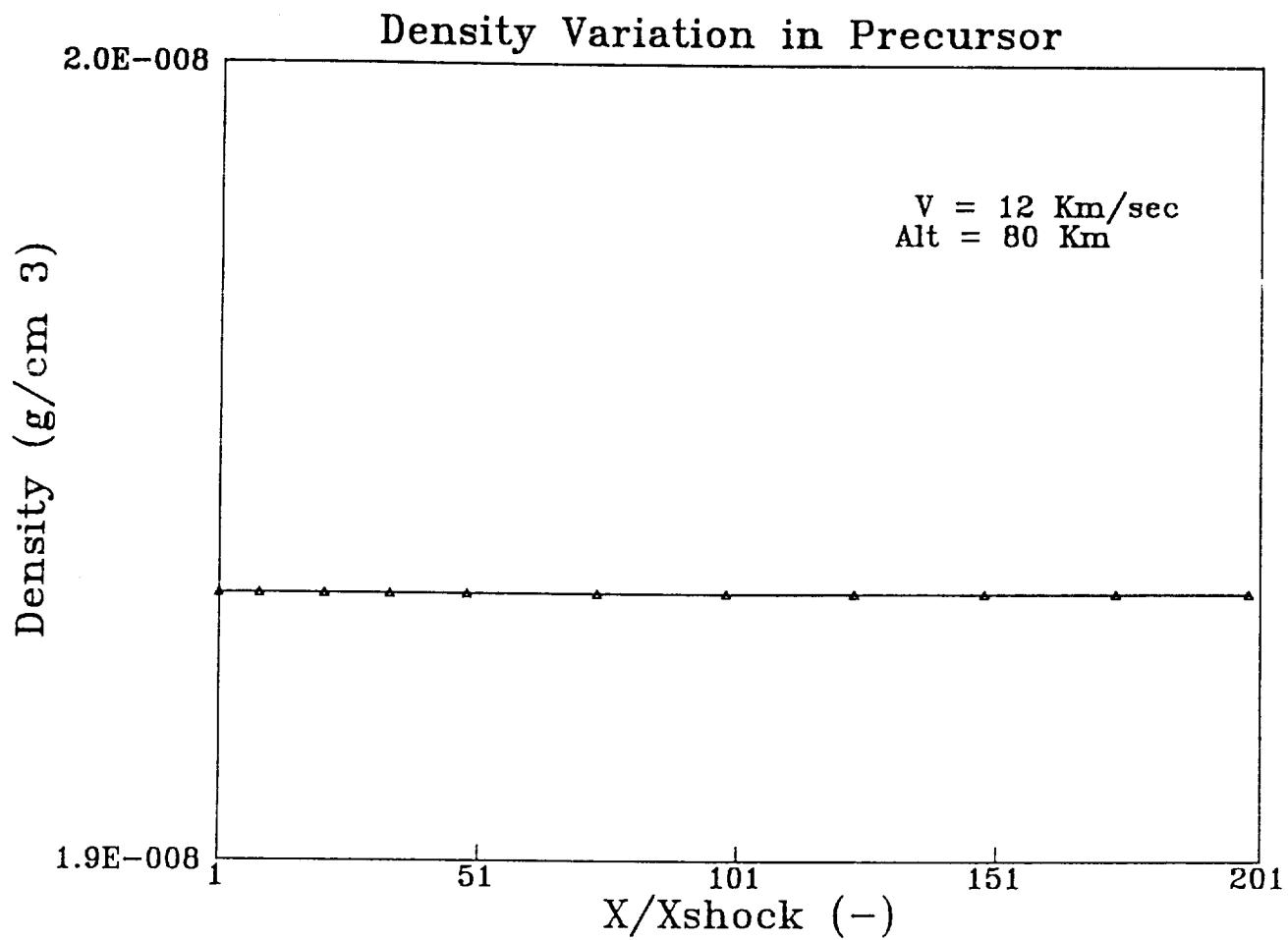


Fig. 15 -- Density Variation in the Precursor
 $U = 12 \text{ km/sec}$, $H = 80 \text{ km}$, $R_{\text{nose}} = 2.3 \text{ m}$



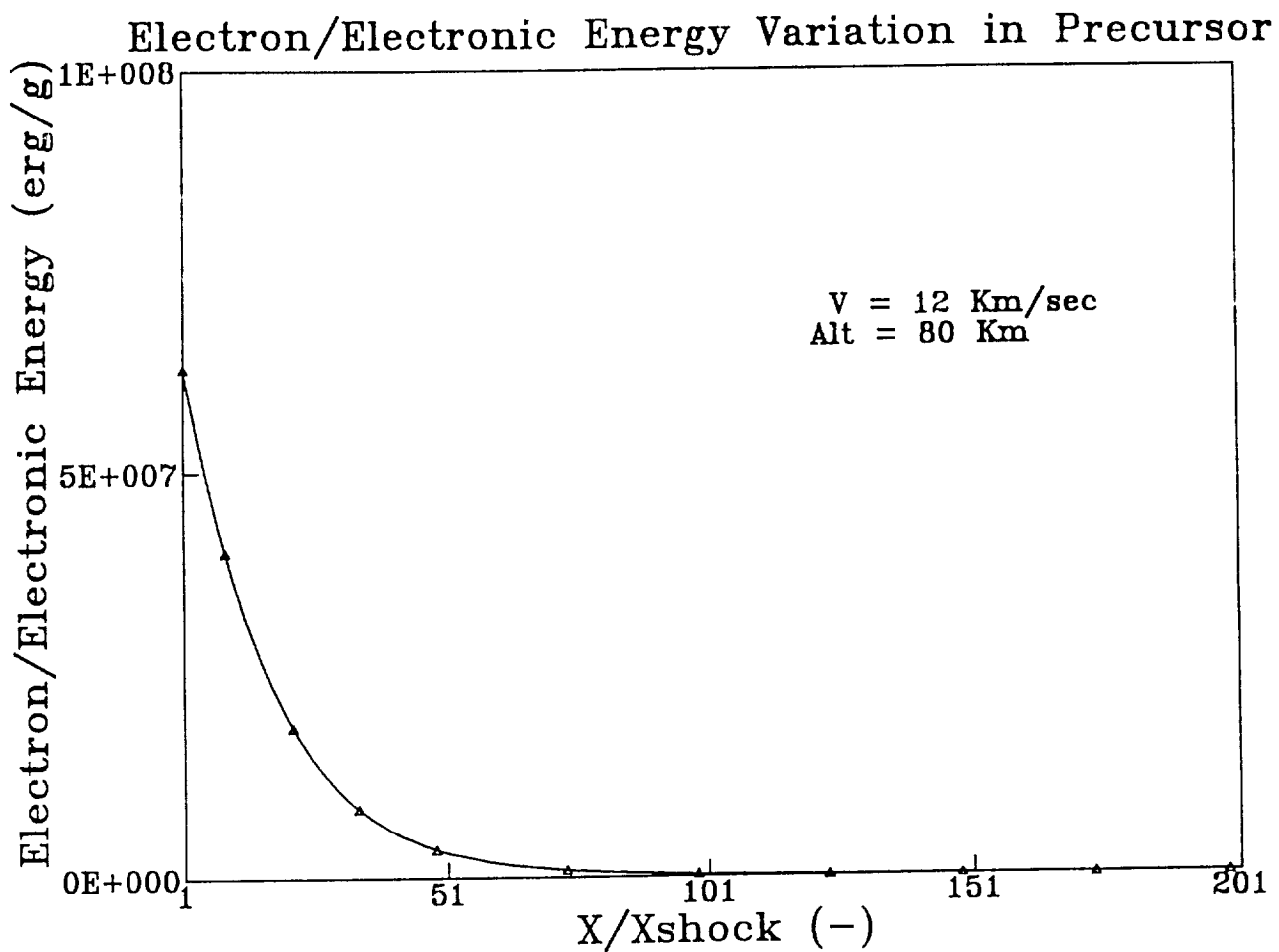


Fig. 16 -- Electron-Electronic Energy Variation in the Precursor
 $U = 12 \text{ Km/sec}$, $H = 80 \text{ km}$, $R_{\text{nose}} = 2.3 \text{ m}$



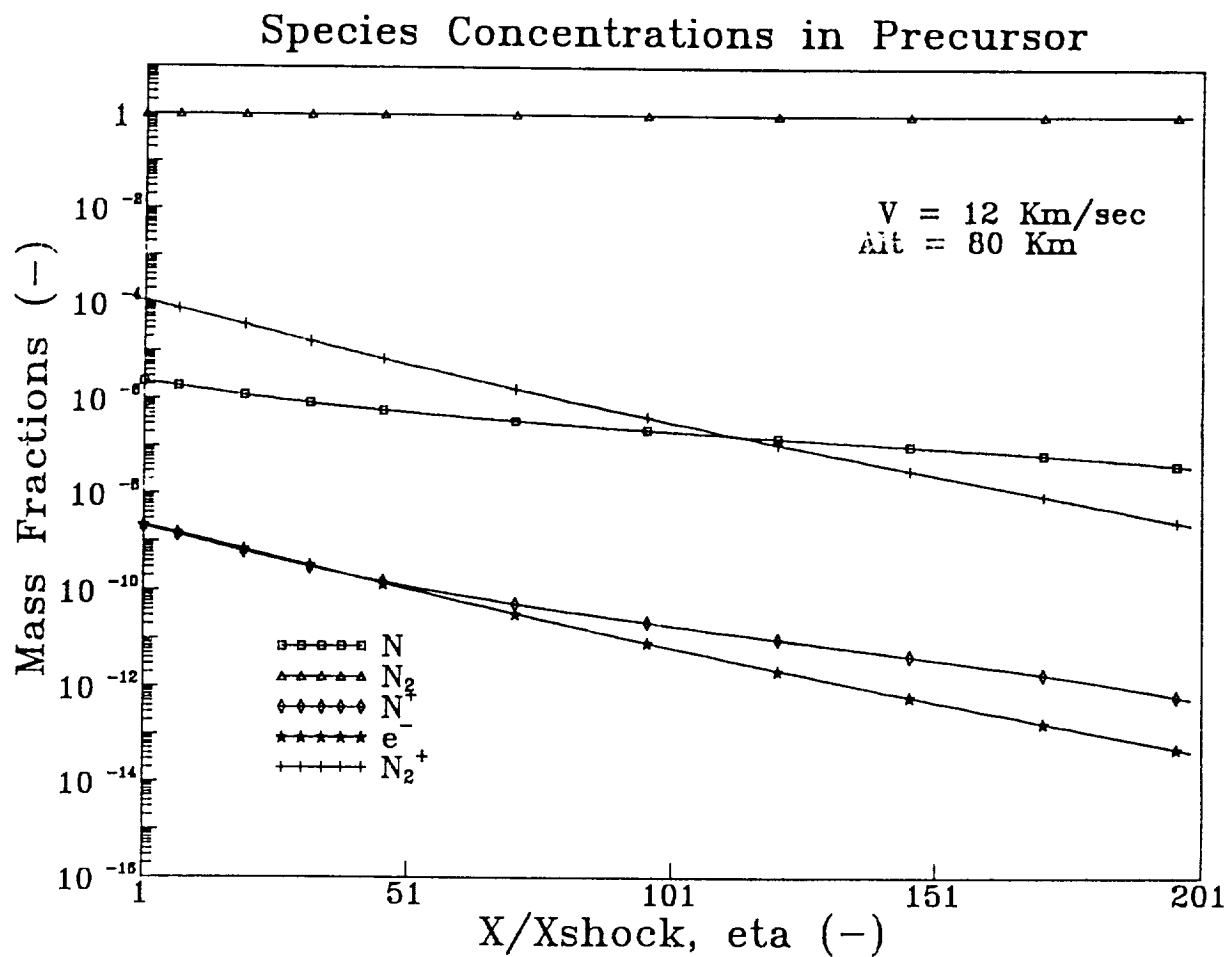
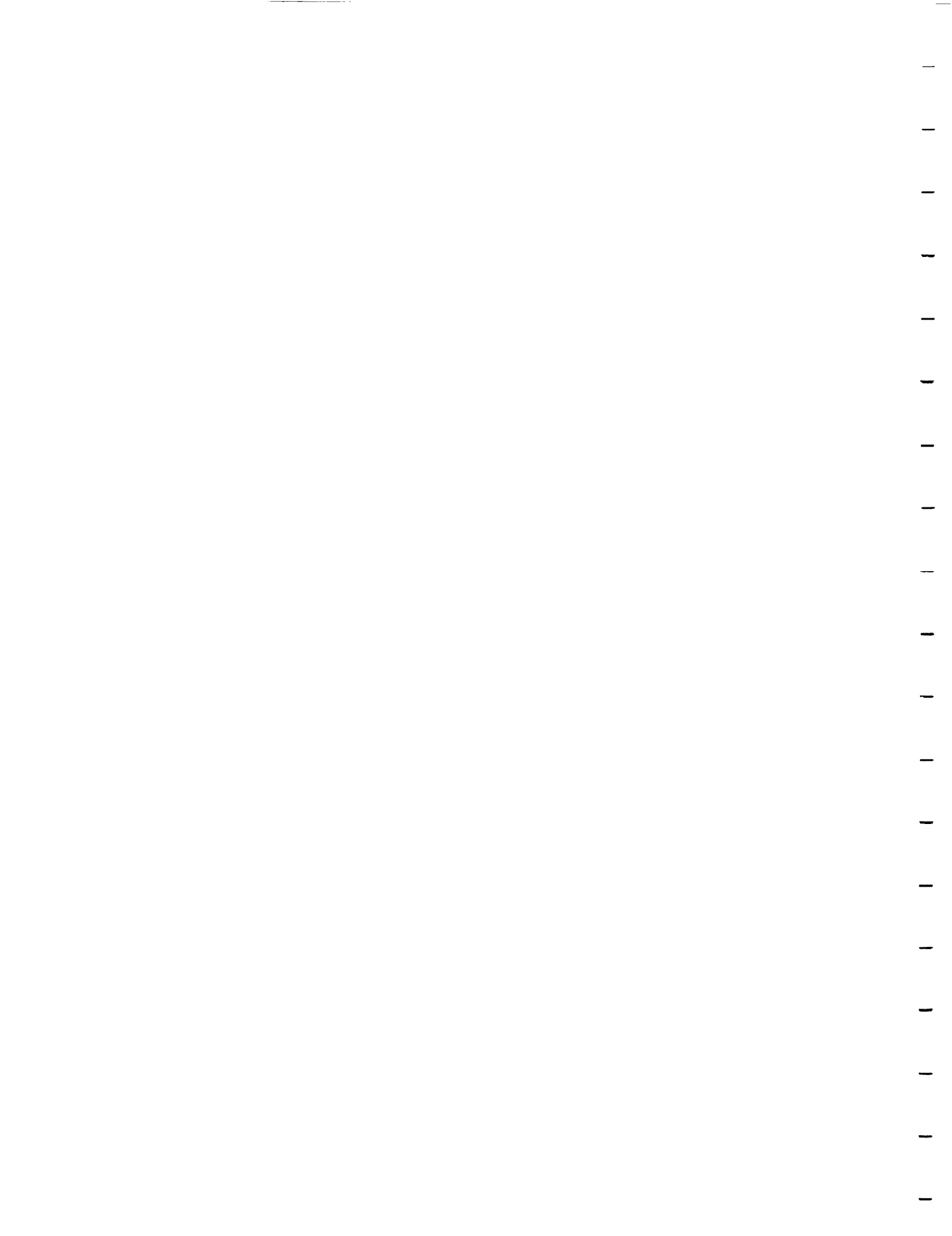


Fig. 17 -- Species Concentration Profiles for the Precursor
 $U = 12 \text{ km/sec}$, $H = 80 \text{ km}$, $R_{\text{nose}} = 2.3 \text{ m}$



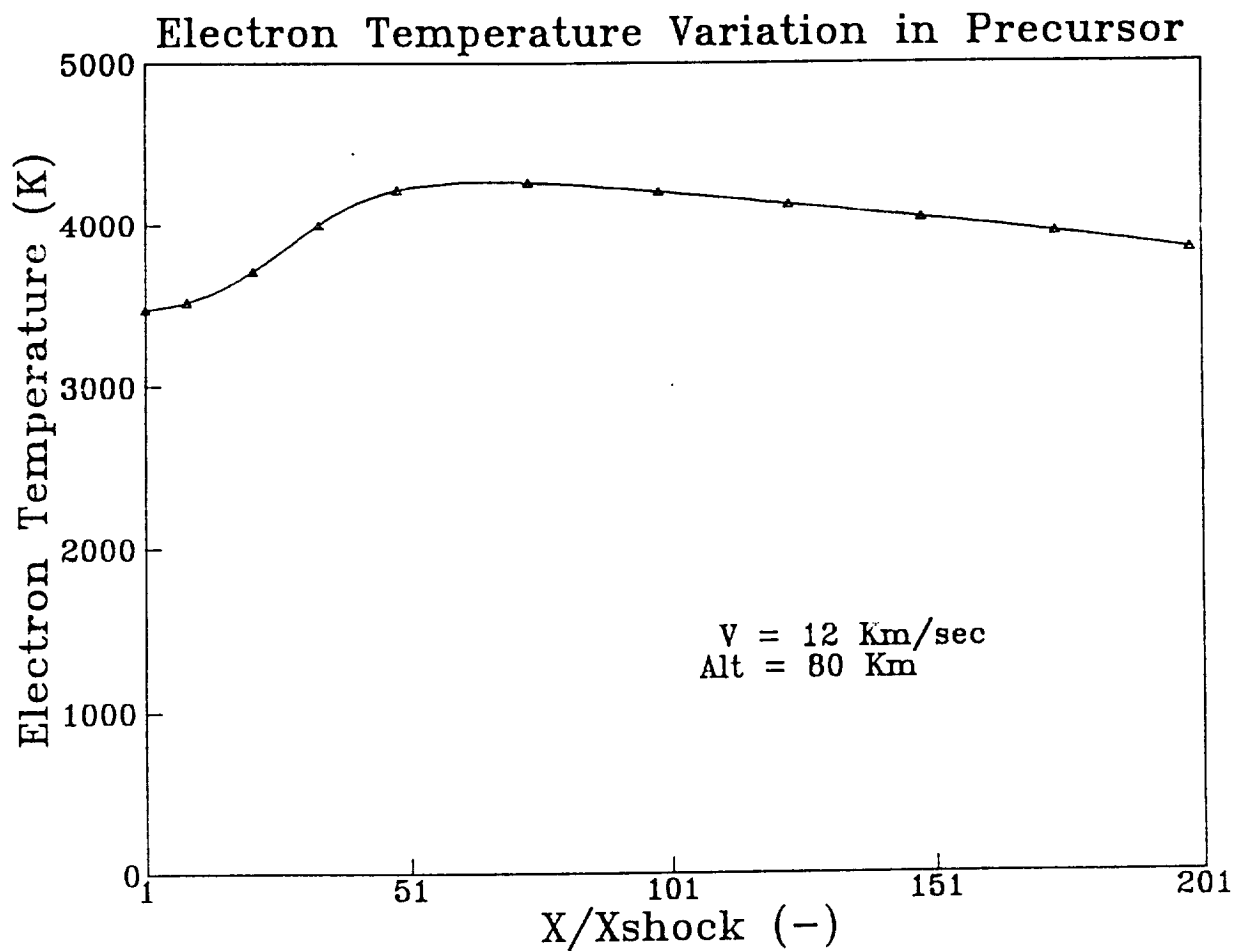


Fig. 18 -- Electron-Electronic Temperature Variation in the Precursor
 $U = 12 \text{ km/sec}$, $H = 80 \text{ km}$, $R_{\text{nose}} = 2.3 \text{ m}$

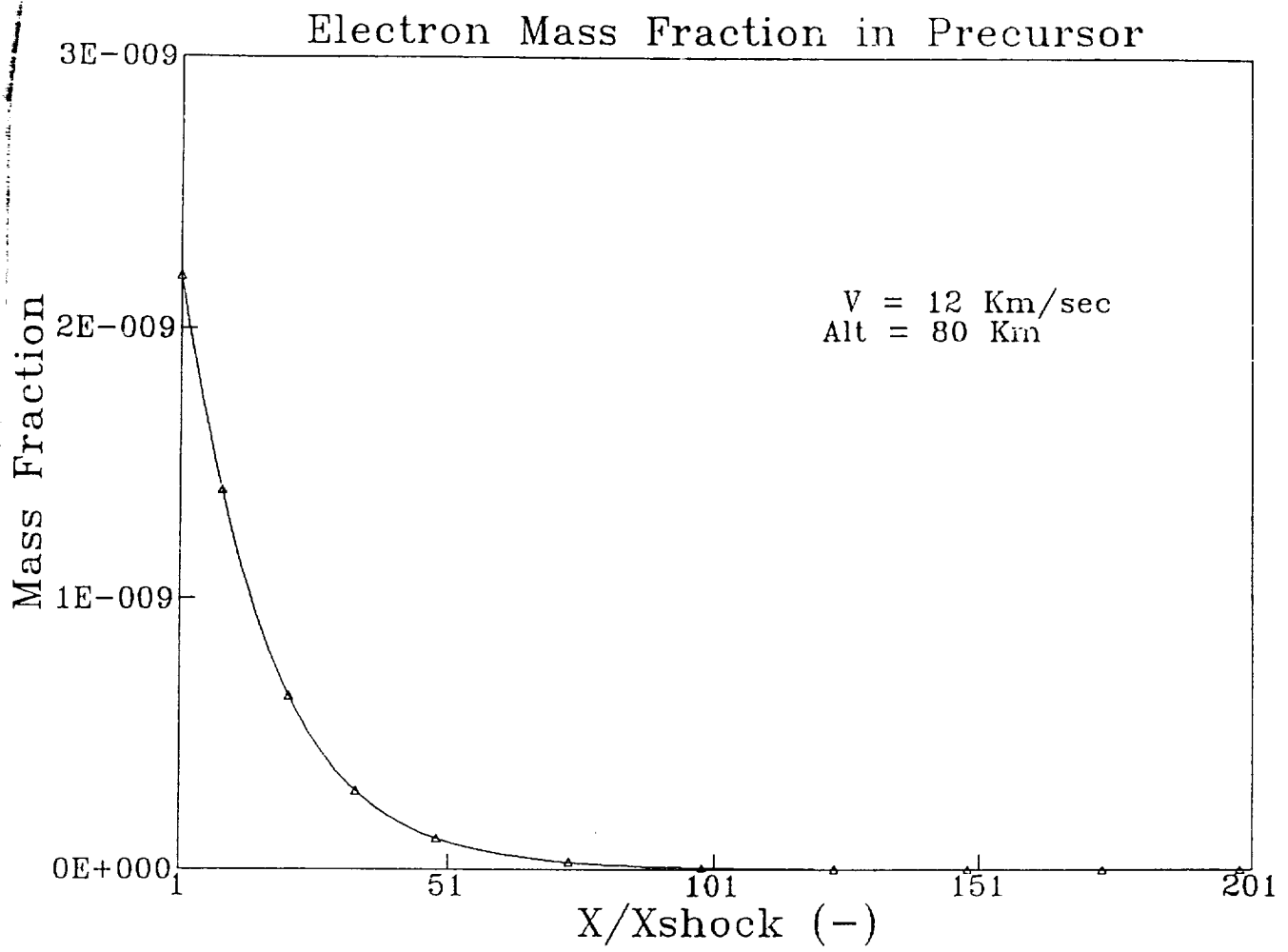
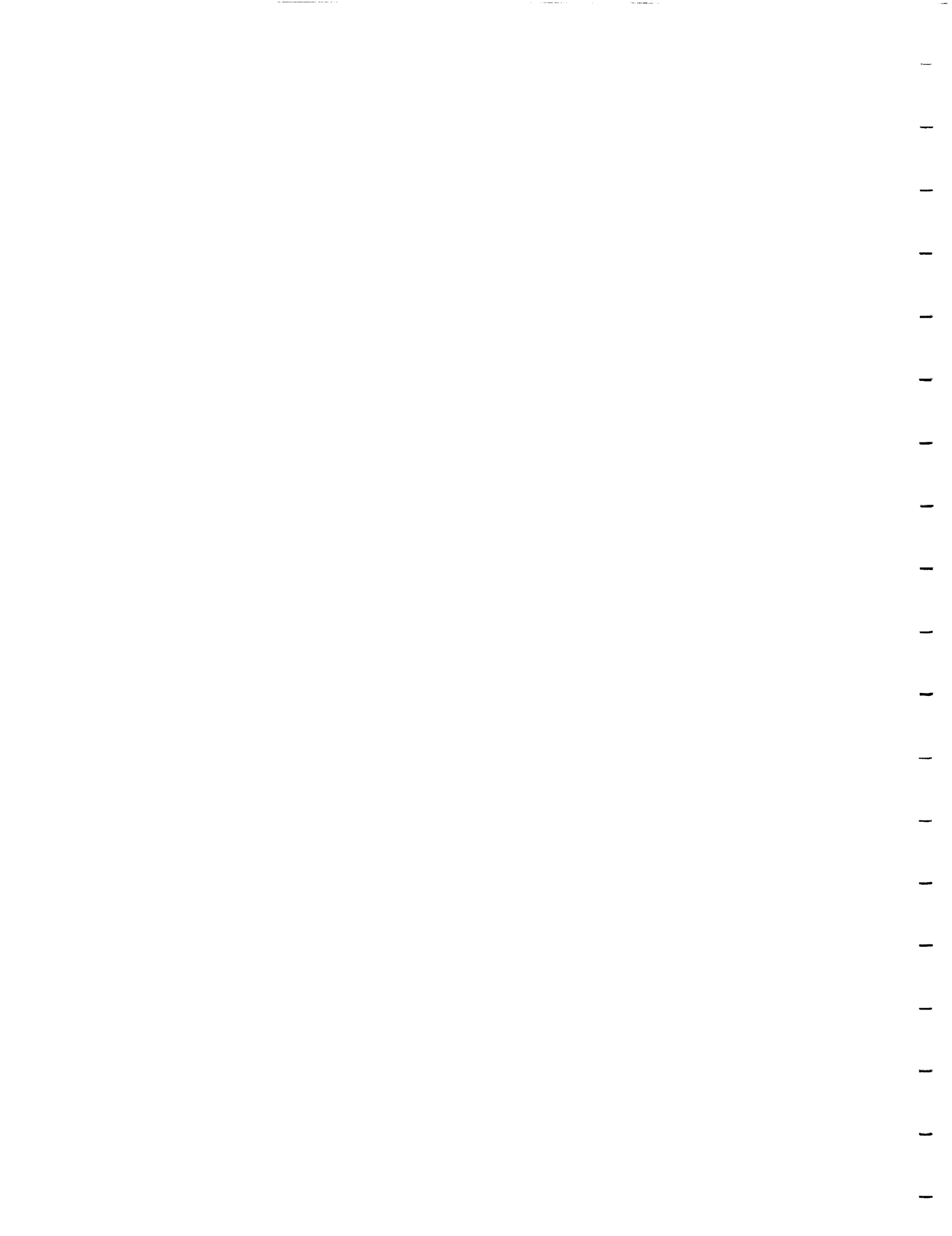


Fig. 19 -- Electron Mass Fraction Variation in the Precursor
 $U = 12 \text{ km/sec}$, $H = 80 \text{ km}$, $R_{\text{nose}} = 2.3 \text{ m}$

APPENDIX I

Abstract of Paper for January 1991
AIAA Aerospace Sciences Conference



NONEQUILIBRIUM CHEMICAL AND RADIATION COUPLING PHENOMENA IN AOTV FLOWFIELDS

AN EXTENDED ABSTRACT

Leland A. Carlson* and Thomas A. Gally**
Texas A&M University
College Station, Texas

SUMMARY

In order to investigate radiative and chemical nonequilibrium effects, flowfield solutions for a wide range of AOTV flight conditions have been obtained. These solutions have been calculated using a viscous shock layer method which includes the effects of chemical and radiative nonequilibrium, thermal nonequilibrium, viscosity, heat conduction, diffusion, and radiative-gasdynamics coupling. The effects on radiative heat transfer and flowfield properties due to radiative coupling and local thermodynamic nonequilibrium effects are shown and discussed. The variation of radiative heating rates with velocity and altitude are also presented for the different coupling and radiative nonequilibrium models investigated.

INTRODUCTION

In the future, various space programs will be conducted which will require the efficient return of large payloads to low earth orbit from missions to the moon or to planets like Mars. To accomplish this task, the return vehicles will utilize aerocapture techniques that will involve reentry and deceleration at high altitudes; and in order to design these vehicles, a thorough understanding of the physical phenomena will be required. Because of the high altitudes associated with aerocapture, the vehicle flowfields will be dominated by chemical, thermal, and radiative nonequilibrium phenomena. Thus, the primary purpose of the present study is to develop an engineering flowfield model suitable for high altitude AOTV flowfields having extensive chemical, thermal, and radiative nonequilibrium and to use this model to investigate the magnitude, extent and coupling between these phenomena.

* Professor, Aerospace Engineering Dept.

** NASA Graduate Research Fellow, Aerospace Engineering Dept.

METHODS

The flowfield model used in this investigation is a viscous shock layer analysis which includes the effects of chemical nonequilibrium, multi-temperature nonequilibrium (electron and heavy particle), viscosity, heat conduction, diffusion, and radiative-gasdynamics coupling. The basic code is the same as used for the previous study presented in Ref. (1), but a number of additions and modifications have been made since the earlier study. First, the VSL code has been coupled with the radiation analysis routines of the NASA Langley program, RADICAL², which is described below. Second, the chemical reaction rate input data has been changed to allow the use of a single reaction rate, k_f or k_b , and the equilibrium constant, K_{eq} , rather than using both the forward and backward rates. This modification was deemed necessary since the ratio of the experimentally determined rates k_f and k_b often deviates significantly from the theoretical K_{eq} . With this modification the species concentrations in the near equilibrium regions of the flowfield are now in agreement with the results predicted from strictly equilibrium analysis. Third, the effects of multi-temperatures on the shock jump conditions and thermodynamic state variables have been improved from those at the time of Ref. (1).

As mentioned, the radiation analysis package from the program RADICAL has been coupled to the viscous shock layer flowfield, giving the ability to calculate flowfield solutions with the effects of radiative cooling present. The radiation analysis in RADICAL is a detailed method which includes atomic continuum radiation, molecular band radiation, and atomic line radiation for the standard CHON (carbon, hydrogen, oxygen, nitrogen) gas system. The original method uses the species number densities and assumes a Boltzmann state distribution to calculate the excited state number densities for each species, and, from this data, the individual radiative absorption coefficients. Using the theory of excited state depletion under nonequilibrium conditions presented in Ref. (3) and Ref. (4), the present radiation analysis uses atomic local thermodynamic nonequilibrium (LTNE) radiation correction factors which account for state population deviations from that predicted by a Boltzmann distribution. A similar set of molecular corrections factors can be deduced from this theory, but the authors question the validity of applying the theory to molecular vibrational states, and an alternate method of determining molecular state populations is under development (see EXPECTED RESULTS).

More details of the flowfield and radiative methods will be presented in the final paper, including equations, relevant figures, and tables.



TYPICAL RESULTS

In this section results obtained using the nonequilibrium coupled radiation viscous shock layer model are presented. At this stage, these results are being primarily used to gain insight into the phenomena affecting the flowfield chemistry and radiation. In all cases, results are for the stagnation line, utilize fifty-one points between the shock and the wall, and the freestream is N_2 . The nonequilibrium chemistry model is the Case II Nitrogen Reaction System presented in Ref. 1, with the reverse rates being obtained via the equilibrium constants. In addition, the wall has been assumed to be a noncatalytic black body at 1650 deg K. This latter assumption has been used for convenience even though it is recognized that for many of the cases of interest that the heat transfer load will be more than adequate to induce ablation and to raise the wall temperature to values several thousand degrees higher.

AFE CFDPoint 2

This condition corresponds to what is often referred to as the "max Q" computational point for one of the initial AFE trajectories at which the freestream velocity is 8.915 km/sec, freestream pressure is 15.715 dyne/cm² and temperature is 197.101 K. For this case, the nose radius has been assumed to be 2.3 meters, and both atoms and molecules have been included in the radiation calculations. Heating results are presented in Table I and the stagnation temperature and composition profiles are shown as Figure 1.

As can be seen, the results include electron thermal nonequilibrium but they assume vibrational equilibrium. Since for the AFE vibrational nonequilibrium effects will be significant and may affect the chemistry and the radiation, it is planned to include in the near future a vibrational nonequilibrium model in the nonequilibrium radiating VSL code. However, the present results assume $T_{vN_2} = T$.

As shown on Figure 1, the electron temperature rapidly rises behind the shock front and equilibrates with the heavy particle temperature. However, as evidenced by the continual decrease in temperature and the variations in composition across the shock layer, the stagnation flow for this case is always in chemical nonequilibrium. Also, the wall thermal layer comprises approximately twenty percent of the 10.8 cm thick shock layer. It should be noted that the electron temperature and composition results shown on Figure 1 are very similar to unpublished results previously obtained for this case using the inviscid AFETE code (Ref. 5) and an earlier version of the VSL code (Ref. 1).

As would be expected for this case, the radiation coupling effects for this case are very small and cannot be detected on plots comparing uncoupled and coupled solutions. However, as shown on Table I, there is a small amount of cooling, which can be observed



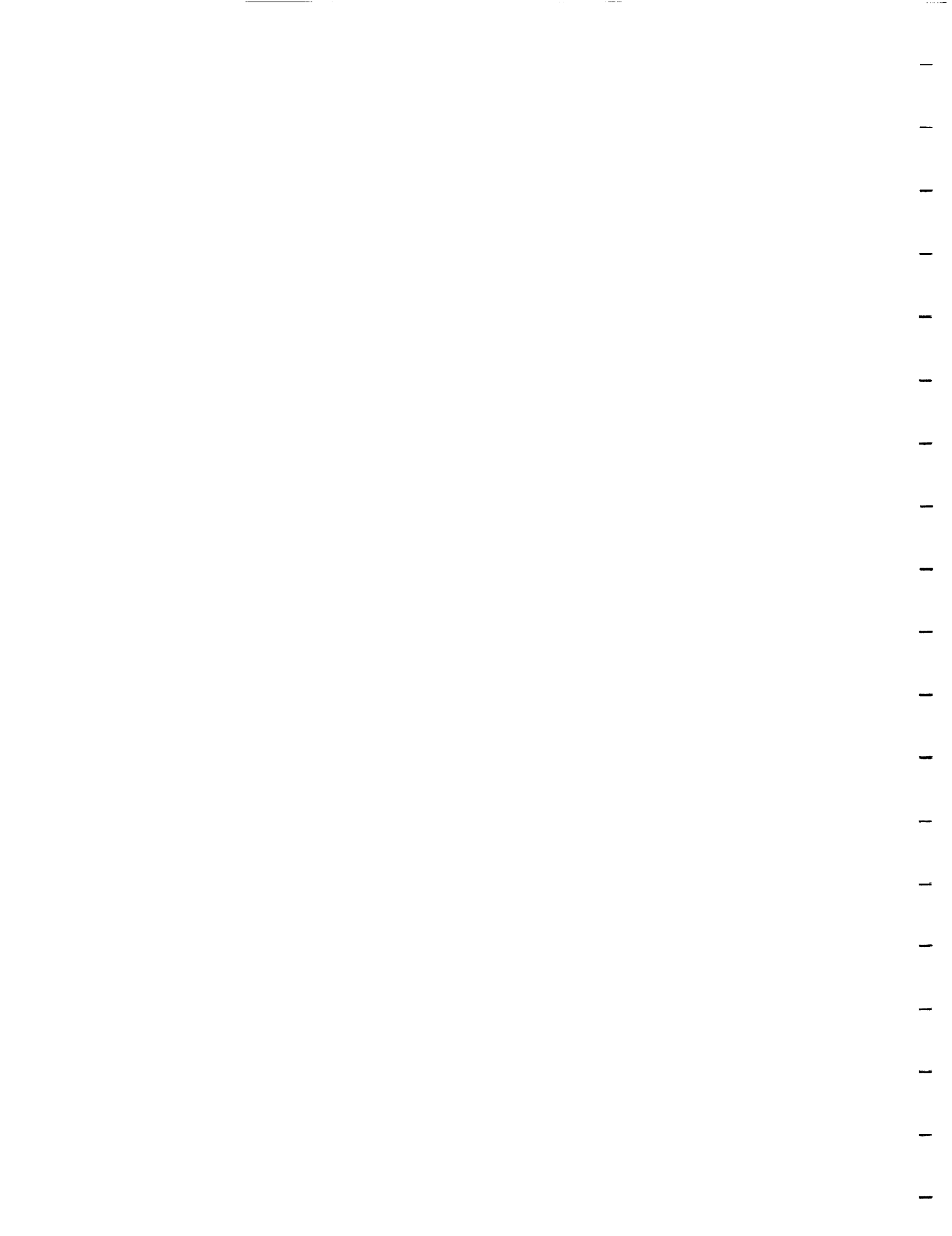
by comparing corresponding cases such as uncoupled corrected with coupled corrected etc. Also, as mentioned above, the radiative heating results for this case include molecules without any LTNE factors; and thus they should be conservative with respect to the radiative heating estimates, which range from 4.76 to 7.21 watts/cm². Note that the usage of the atomic LTNE corrections factors only reduces the radiative heating about 0.7 watts/cm², indicating that most of the radiation is probably molecular.

Since results have been obtained for this case previously using different versions of the method, the sensitivity of the results to various factors can be observed. For example, with the original VSL code, forward and reverse rate reaction chemistry, and the eight step radiation model used in Ref. (1), the non-radiation coupled results were with no LTNE corrections 29.7 watts/cm² and 22.4 watts/cm² with atomic LTNE corrections only. For these cases the electron temperature profile in the nonequilibrium zone was slightly higher than those shown on Figure 1 due to the influence of different reaction rates. On the other hand, after shock jump and enthalpy changes involving electron temperature were incorporated but before the forward and reverse rates were replaced with the forward rate and an equilibrium constant, the results for columns (3) and (4) of Table I were, using RADICAL, 15.9 and 12.6 watts/cm² respectively. Thus, radiative heating results are sensitive to small details in the methods, the radiation model, and in particular to the chemistry and electron temperature. It should be noted that the change from forward and reverse rates to only a forward rate and a computed equilibrium constant significantly changed the equilibrium temperature and composition.

Since the results shown on Figure 1 and Table 1 for this case are in better agreement with the detailed inviscid results obtained using AFETE than previous VSL values and since they have been obtained using better models, they are probably reasonable estimates. However, the effects of vibrational nonequilibrium and chemical nonequilibrium on molecular radiation have yet to be included. Nevertheless, since the latter effects should most likely reduce radiative heating, the presents estimates may be conservative.

AFE CFD Point 4

It is believed that this condition corresponds to a "max Q" computational point for an AFE trajectory associated with a heavier vehicle at which the freestream velocity is 9.326 km/sec, freestream pressure is 26.4 dyne/cm² and temperature is 200 K. For this case, the nose radius has also been assumed to be 2.3 meters, and both atoms and molecules have been included in the radiation calculations. Heating results are presented in Table I and the stagnation temperature and composition profiles are shown Figure 2, for which the shock layer thickness is 10.5 cm.



As can be seen, these results are very similar to those for the CFD Point 2 case, and the remarks concerning that case apply equally well here. In general, the predicted heating rates, which do not include molecular nonequilibrium radiation factors, are higher than those for CFD Two.

U = 14.5 km/sec, Altitude = 65 km

In a recent paper (Ref. 6) results have been presented for the stagnation line of a one meter nose radius body at a trajectory point possibly representative of an earth entry return from Mars. These results include chemical nonequilibrium, thermal nonequilibrium assuming that vibrational, electronic, and electron nonequilibrium can be represented by a single temperature, and uncoupled nonequilibrium radiation computed by a detailed model that includes the molecular continuum and atomic lines.

Using this model, the investigators obtained for this trajectory point an uncoupled radiative heating rate of 1700 watts/cm², a shock standoff distance of 5.7 cm, and a post-shock chemical nonequilibrium zone 1.1 cm thick. In this nonequilibrium zone, the electron-vibrational temperature never significantly exceed the equilibrium temperature. They also stated that most of the radiative heating was from the ultra-violet below 2000 Å, that it originated from the nonequilibrium region behind the shock wave, and that very little was absorbed in the wall thermal layer. The latter is different from previous beliefs by some researchers (Ref. 7), but it is in agreement with the approximate studies of Carlson (Ref. 3).

In addition, in Ref. 6 comparisons were made with results obtained using the RASLE code (Ref. 8), which is an equilibrium viscous shock layer code using a radiation model also based upon RADICAL. Using the RASLE code, Ref. 6 obtained for the same case a shock standoff distance of 3.5 cm and a radiative heating rate of 970 watts/cm². The authors attributed the differences to nonequilibrium chemistry effects and the RASLE radiation model, asserting that the latter smeared atomic lines and therefore obtained incorrect results.

Considering these discrepancies, it is believed that it would be valuable to apply the present model to this trajectory point; and temperature and composition profile results for the case including radiative cooling are presented in Figure 3. For this case, the shock standoff distance is 3.4 cm; and, as can be seen, most of the shock layer is in chemical equilibrium.

The difference in shock standoff distance between the present results and those of Ref. 6 is believed to be primarily due to the electron temperature profile and its subsequent effect on chemistry. In Ref. 6, T_e is low in the region behind the shock front, possibly due



to combining electron-electronic with vibrational phenomena. However, as shown in the composition profiles, diatomic species are insignificant over most of the shock layer and ionization dominates the chemistry. Thus, in the present case, an electron temperature model which is strongly influenced by collisional and ionization phenomena is used. Figure 3 shows that the result of using such an approach is an electron temperature which in the nonequilibrium zone behind the shock front significantly exceeds the shock layer equilibrium temperature. Since the dominant ionization mechanism behind the shock front is electron-atom collisions (Ref. 1) that are governed by the free electron temperature, this enhancement of T_e accelerates ionization, shortens the chemical nonequilibrium zone to about 0.4 cm, and decreases the overall shock layer thickness. It should be noted that this result shows the strong sensitivity of the overall solution to the electron temperature model at such trajectory points.

Radiative heating results obtained with the present model are shown on Table I. Since at these conditions the radiative transfer should be dominated by atomic processes and since for the predicted shock layer temperatures nitrogen should be a reasonable model for air (Ref. 9), these results, which have been obtained utilizing only atomic processes corrected for LTNE effects, should be appropriate. As can be seen, the predicted stagnation point radiative heat transfer for the case without any radiation gasdynamic coupling is 1691 watts/cm², which is in remarkable agreement with the corresponding prediction of Ref. 6. It should be noted, however, that the present results indicate that most of the radiation originates from the high temperature equilibrium portion of the shock zone and not from the nonequilibrium part as postulated in Ref. 6. In the post-shock region, chemical nonequilibrium induces local thermodynamic nonequilibrium and depopulates the excited states rapidly via ionization, with the result that very little radiation originates in the nonequilibrium region.

Moreover, the radiation coupled results for this case indicate significant radiation cooling is present. This cooling is evidenced not only by the decrease in radiative heating to 1039 watts/cm² but also by the temperature and ionization profiles on Figure 4. These figures compare the uncoupled and coupled results; and as shown by the steady decrease in temperature and in particular ionization throughout the equilibrium zone, radiation cooling for this case is significant and needs to be included in an analysis model.

As mentioned, the RASLE prediction for this case was 970 watts/cm². However, it is probable that the difference between this value and the present prediction is primarily due to the influence of reaction chemistry and the amount of absorption in the wall thermal layer. Since RASLE assumes equilibrium chemistry, it should predict more molecules in the wall layer and hence more absorption. This possibility is borne out by the fact that the

RASLE results (Ref. 6) indicate that the wall thermal layer absorbs about 32% of the wall directed radiation while the present model indicates only about 15% is absorbed. Thus, it appears, that while most of the shock layer is in chemical equilibrium for this case, that chemical nonequilibrium effects may still be important and affect the radiative heating. In addition, it should be noted that the equilibrium chemistry formulation (i.e. forward and reverse rates or forward rate combined with equilibrium constant) strongly affects the heating results for this case. The results shown all used the forward rate combined with an equilibrium coefficient formulation.

It is mentioned above that Ref. 6 indirectly criticizes the RADICAL model, stating that it improperly handles line radiation by smearing the lines and that as a result it should give incorrect answers. Unfortunately, this assertion may be the result of a misinterpretation of the RADICAL radiation model and output. For convenience, RADICAL groups the radiative transfer into various wavelength regions and gives appropriate average values for these regions; and it is these values which are frequently plotted to show the variation of say wall radiative heating with wavelength or electron volts. An example of such a plot for the present case is shown on Figure 5, and at first glance it would appear that RADICAL does indeed smear lines to a significant extent. However, in the actual computation of the radiative transfer, RADICAL actually does for most line groups perform a line by line integration; and the final result is actually the consequence of such a detailed calculation.

When the results of the detailed RADICAL computation are plotted for the radiative flux to the stagnation point for this case, they appear as shown on Figure 6. Here a semi-log abscissa has been used in order to more vividly display the underlying continuum radiation as well as the lines. As can be seen, there are strong lines in the infrared region below 4 eV and in the ultra-violet between 7 and 11 eV. However, in the vacuum ultra-violet above 11 eV many of the lines are actually absorbing part of the continuum flux as evidenced by the plots dropping below the continuum level. This absorption is also evident on Figure 7 where the stagnation heating is plotted versus wavelength. Here the line absorption of the continuum radiation is very evident around 0.1 microns as is the underlying continuum.

In general, the results shown on Figures 5-7 are very similar to Figures 3 and 4 in Ref. 6. However, careful comparison indicates that the present results have significant radiation above 11 eV primarily due to free-bound continuum processes, while those of Ref. 6 have little or no flux in this region. In Ref. 6 this difference is attributed to the usage of the smeared band line model in RADICAL; but, as shown on Figures 6 and 7, RADICAL does include the lines in detail in this region, and most of the radiation above 11 eV is due to the continuum, not the highly absorbing lines. This fact, combined with the absence of any significant radiation between 4 and 6 eV (.2 to .3 microns) in the results presented in Ref.



6, indicates that possibly Ref. 6 treated atomic continuum radiation differently. Thus, the seemingly good agreement between the methods may actually be serendipity and require further study.

Radiation Model Comparisons

Considering the possible sensitivity of various flowfield cases of interest to the radiative heating, it has been decided to compare several available radiation models and, if possible, evaluate the accuracy of RADICAL. For these comparisons, the following models have been used - (1) RADICAL, (2) NEQAIR (Ref. 10), (3) and a modified 8-step band model based upon Ref. 11. Unfortunately, complete spectral comparisons have not been possible since NEQAIR does not automatically include absorption effects while RADICAL and the 8-Step model do. Thus, it has been decided to exclude the highly absorbing ultra-violet region and to limit the comparisons to the, by comparison, transparent visible and infrared region above 2000 Å. In addition, since LTNE factors are still under development, the comparison cases have assumed a constant temperature and pressure slab with the composition determined by the equilibrium calculation in RADICAL. For RADICAL and NEQAIR the gas has been considered to be air, while for the 8-Step model it has been considered equilibrium nitrogen at the same temperature and pressure. The results of the calculations are presented in Table II

As can be seen, the results of all three models are in very good agreement with the total variation in each case only being about 10 percent. This agreement is not really surprising since previous studies (Ref. 3-4) have shown that most models agree well in the visible and infrared. Thus, such comparisons and similar comparisons with experimental data in the visible and infrared are probably not very definitive. Nevertheless, considering that RADICAL agrees with other models and considering that it has been extensively compared to experimental data over a wide range of conditions (Ref. 2 and 12), it is believed that RADICAL is an excellent and adequate radiation model for the present research. In other words, the problems with predicting AOTV flowfields are not associated with the primary radiation model. Instead the difficulties are a result of the sensitivity to chemistry, electron temperature modeling, LTNE factors, etc

Velocity Effects at 80 km

Results have also been obtained for three different velocities, 12, 14, and 16 km/sec, at an altitude of 80 km. These velocities are, depending upon the trajectory chosen, within the possible range of entry velocities associated with a Martian return vehicle. In all cases, the results are for the stagnation line of a 2.3 meter nose radius vehicle, the freestream is nitrogen, and only atomic radiation is considered.



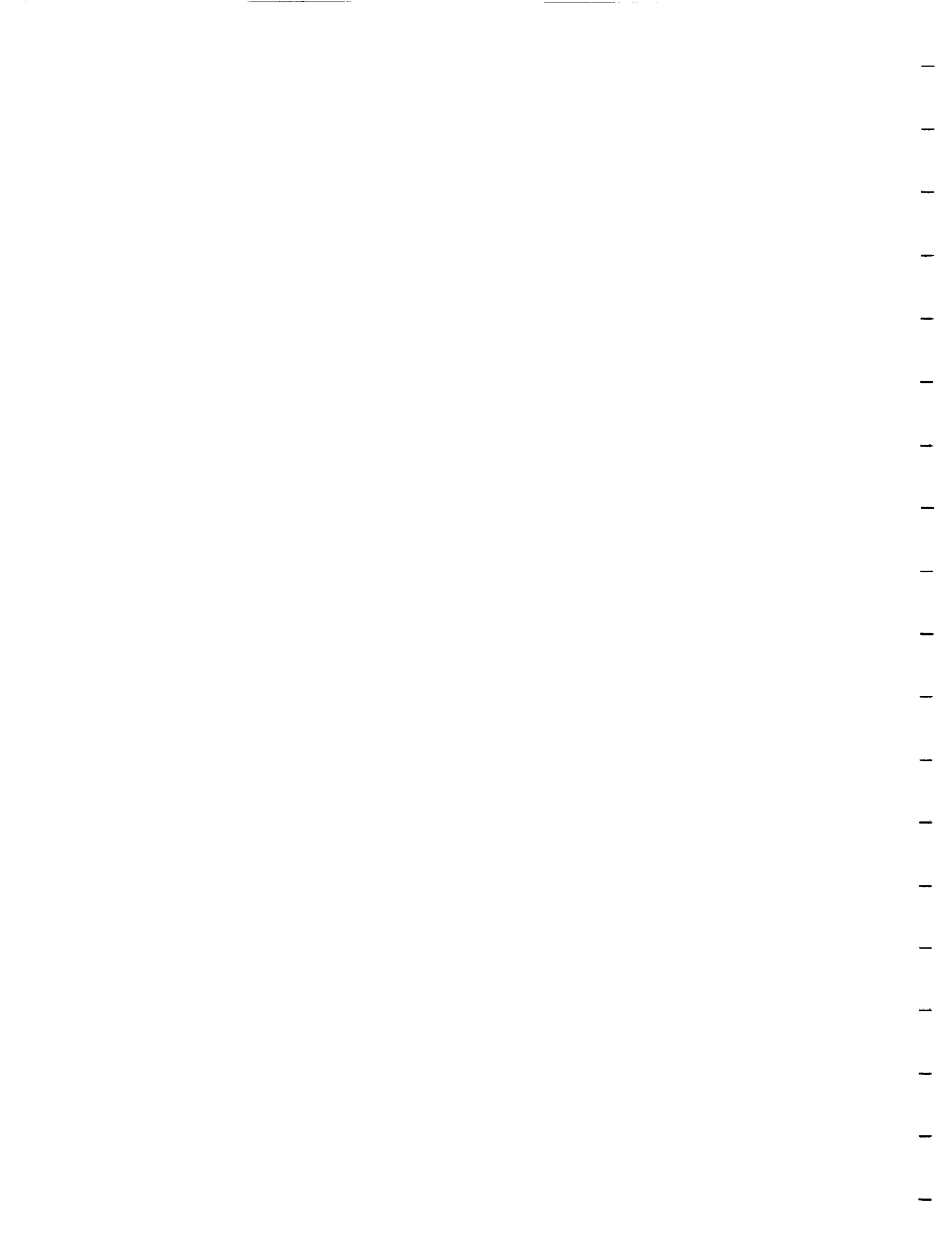
The temperature and composition profiles for the 12 km/sec case are shown on Figure 8, and the radiative heating rates are listed in Table I. As can be seen on the figure by the continually decreasing temperature and the variation in the N^+ concentration, the entire shock layer at this flight condition is in chemical nonequilibrium. Immediately behind the shock front, which for the coupled case including LTNE factors is 10.7 cm from the wall, the electron temperature rises to a value several thousand degrees Kelvin above the expected equilibrium temperature and then gradually equilibrates with the heavy particle temperature. In the wall thermal layer, which comprises about 20% of the shock layer, deionization and recombination processes are important.

By comparing the uncoupled uncorrected radiative heating for this case with the uncorrected coupled result, it is apparent that for the uncorrected radiatively coupled situation, which assumes that electronic states are populated according to a Boltzmann distribution, that there is significant radiation cooling. While not shown, comparison of uncorrected and corrected profiles indicates that this cooling occurs in the outer portion of the shock layer where the electron temperature is high. On the other hand, the corrected results, which include LTNE factors, shows only slight radiation coupling or cooling.

Results were also obtained earlier using a version of the code which utilized both forward and reverse rates instead of a forward rate and an equilibrium expression. In those cases, the level of ionization was about 50% higher and the temperature profiles, particularly in the region near the shock front were different in that the electron temperature was higher. As a consequence, the radiative heating rates comparable to those in Table I were a factor of two to three higher. This difference was primarily due to the higher electron temperature, and again demonstrates the sensitivity of radiative heating to composition and electron temperature.

Interestingly, the radiative heating value of 9.44 watts/cm^2 predicted for the situation including radiation coupling and LTNE effects is remarkably close to the 10.5 watts/cm^2 previously predicted for this case (Ref. 1). The latter was obtained using an earlier version of the model before the shock jump and chemistry improvements were incorporated. In addition, it used the 8-Step radiation model instead of RADICAL. However, the old shock jump conditions yielded a lower heavy particle temperature behind the shock front, which when combined with the older chemistry model predicted a very similar electron temperature profile. As a consequence, the heating rates were similar. Again, the sensitivity of radiative heating to electron temperature is evident.

The temperature and composition profiles for the 14 km/sec case are shown on Figure 9, and the radiative heating rates are also listed in Table I. Since the freestream velocity is higher, the nonequilibrium zone behind the shock front is shorter than at 12 km/sec,



occupying only the outer 50% of the 8.7 cm thick shock layer. Nevertheless, the flow is dominated by a nonequilibrium chemistry zone, composed primarily of N , N^+ , and e^- , and the wall thermal layer. While N_2^+ peaks behind the shock front, it is very small over most of the shock layer. In addition, as can be seen in Table I, there is in the uncorrected case extensive radiative cooling. As shown on Fig. 9a, the profiles for various cases indicates that for the uncorrected case that the cooling occurs primarily in the nonequilibrium region behind the shock front where the electron temperature is highest.

However, for the corrected cases the inclusion of LTNE nonequilibrium effects significantly decreases the radiation from the nonequilibrium portion of the shock layer since in those cases ionization processes deplete rapidly the excited atomic electronic states. As a result, while there is radiative cooling, what there is occurs in the equilibrium portion of the shock layer between Y/Y_{shock} of 0.2 and 0.6. In addition, the present results indicate that LTNE phenomena reduce the radiative heating by about 80% for this flight condition.

Finally, with respect the 14 km/sec case, it should be noted that the same trend exists as in the 12 km/sec case with respect to the sensitivity to the old and new reaction rate treatments. As before, the electron temperature is higher in the nonequilibrium zone with the old formulation; and the radiative heating is approximately a factor of two higher.

The temperature and composition profiles for the 16 km/sec case are shown on Figure 10, and the radiative heating rates are again listed in Table I. Here, the electron temperature immediately behind the shock front is very high, having a peak value in the corrected coupled case of slightly over 20,000 K, as is the amount of ionization, which is about 60%. Likewise, due to the increase in velocity, the nonequilibrium zone is somewhat shorter. In this case it is about 30-40% of the 7.32 cm shock layer.

As would be expected, the radiative heat transfer results have the same trend as those for 14 km/sec. The uncorrected cases exhibit significant radiation coupling and cooling, with almost all of the cooling occurring from the nonequilibrium portion of the shock layer through the shock front due to the very high electron temperature in that zone. This type of behavior is consistent with that shown in Ref. 3 in that reference's study of the sensitivity of the flowfield to radiation parameters. On the other hand, when LTNE effects are included (corrected results), the radiative cooling is significantly less. As before, it occurs primarily in the equilibrium portion of the shock zone.

A graphical summary of the 80 km radiative heating results is presented as Figure 10a. From this figure it is easy to see the tremendous effects the inclusion of LTNE corrections has on the total heat transfer for all three flight velocities. Also evident is the much lower amount of radiative coupling present in the LTNE corrected flows as compared to the



uncorrected flows.

Finally, for all three flight velocities, the predicted radiative heating is significant compared to the convective heating; and, in the 16 km/sec case, the radiative heating exceeds the convective prediction by 70%. While the latter is only approximate in that only 51 points have been used in these calculations and that the wall has been assumed fully noncatalytic, it is probably reasonably accurate. Also, since it is anticipated that advanced heat shield materials can withstand only up to 70 watts/cm² without ablating, these results indicate that at 80 km ablative heat shields would be required on 2.3 meter nose radius vehicles at velocities of 14 km/sec and above.

U = 16 km/sec Altitude = 75 km and 72 km

In order to investigate altitude effects and to determine the difficulty of using the model under a situation on a "large" vehicle where much of the shock layer is in equilibrium, results have been obtained for the 2.3 meter radius body at 16 km/sec at 75 and 72 km. The composition and thermal profiles for 75 km are displayed on Figure 11, and in this case it can be seen that due to the lower altitude the chemical nonequilibrium zone is shorter occupying only about 15-20% of the shock layer. Likewise the entire shock layer is as a result of the higher pressure and density thinner than at 80 km, having a thickness of 6.8 cm in the coupled corrected case.

Further, as shown on Table I, even in the corrected case including LTNE effects there is significant radiative cooling. While difficult to detect on Figure 11, this cooling does affect the composition and temperature profiles in that the temperature is steadily decreasing in the "equilibrium" zone between 20 and 80%. Also, the degree of ionization actually peaks at Y/Y_{shock} of 0.85 and then due to cooling decreases by 50 percent before the effects of the wall thermal layer are encountered around $Y/Y_{\text{shock}} = 0.2$. Finally, it should be noted that for this case, the radiative heating dominates the problem and exceeds the convective rate by a factor of almost five.

The stagnation profiles at 72 km are shown on Figure 12; and at this altitude the predicted shock layer thickness is 6.6 cm, only slightly smaller than the value at 75 km. However, due to the increased pressure, the post-shock nonequilibrium chemical relaxation zone is considerably shorter at about 0.75 cm.; and the radiative heat transfer is approximately a factor of two larger at 758 watts/cm². Further, the temperature profile in the equilibrium zone is steadily decreasing; and the ionization level peaks at the end of the chemical relaxation zone and then decreases due to radiative cooling throughout the rest of the shock layer. This radiative coupling effect can be observed in the concentration profiles by noting the steady decrease in $[N^+]$ and increase in $[N]$ from the end of the



nonequilibrium chemistry region at $Y/Y_{\text{shock}} 0.9$ to the beginning of the wall thermal layer around 0.15. Thus, for this case radiation coupling effects are important and do affect the temperature and composition of the shock layer.

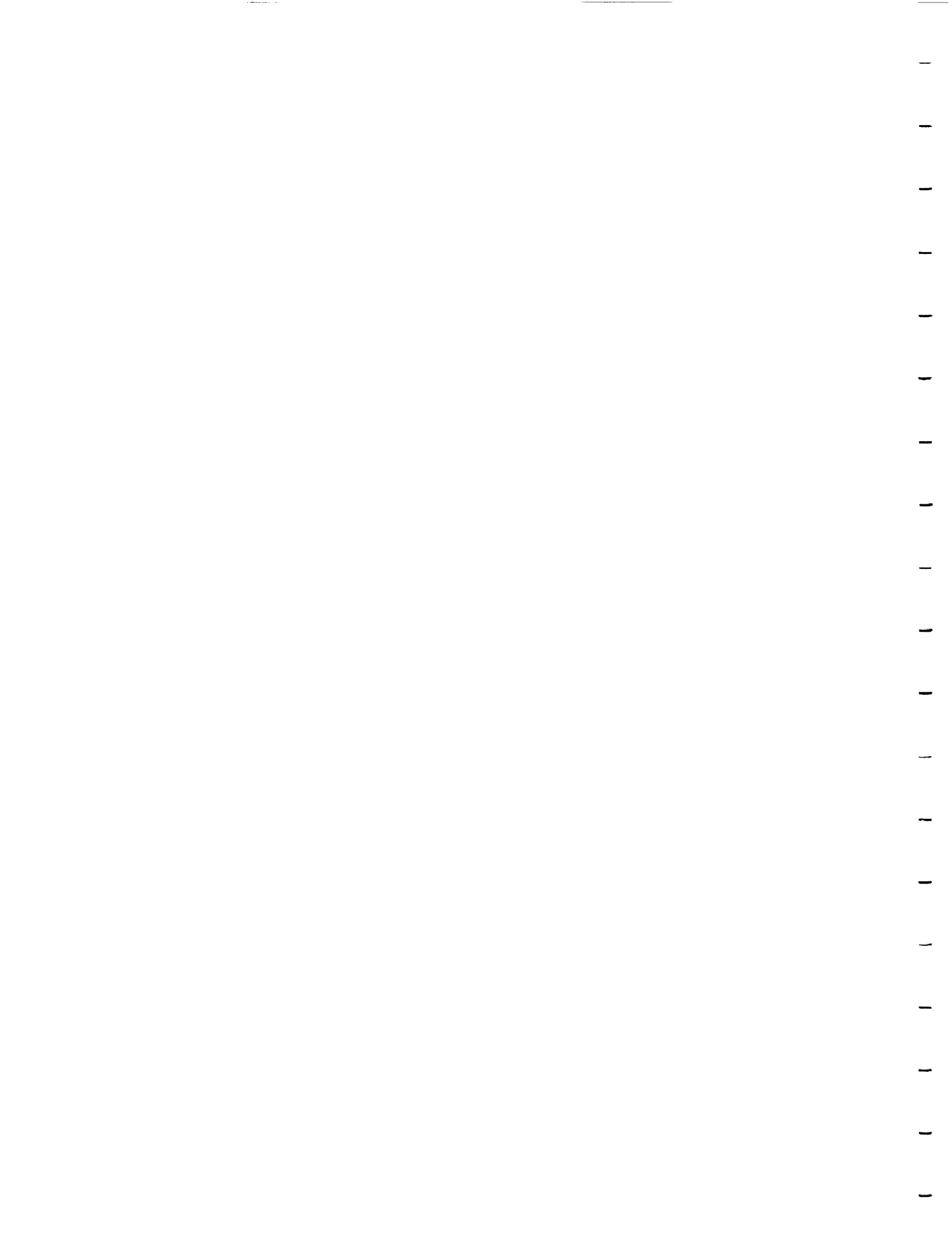
The trends in radiative heating with altitude for the above 72 km and 75 km cases along with the previous 80km case at a freestream velocity of 16 km/sec are shown in Figure 12a. Again, the importance of including the effects of coupled radiative cooling in the calculation of radiative heat transfer for this high speed case is evident.

Comparison with Inviscid Equilibrium Results

Even though a significant portion of any AOTV earth entry will be at altitudes where viscous and chemical nonequilibrium effects should be important, it is believed that it would be instructive to compare results obtained with the present model with inviscid equilibrium results. Such comparisons should indicate the validity of the present model and the limitations of equilibrium inviscid analysis predictions. As a result a limited number of cases have been computed in order to compare with the inviscid equilibrium tabular results of Sutton. The latter were obtained using a radiatively coupled solution of the inviscid flow equations at the stagnation point of a hemisphere and used RADICAL as the radiation model. This method has been compared extensively to ground test and flight measurements as described in Ref. 12. In comparing the Sutton values with the present results, it should be recognized that in addition to the inviscid-viscous and equilibrium-nonequilibrium differences, the Sutton results were obtained for air while the present values assumed a freestream of nitrogen and only include atomic radiation at this point.

In this comparison effort, four cases have arbitrarily been selected; and these are listed on Table III along with the inviscid equilibrium results. The corresponding viscous nonequilibrium heat transfer results are given in Table I, and the shock layer profiles are presented in Figures 12 - 15.

In general, the heating predictions from the two methods are of the same order of magnitude; and the shock standoff distances are similar. However, there are interesting differences. First, the shock standoff distances from the VSL nonequilibrium solutions are usually less than those obtained in the inviscid equilibrium cases. In the viscous nonequilibrium situation, the nonequilibrium zone behind the shock front has a lower than equilibrium density, which would tend to cause the shock layer to be thicker than in the equilibrium case. On the other hand, the wall thermal layer has a very high density due to the assumed cool wall temperature, which would cause the shock layer to be thinner. Apparently for the cases considered, the effects are counterbalancing with the result that the viscous nonequilibrium shock layer thickness is slightly less than the inviscid equilibrium



result.

The second interesting point is that in all cases the nonequilibrium viscous radiative heat transfer is less than the corresponding equilibrium inviscid value. In the nonequilibrium case, LTNE phenomena significantly reduces the radiation originating in the chemical nonequilibrium region behind the shock front and the cool temperatures in the wall thermal layer reduce radiation from that zone. Since the shock layer thicknesses are similar, these effects reduce the radiation heat transfer prediction to values below the equilibrium results.

In spite of the differences between the viscous nonequilibrium and inviscid predictions, it appears that the present results are reasonable and demonstrate the importance of including viscous, and chemical and radiative nonequilibrium effects in the AOTV flight regime.

EXPECTED RESULTS

In addition to the above results, the following additions and/or modifications to the flowfield code and radiation code currently being considered and are expected to be included in the final paper. First, the present approximation for the electron temperature will be replaced by a complete electron-electronic energy equation fully consistent with the approximations inherent to the VSL method. Since the added terms will be of lower order magnitude than the current terms being included, the current solution scheme will not be modified, but the new terms will be added explicitly as corrections or perturbations to the approximate method. The authors feel that the quasi-equilibrium equation currently being used is an accurate approximation and do not expect the new results to differ significantly from the current results.

In addition to the existing atomic LTNE correction factors currently used in the radiation calculations, the authors plan to have a similar set of molecular radiation correction factors incorporated. Past research into molecular radiation has included such factors which were calculated in a manner directly analogous to the atomic correction factors. The authors now question the accuracy of corrections factors calculated in such a manner given the relatively even spacing of the electronic energy levels in such molecules as N_2 , the current belief of many researcher in a strong coupling between free electrons and vibrational energy, and the effectiveness of pre-dissociation and reverse pre-dissociation in the depopulation and population of the excited electronic states, respectively, as compared to collisional dissociation. As an alternative to the previously used method, the authors are presently including a quasi-steady state model into the radiation calculations to calculate the actual individual electronic excited state populations.



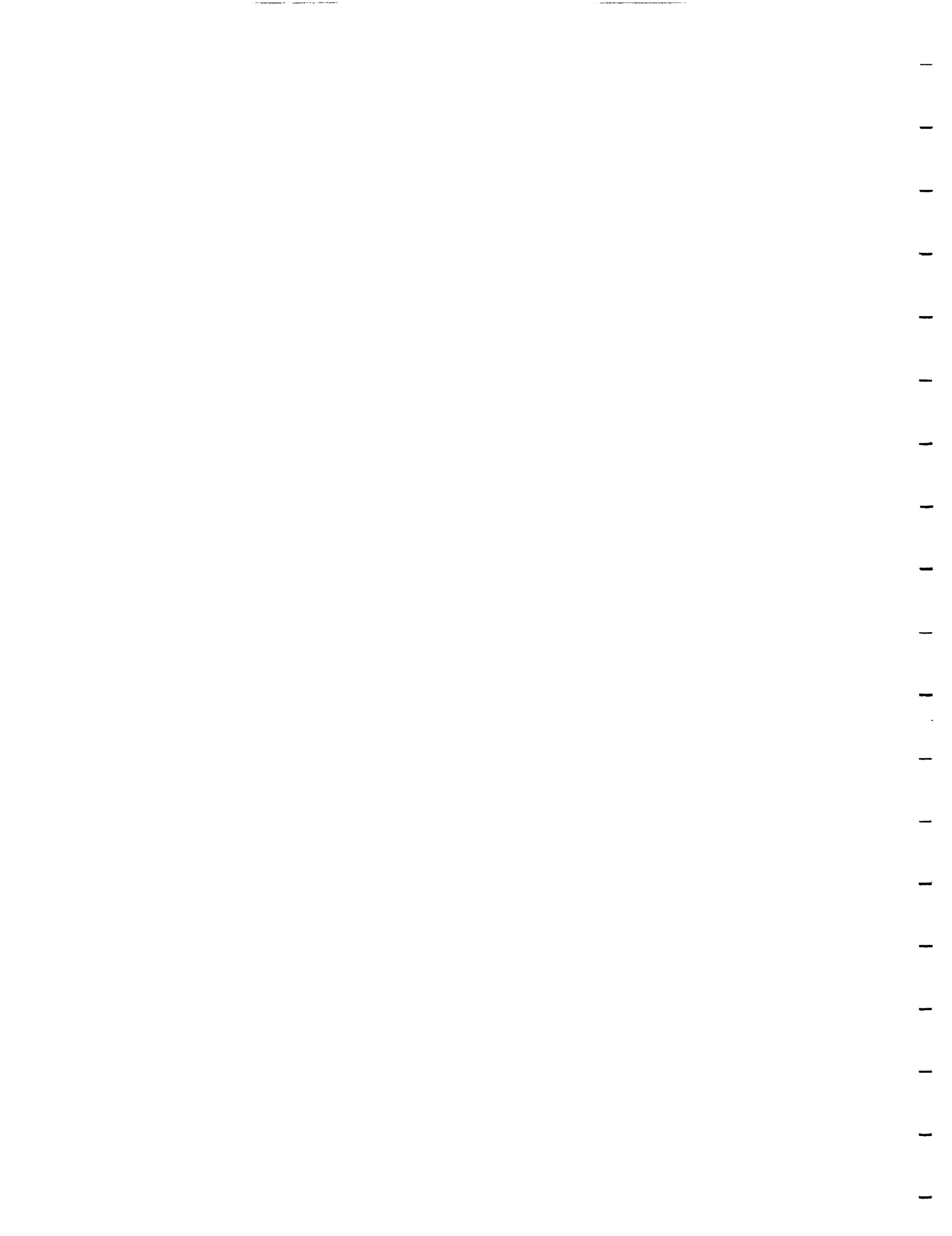
Another on going effort is being made to include a vibrational energy model, T_{vib} , into the VSL flowfield code. At the higher flight velocities associated with lunar and martian returns the inclusion of a separate vibrational equation has not been deemed necessary due to the fast dissociation of the diatomic species near the shock front. For the lower speeds associated with some orbital transfer operations and the AFE flight experiment, a separate vibration equation will allow more accurate prediction of the nonequilibrium, relaxation phenomena behind the shock.

Also planned for inclusion in the final paper are cases for an air freestream gas mixture rather than just nitrogen, solutions at various FIRE 2 trajectory points, comparisons to the FIRE flight data, and at least one full face solutions for a AFE type configuration.

CONCLUSIONS

While the present viscous nonequilibrium model still needs development and improvement in many areas, it, even in its present form, offers several advantages over other existing techniques. First, it includes viscous and chemical nonequilibrium effects. Second, it is reasonably computationally efficient with respect to both time and resource requirements. Third, it utilizes a detailed radiation model, RADICAL, which accounts for the molecular continuum, atomic lines, and atomic continuum phenomena. Fourth, this model has been modified so that the effects of local thermodynamic nonequilibrium on the radiative transfer are included in the computation of the atomic radiation phenomena. Finally, fifth, the model includes multi-temperature effects in both the nonequilibrium chemistry and radiation models by computing via a free electron equation model an electron temperature. It is believed that this approach to the computation of radiation and chemistry effects is applicable for those AOTV entries for which diatomic species are insignificant over most of the shock layer.

Flowfield solutions obtained with this model show a number of important dependancies upon the approximations and formulations. The current use in this model of a single reaction rate and the theoretical equilibrium constant to describe each chemical reaction was chosen to insure the proper species concentrations at equilibrium. but had a secondary effect on the magnitude of radiation due to a significant change in electron densities from the earlier k_f - k_b model. The inclusion of an electron-electronic energy equation shows the presence of an electron temperature overshoot in the nonequilibrium region near the shock. This overshoot will inturn result in a large pulse of radiant energy from that region unless the effects of nonequilibrium thermodynamics are included, in which case the bulk of the radiation is emmitted in the near equilibrium regions of the flow profiles and the total radiative heat transfer to the wall is much less.



Consequently, the present study demonstrates that the prediction of high altitude aerocapture vehicle flowfields is strongly dependent upon the details of nonequilibrium chemistry, nonequilibrium radiation, and electron temperature profiles. In addition, the present results indicate that these phenomena are in many cases highly coupled and interdependent. Finally, the present results show that for many cases of interest in aerocapture that radiative gasdynamic coupling is significant and that this coupling is strongly influenced by radiative and chemical nonequilibrium. The final paper will delineate these regions and the extent of coupling in more detail.

REFERENCES

1. Carlson, L. A. and Gally, T. A., "The Effect of Electron Temperature and Impact Ionization on Martian Return AOTV Flowfields," AIAA Paper 89-1729, June 1989.
2. Nicolet, W. E., "Advanced Methods for Calculating Radiation Transport in Ablation Product Contaminated Boundary Layers," NASA CR - 1656, September 1970.
3. Carlson, L. A., "Approximations for Hypervelocity Nonequilibrium Radiating, Reacting, and Conducting Stagnation Regions," J. of Thermophysics and Heat Transfer, Vol. 3, No. 4, October 1989, pp. 380-388.
4. Carlson, L. A., Bobskill, G. J., and Greendyke, R. B., "Comparison of Vibration Dissociation and Radiative Transfer Models for AOTV/AFE Flowfields," J. of Thermophysics and Heat Transfer, Vol. 4, No. 1, January 1990, pp. 16-26.
5. Carlson, L. A., "Computational Fluid Dynamics and Aerothermodynamics - Final Report," Texas A&M Research Foundation Report No. 5671-89-01, March 1989.
6. Park, C. and Milos, F. S., "Computational Equations for Radiating and Ablating Shock Layers," AIAA Paper 90-0356.
7. Park, C., "Assessment of Two Temperature Kinetic Model for Ionizing Air," AIAA Paper No. 87-1574, June 1987.
8. Nicolet, W. E., Waterland, L. R., and Kendall, R. M., "Methods for Predicting Radiation Coupled Flowfields about Planetary Entry Probes," Aerodynamic Heating and Thermal Protections Systems, AIAA Progress in Astronautics and Aeronautics, Vol. 59, Ed. by L. S. Fletcher, AIAA, 1978, pp. 120-136.
9. Knott, P. R., Carlson, L. A., and Nerem, R. M., "A Further Note on Shock Tube Measurements of End Wall Radiative Heat Transfer in Air," AIAA Journal, Vol. 7, November 1969, pp. 2170-2172.
10. Park, C. "Nonequilibrium, Air Radiation (NEQAIR) Program: User's Manual," NASA TM B6707, July 1985.



11. Olstad, W. B., "Nongray Radiating Flow About Smooth Symmetric Bodies,"
AIAA Journal, Vol. 9, January 1971, pp. 122-130.

12. Sutton, K., "Radiation Revisited," AIAA Paper 84-1733, June 1984.

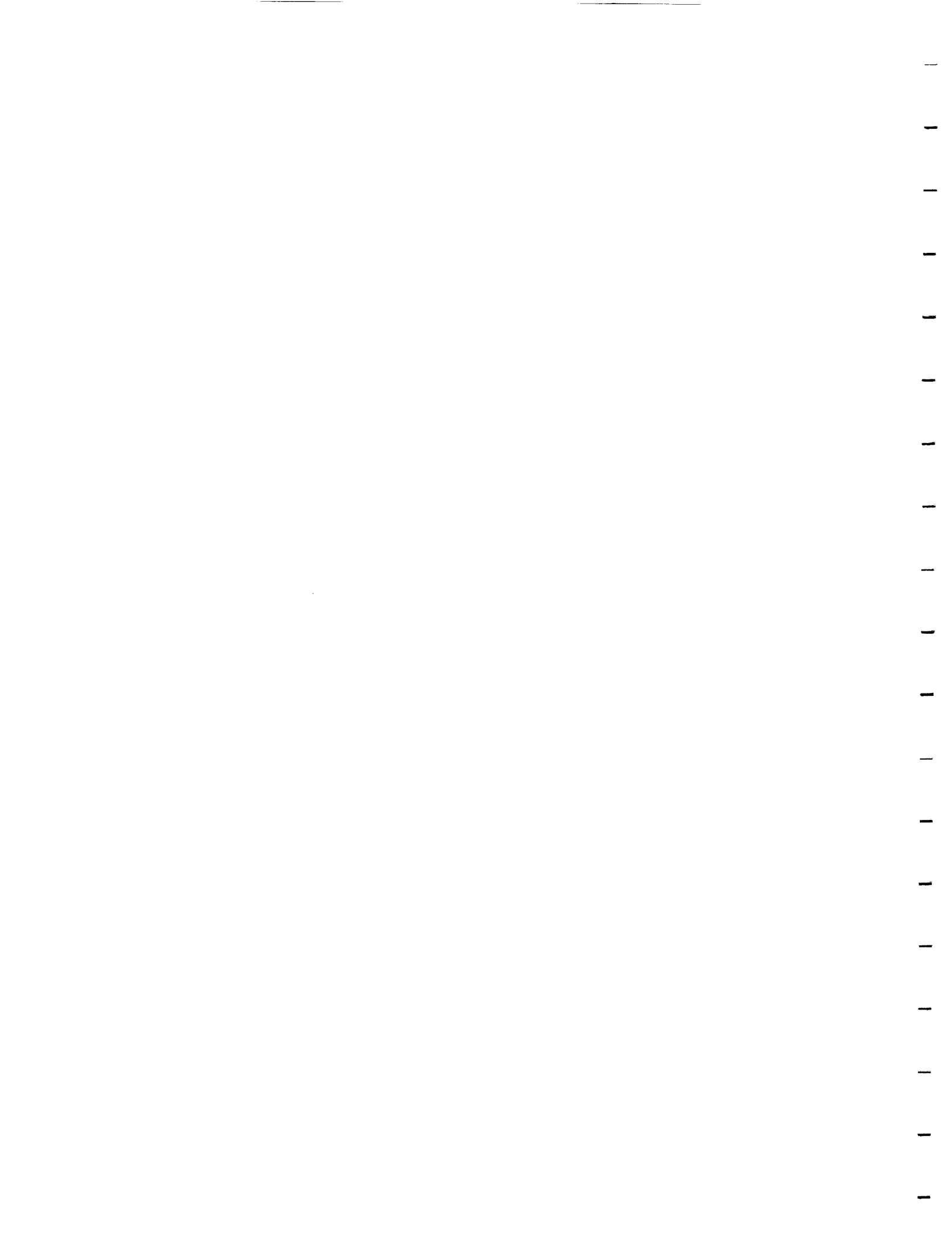


TABLE I -- Heat Transfer Results for Test Cases

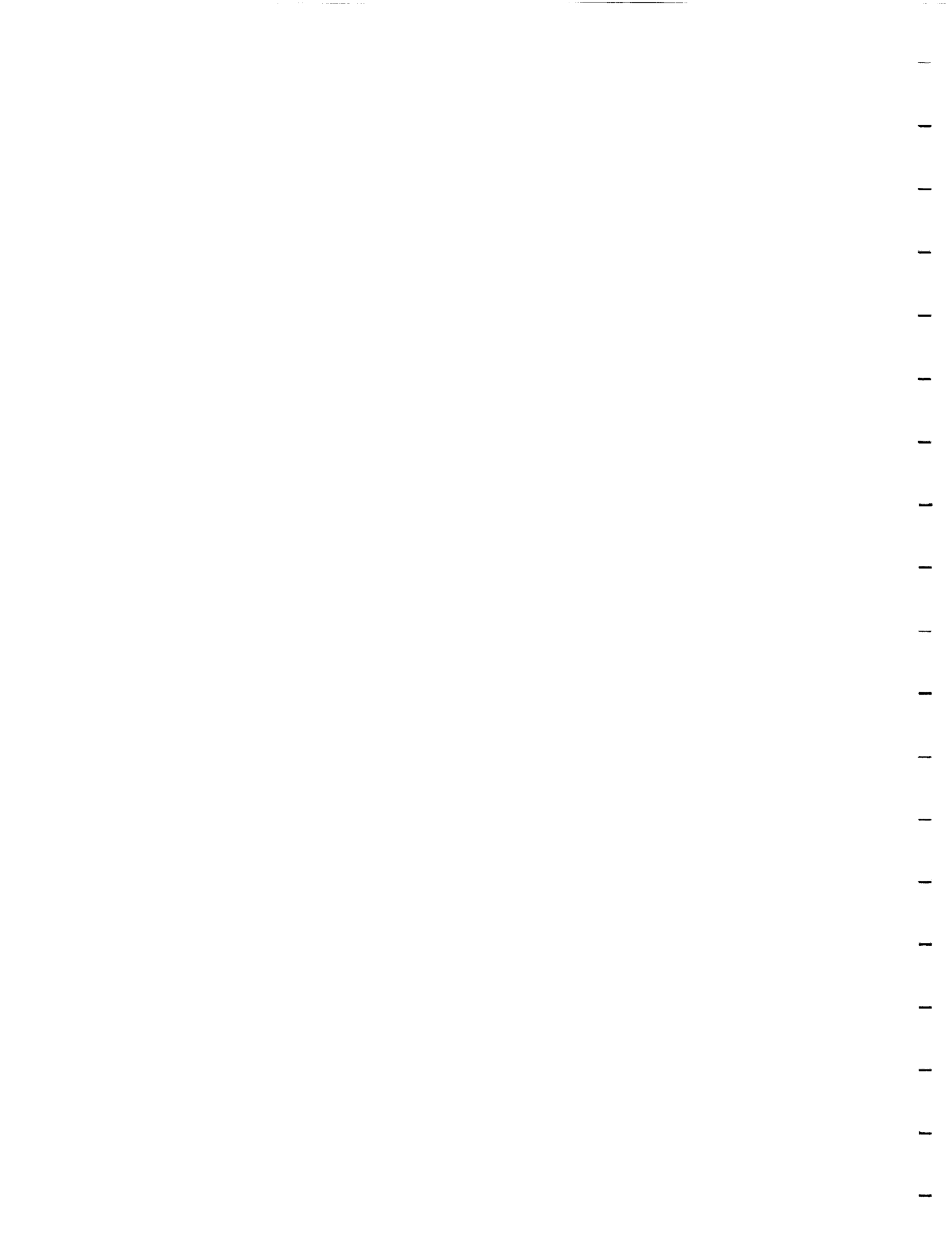
Case			Radiative Heat Transfer				Convective Heat Transfer	
U_{∞} (km/sec)	Altitude (km)	R_{nose} (m)	Uncoupled (watts/sq cm)	Coupled (watts/sq cm)		Comments	(watts/sq cm)	
			Atomic LTNE Corrections					
			No	Yes	No	Yes		
8.915	77.9	2.3	7.21	6.05	5.46	4.76	Molecules Incl.	10.1
9.326	75.15	2.3	9.52	7.12	7.76	6.08	Molecules Incl.	16.0
14.5	65	1.0		1691		1039	Atomic Rad. Only	195
12	80	2.3	388	10.9	94.1	9.44	Atomic Rad. Only	30.5
14	80	2.3	1636	67.3	279	49.7	Atomic Rad. Only	49.8
16	80	2.3	4060	173	548	124	Atomic Rad. Only	70.0
16	75	2.3	3949	669	921	430	Atomic Rad. Only	89.9
16	72	2.3		1384		758	Atomic Rad. Only	103
16	72	1.0		738		518	Atomic Rad. Only	184
14	66	1.0		1004		657	Atomic Rad. Only	167
14	66	2.3		1815		971	Atomic Rad. Only	97.2

Table II -- Wall Radiative Flux Above 2000 Angstroms

T_e (K)	Thickness (cm)	Pressure (atm)	Radical	Neqair	8-Step
(watts/ sq cm in all cases)					
12991	3.6	.3268	470	433	490
10844	12	.0264	18	17	19

Table III -- Inviscid Equilibrium Results from Sutton

Case U_{∞} (km/sec)	Altitude (km)	Nose Radius (m)	Radiative Heat Transfer (watts/sq cm)		Standoff Distance (cm)
			Adiabatic	Coupled	
16	72	2.3	2668	1066	7.75
16	72	1.0	1570	845	3.6
14	66	2.3	3208	1323	8.65
14	66	1.0	2054	1065	3.92



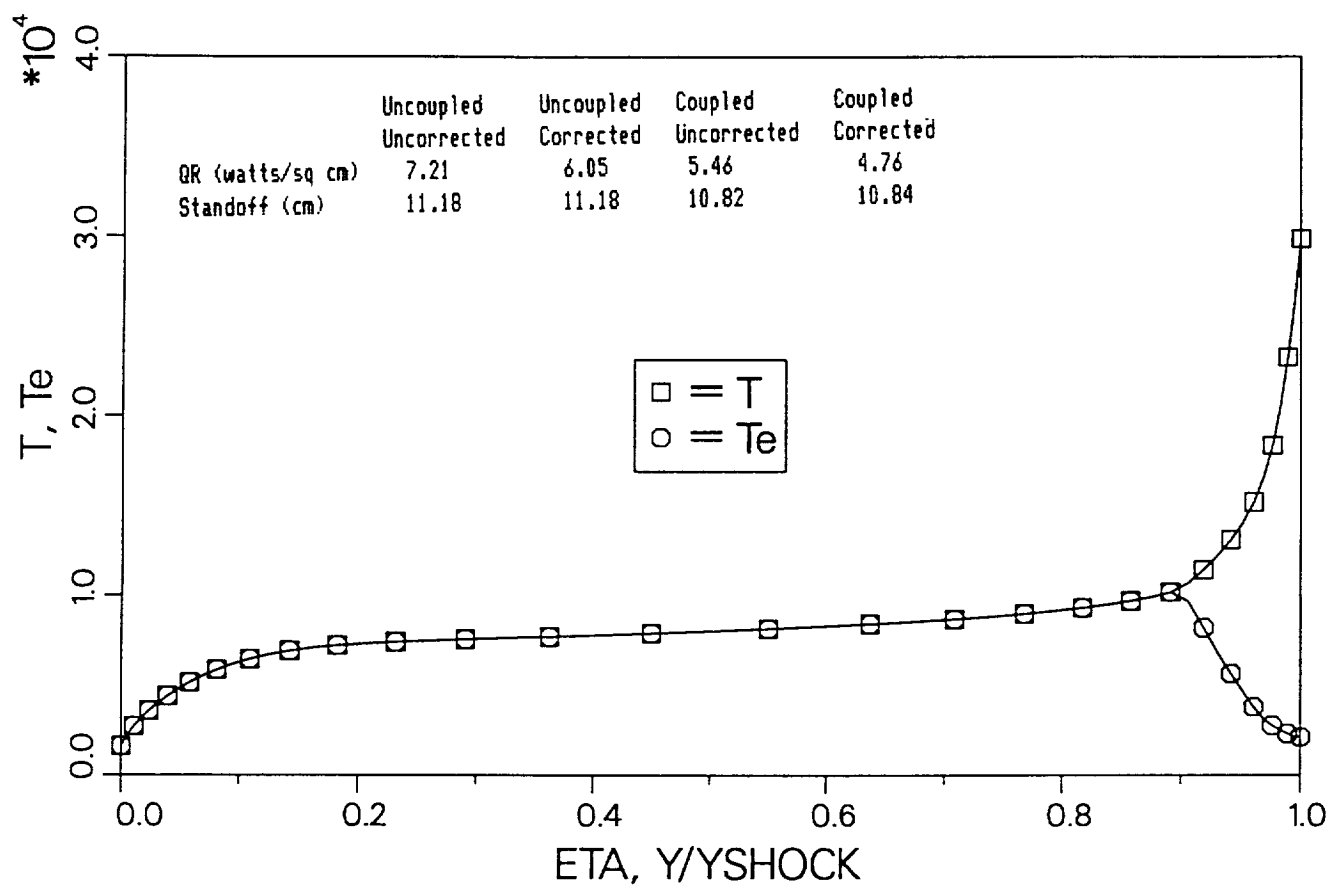
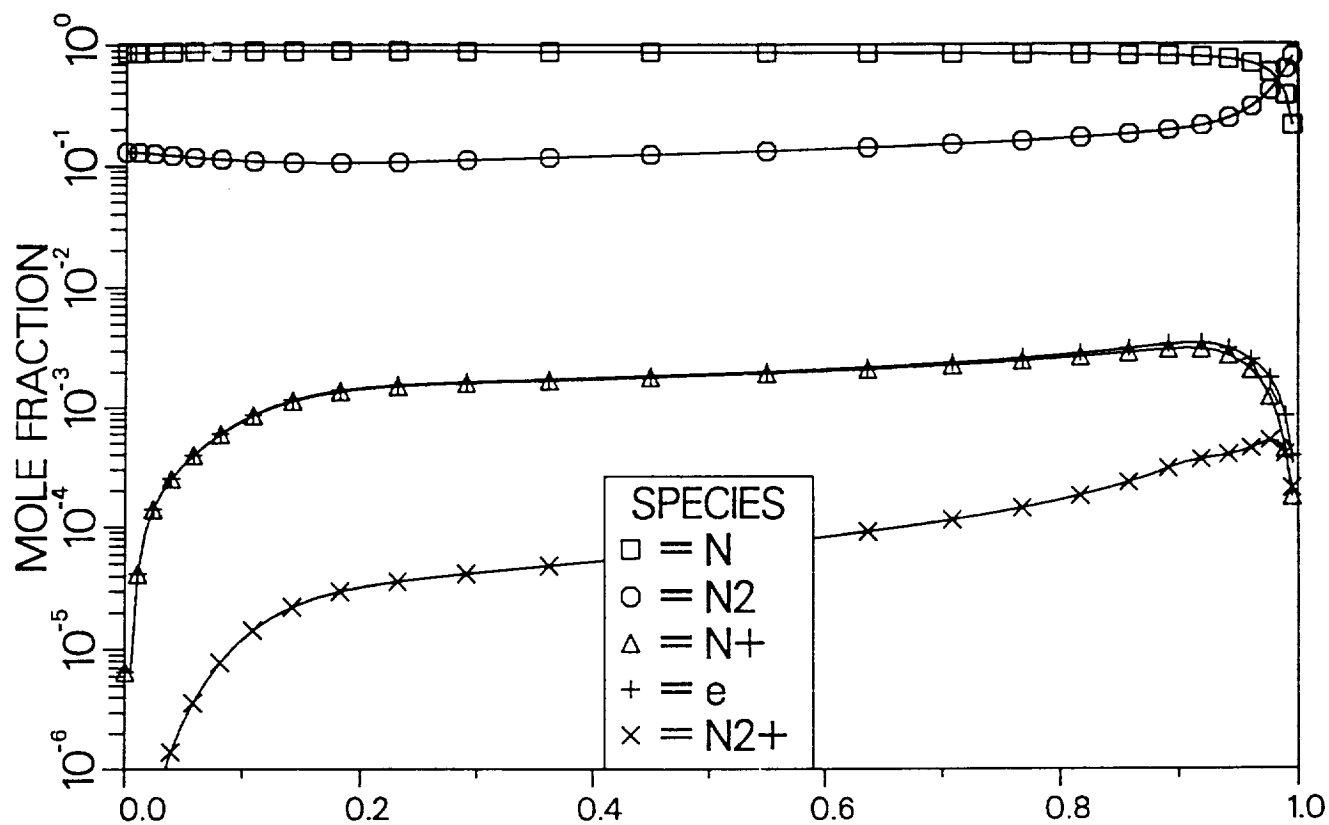


Fig. 1 -- Stagnation Profiles with Radiation Coupling and LTNE Effects

$U = 8.915$ km/sec, $H = 77.9$ km, $R_{nose} = 2.3$ m

QR = 4.76 watts/sq cm, $\delta = 10.84$ cm



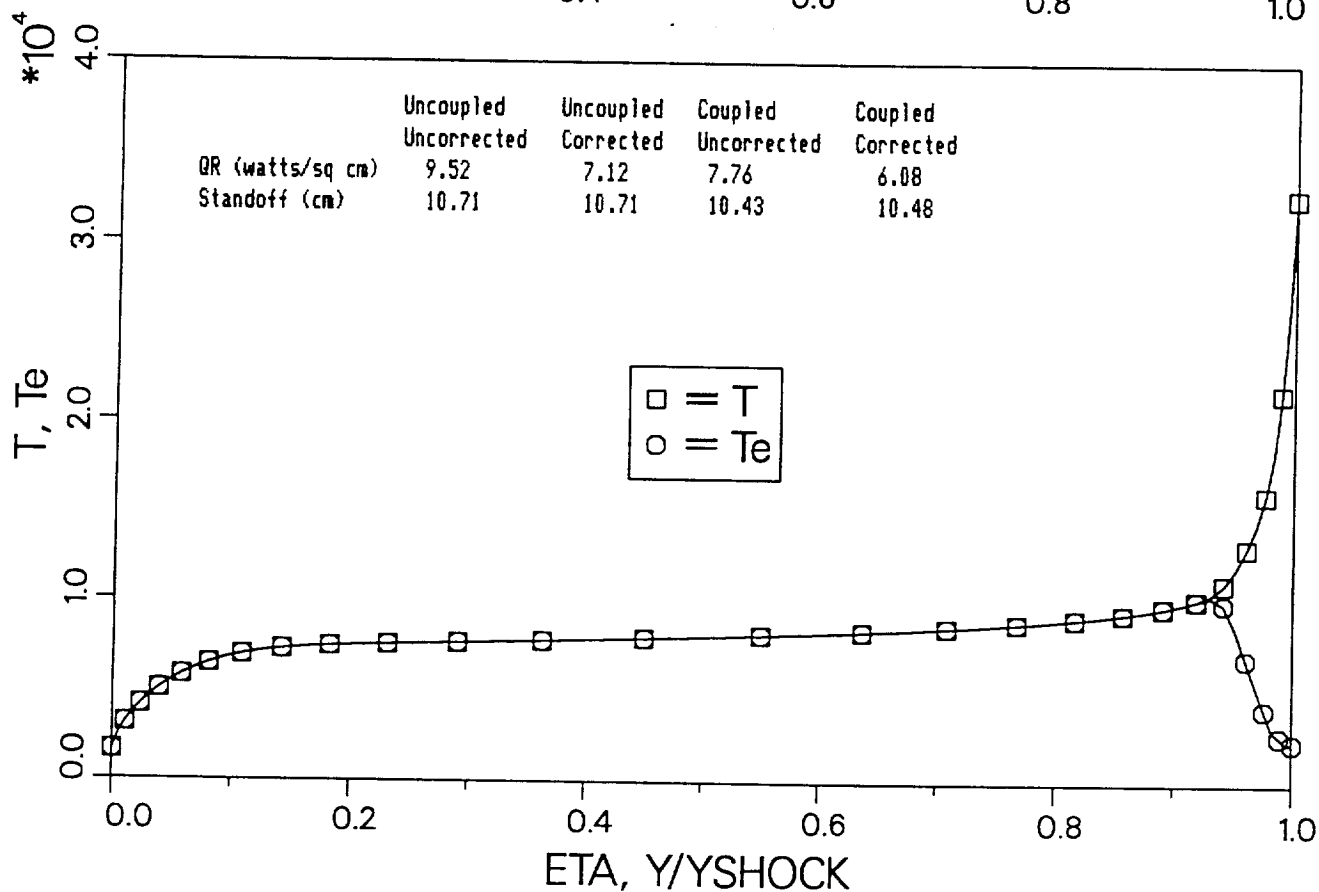
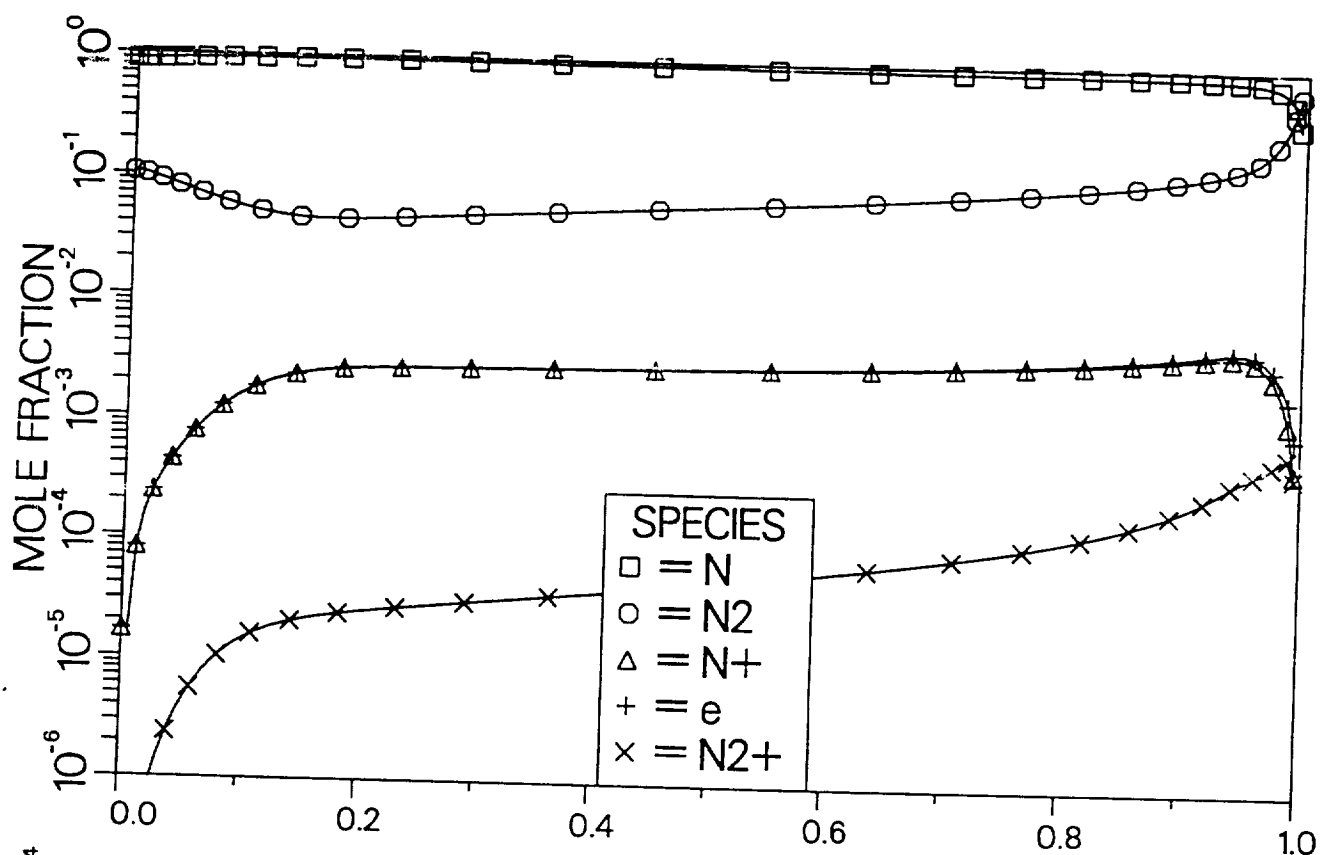


Fig. 2 -- Stagnation Profiles with Radiation Coupling and LTNE Effects
 $U = 9.326$ km/sec, $H = 75.2$ km, $R_{nose} = 2.3$ m
 $QR = 6.08$ watts/sq cm $\delta = 10.48$ cm



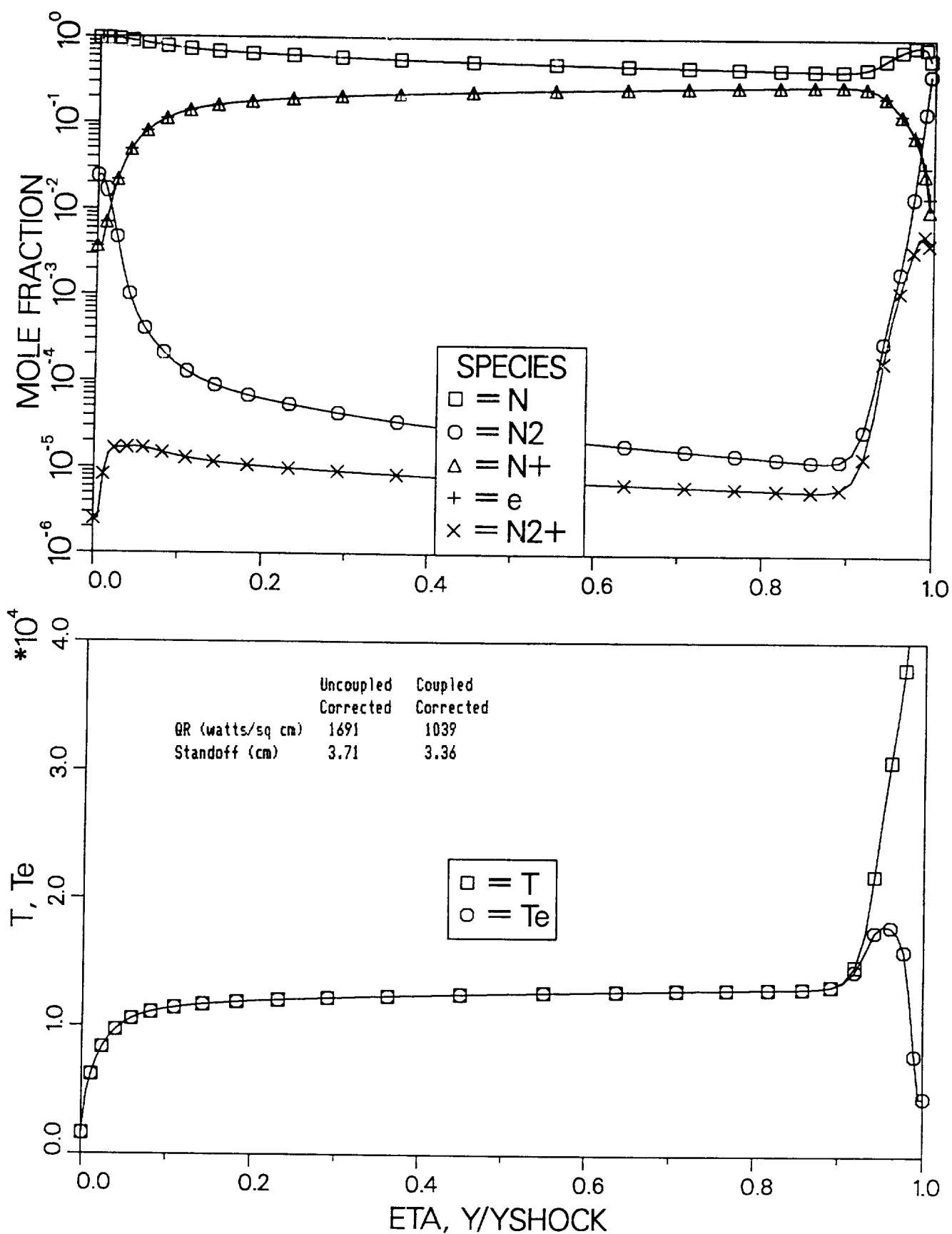


Fig. 3 -- Stagnation Profiles with Radiation Coupling and LTNE Effects

$U = 14.5$ km/sec, $H = 65$ km, $R_{nose} = 1$ m

QR = 1039 watts/sq cm $\delta = 3.36$ cm



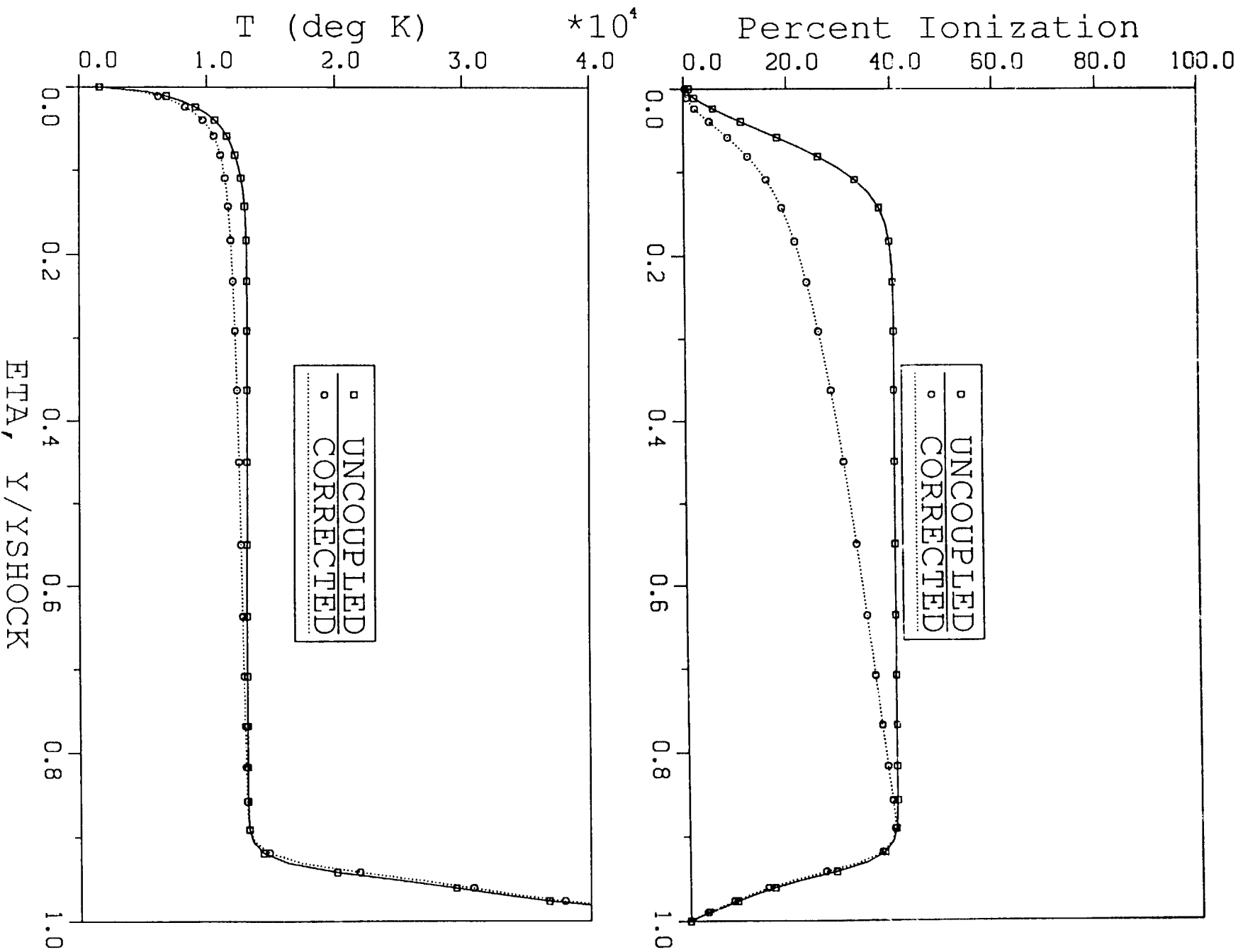


Fig. 4 --- Comparison of Uncoupled and Coupled Profiles. Both with LTNE Effects
 $U = 14.5 \text{ km/sec}$, $H = 65 \text{ km}$, $R_{nose} = 1 \text{ m}$



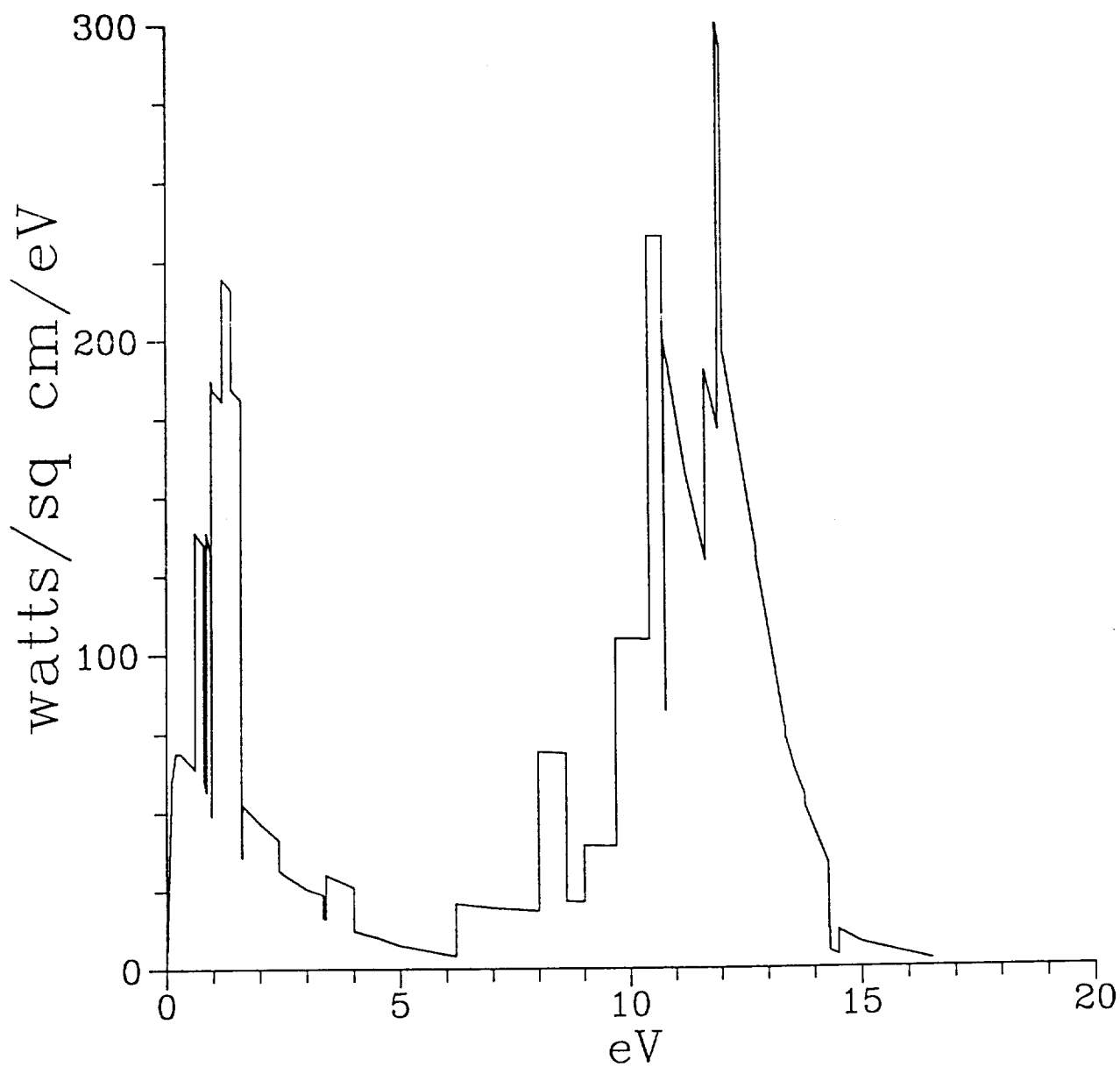


Fig. 5 -- Usual Presentation of Spectral Variation of Stagnation Point Heat Transfer
 $U = 14.5$ km/sec, $H = 65$ km, $R_{nose} = 1$ m



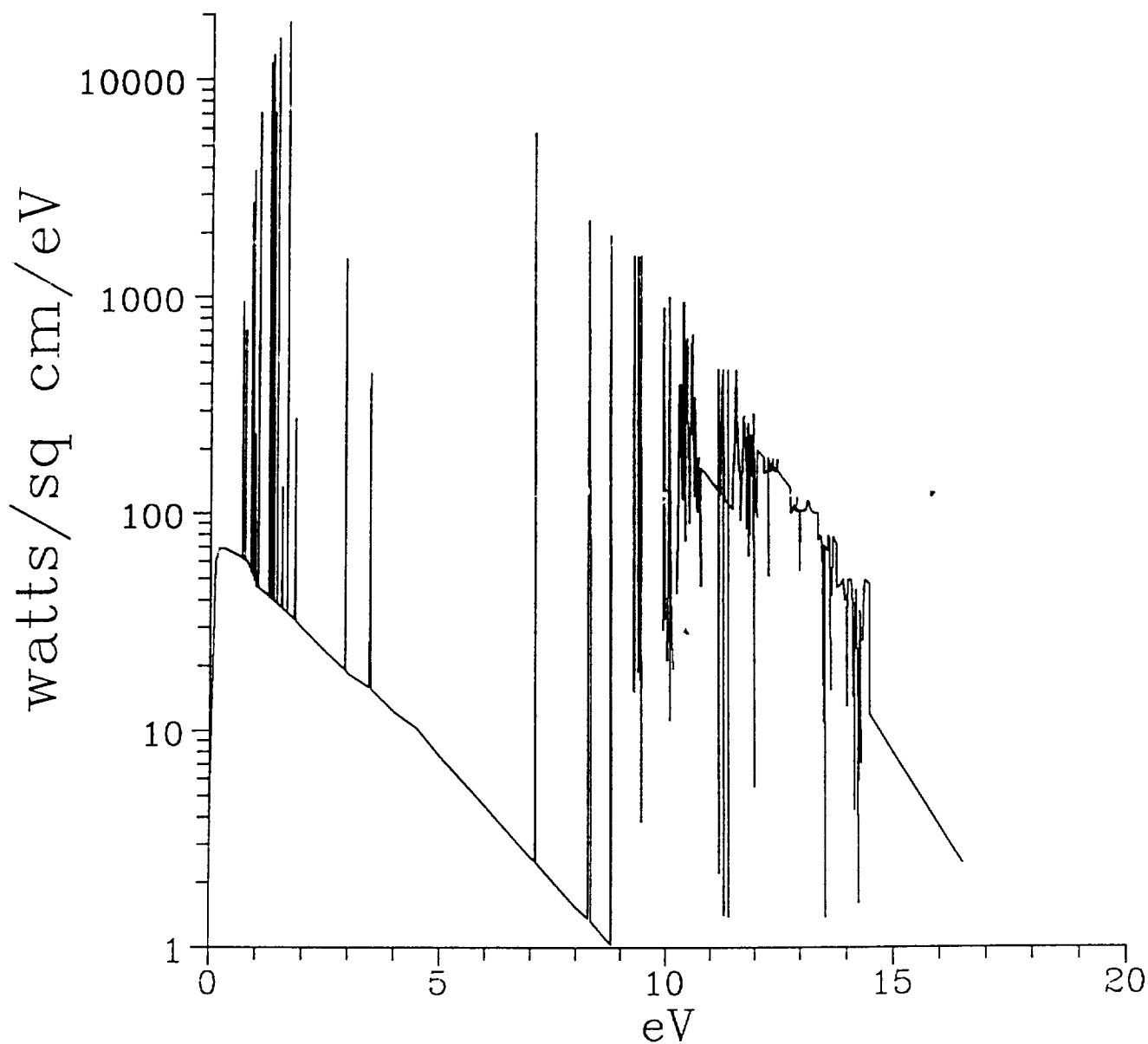


Fig. 6 -- Detailed Spectral Variation of Stagnation Point Heat Transfer
 $U = 14.5$ km/sec, $H = 65$ km, $R_{\text{nose}} = 1$ m



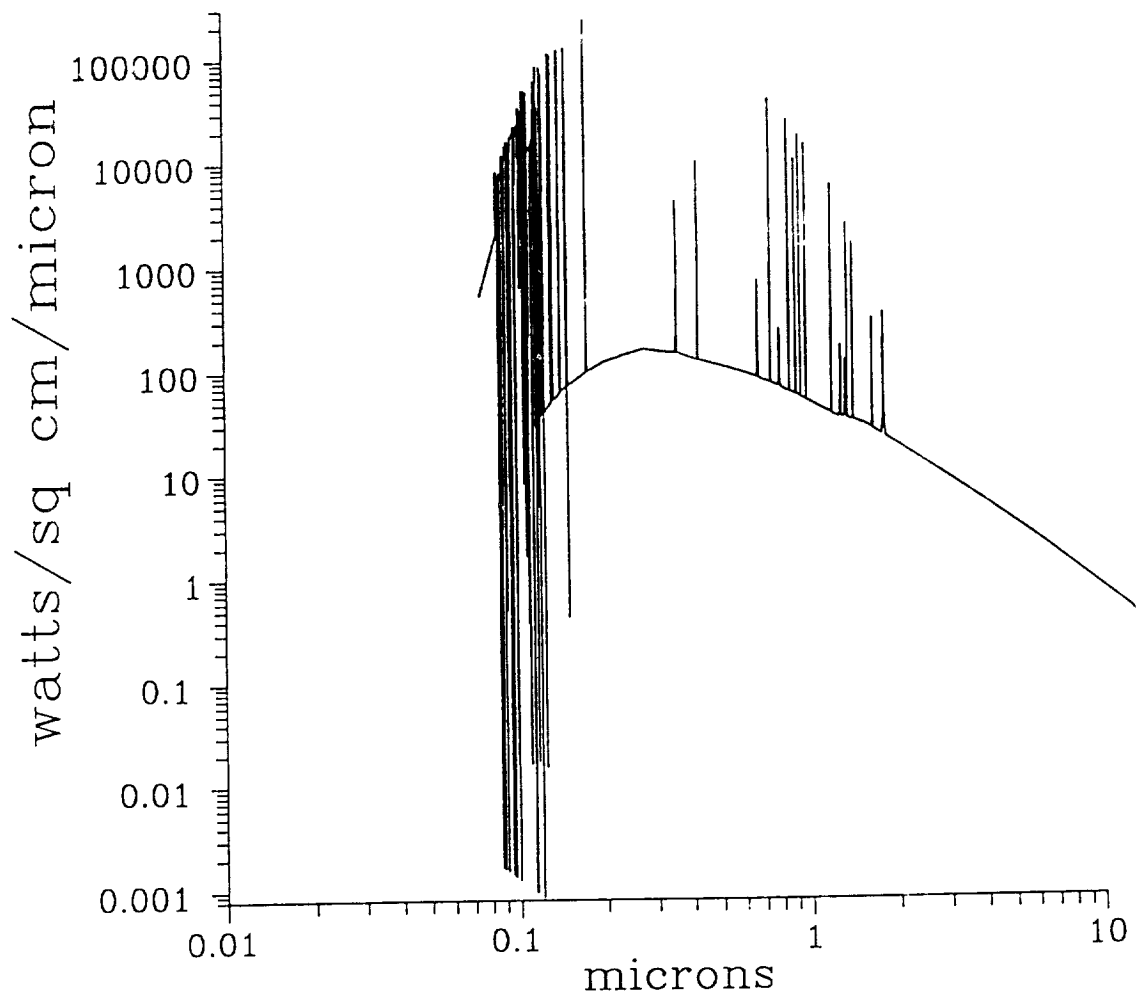


Fig. 7 -- Detail Spectral Variation of Stagnation Point Heat Transfer
 $U = 14.5$ km/sec, $H = 65$ km, $R_{nose} = 1$ m



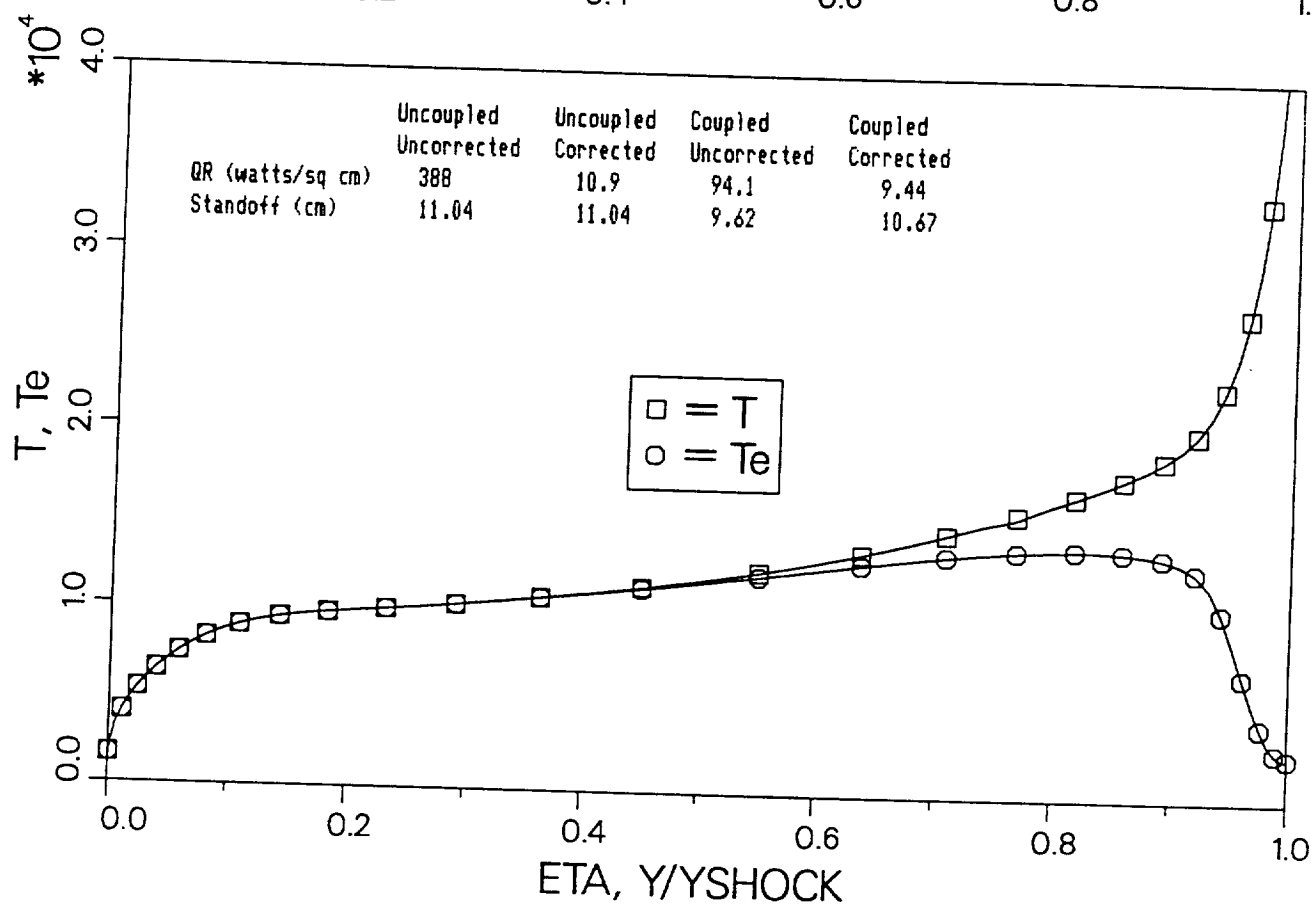
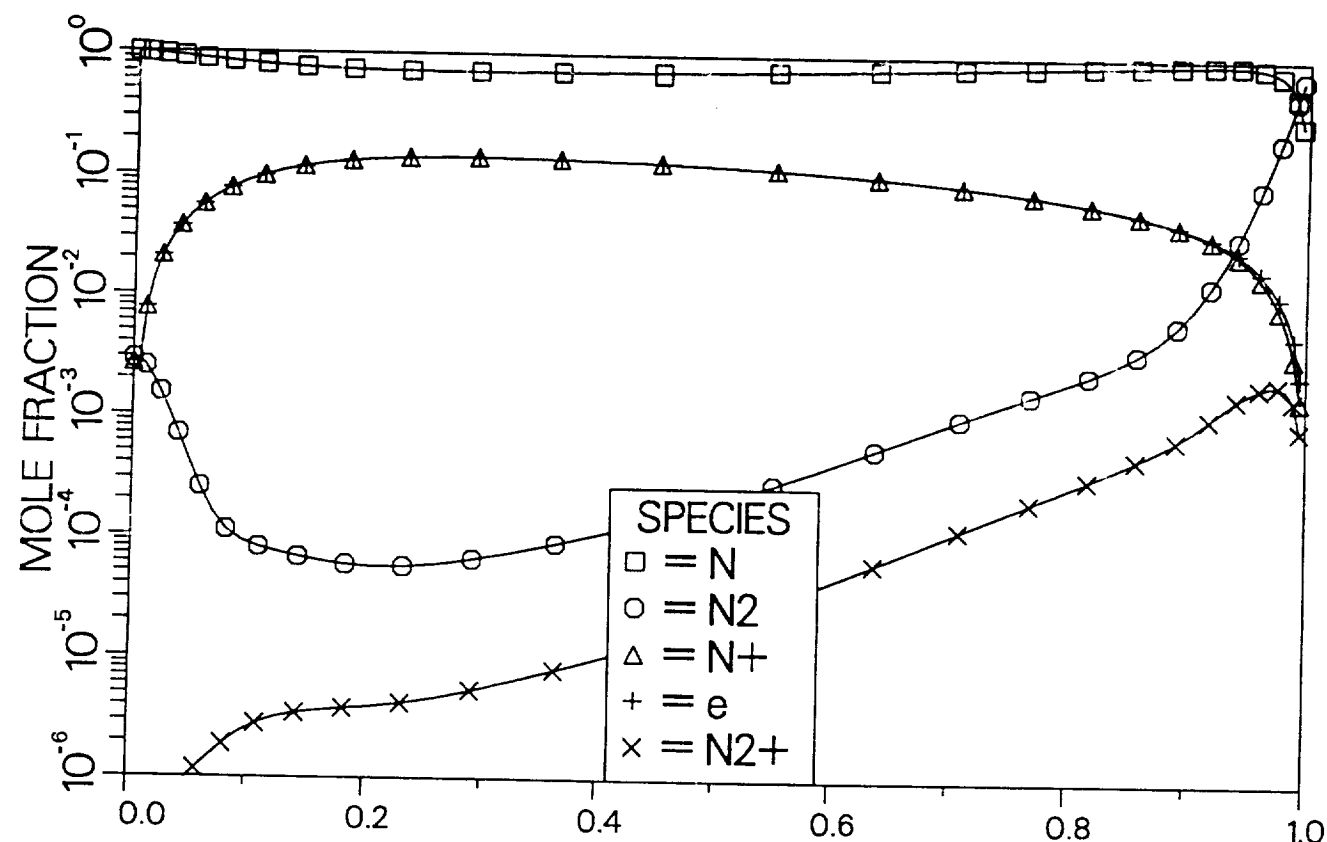


Fig. 8 -- Stagnation Profiles with Radiation Coupling and LTNE Effects
 $U = 12$ km/sec, $H = 80$ km, $R_{nose} = 2.3$ m
 $QR = 9.44$ watts/sq cm $\delta = 10.67$ cm



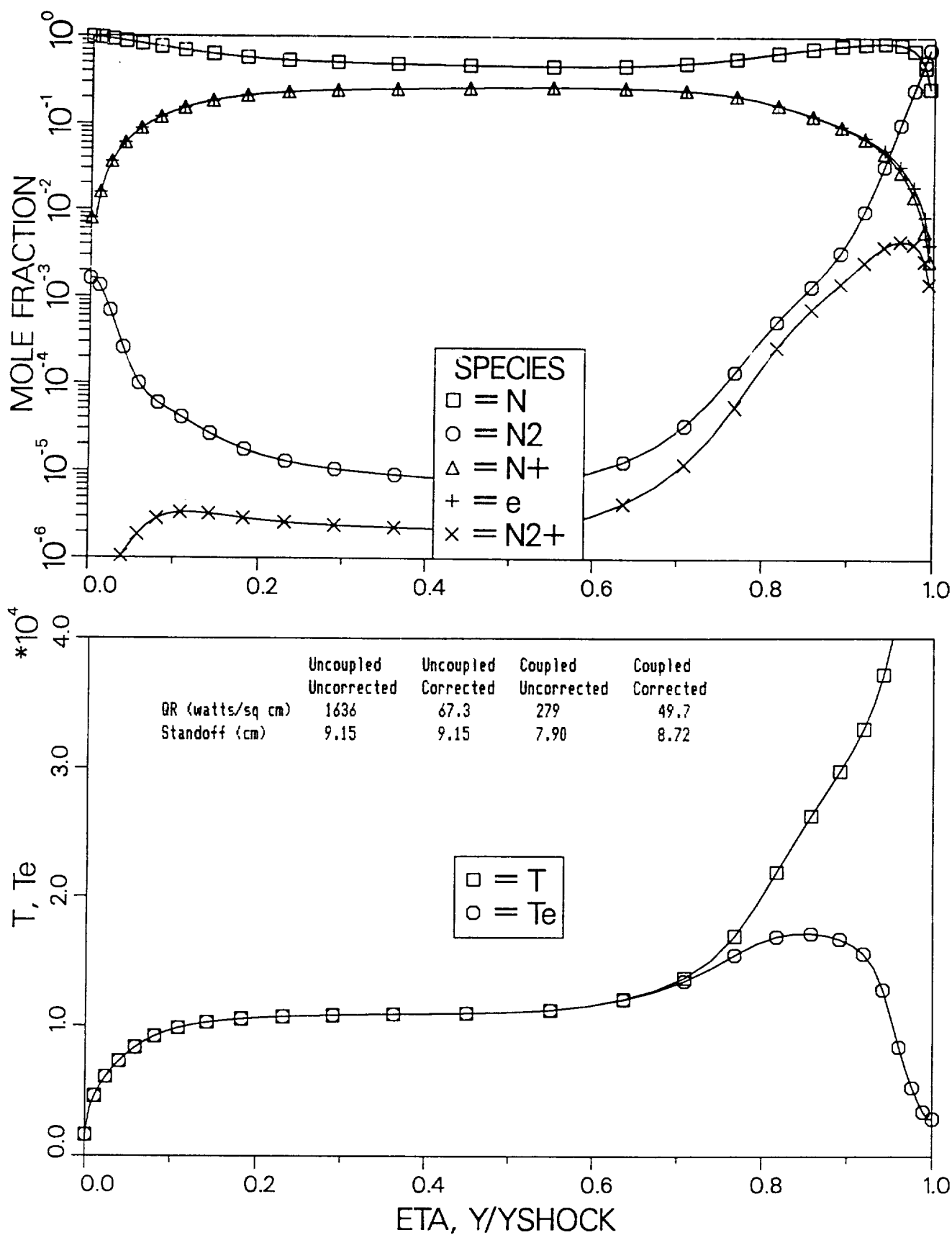


Fig. 9 -- Stagnation Profiles with Radiation Coupling and LTNE Effects
 $U = 14 \text{ km/sec}$, $H = 80 \text{ km}$, $R_{\text{nose}} = 2.3 \text{ m}$
 $QR = 49.7 \text{ watts/sq cm}$ $\delta = 8.72 \text{ cm}$



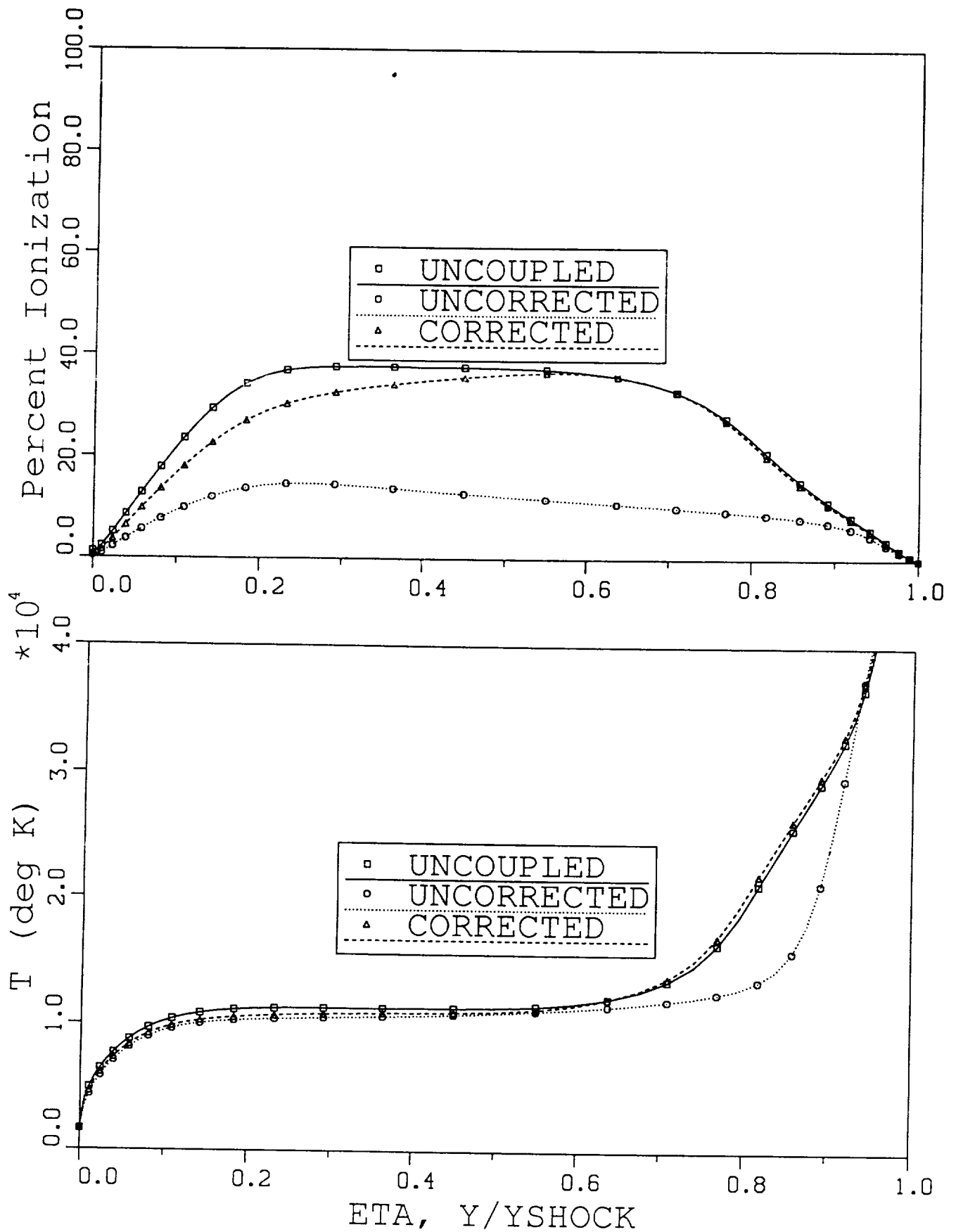


Fig. 10 -- Comparison of Uncoupled, Coupled Uncorrected, and Coupled Corrected Profiles
 9a $U = 14 \text{ km/sec}, H = 80 \text{ km}, R_{\text{nose}} = 2.3 \text{ m}$



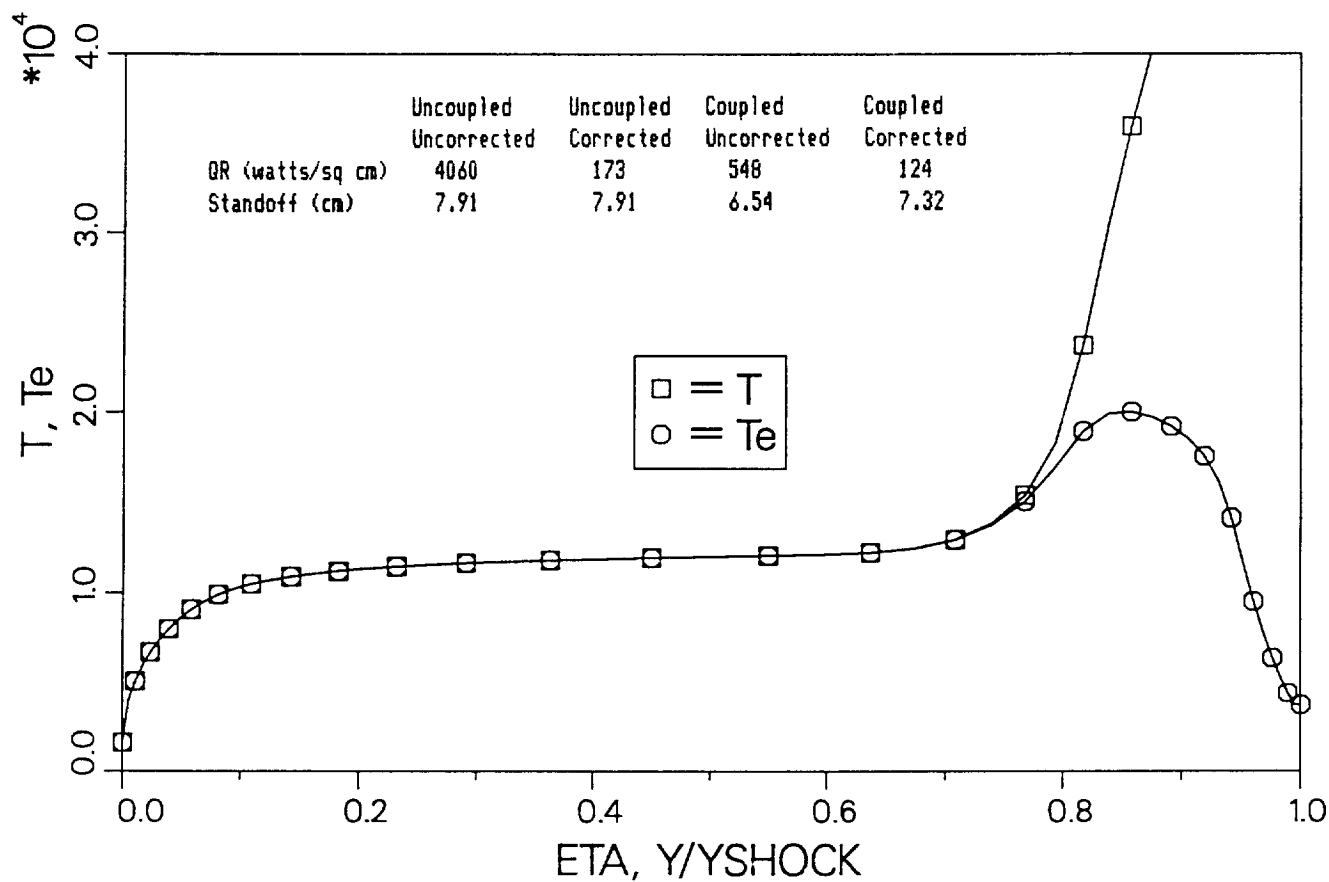
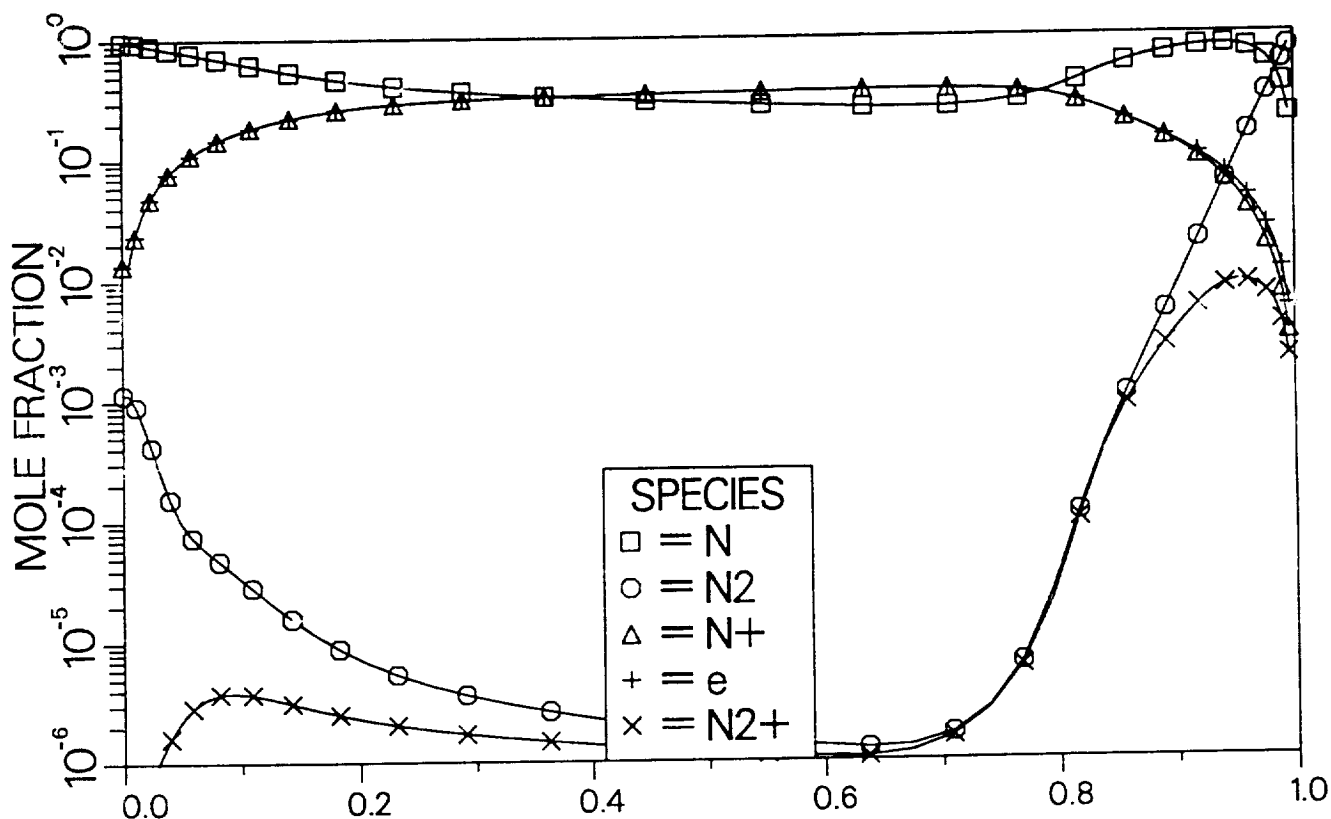


Fig. 10 -- Stagnation Profiles with Radiation Coupling and LTNE Effects
 $U = 16$ km/sec, $H = 80$ km, $R_{nose} = 2.3$ m
 $QR = 124$ watts/sq cm $\delta = 7.32$ cm



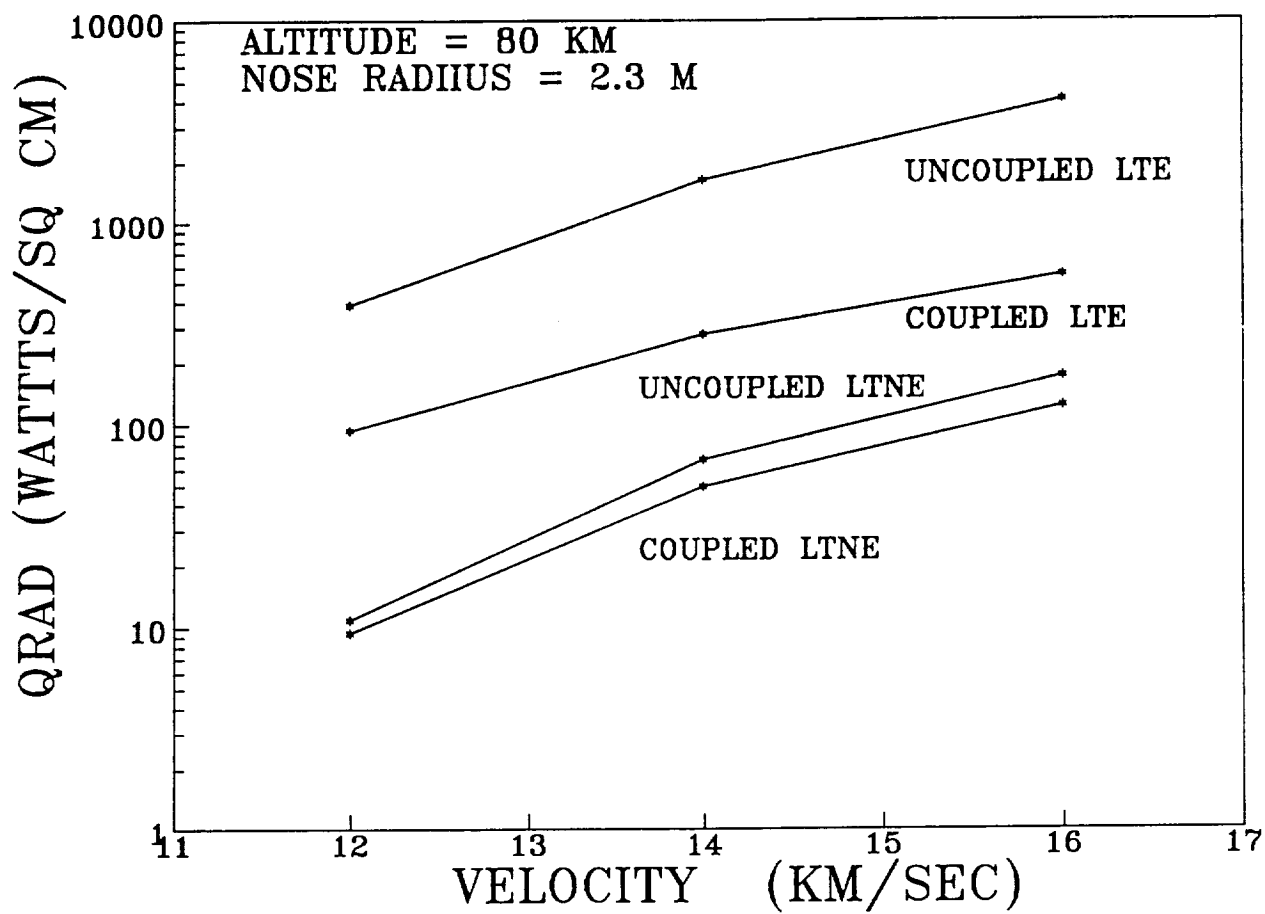


Figure 10a



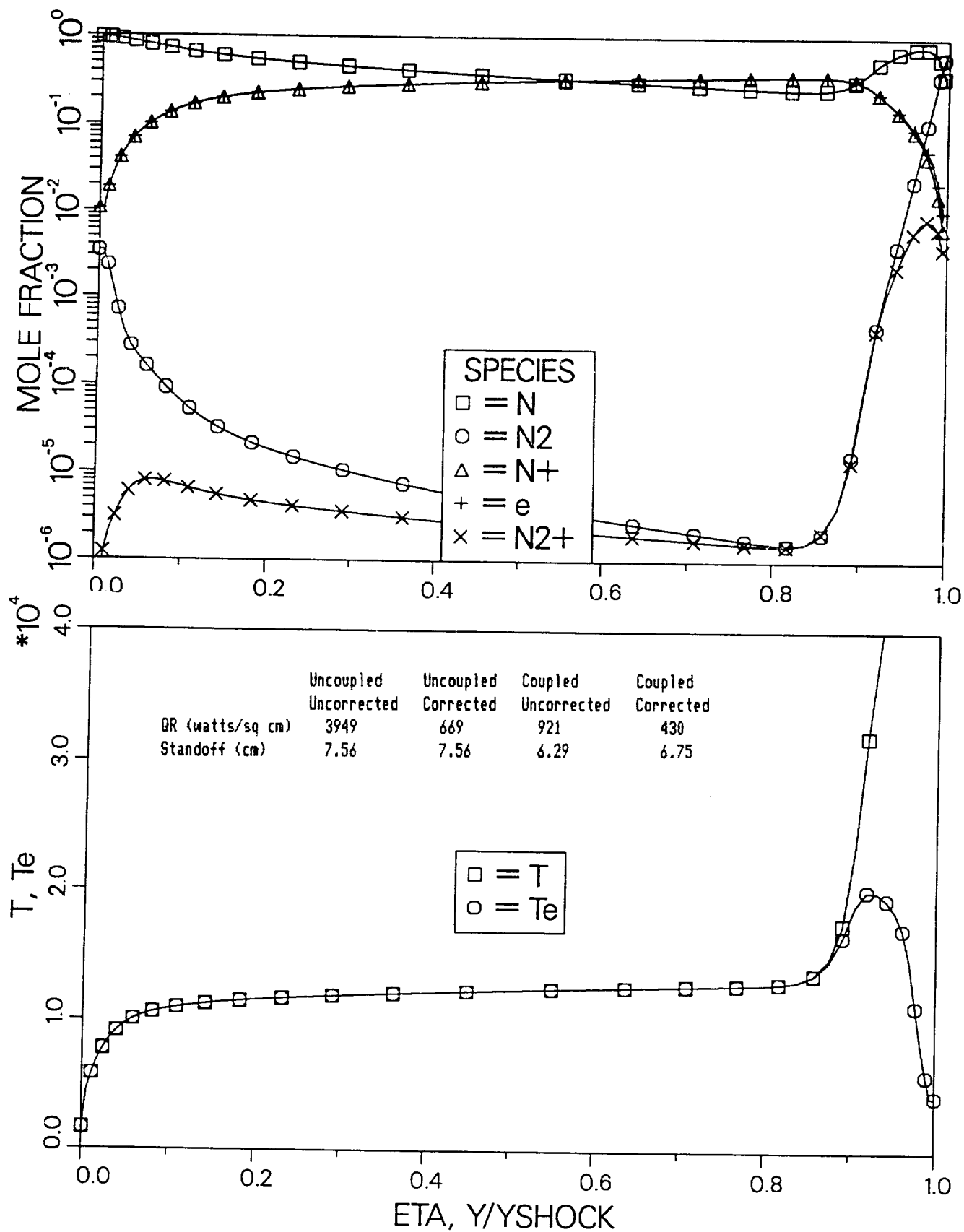


Fig. 11 -- Stagnation Profiles with Radiation Coupling and LTNE Effects
 $U = 16$ km/sec, $H = 75$ km, $R_{nose} = 2.3$ m
 $QR = 430$ watts/sq cm $\delta = 6.75$ cm

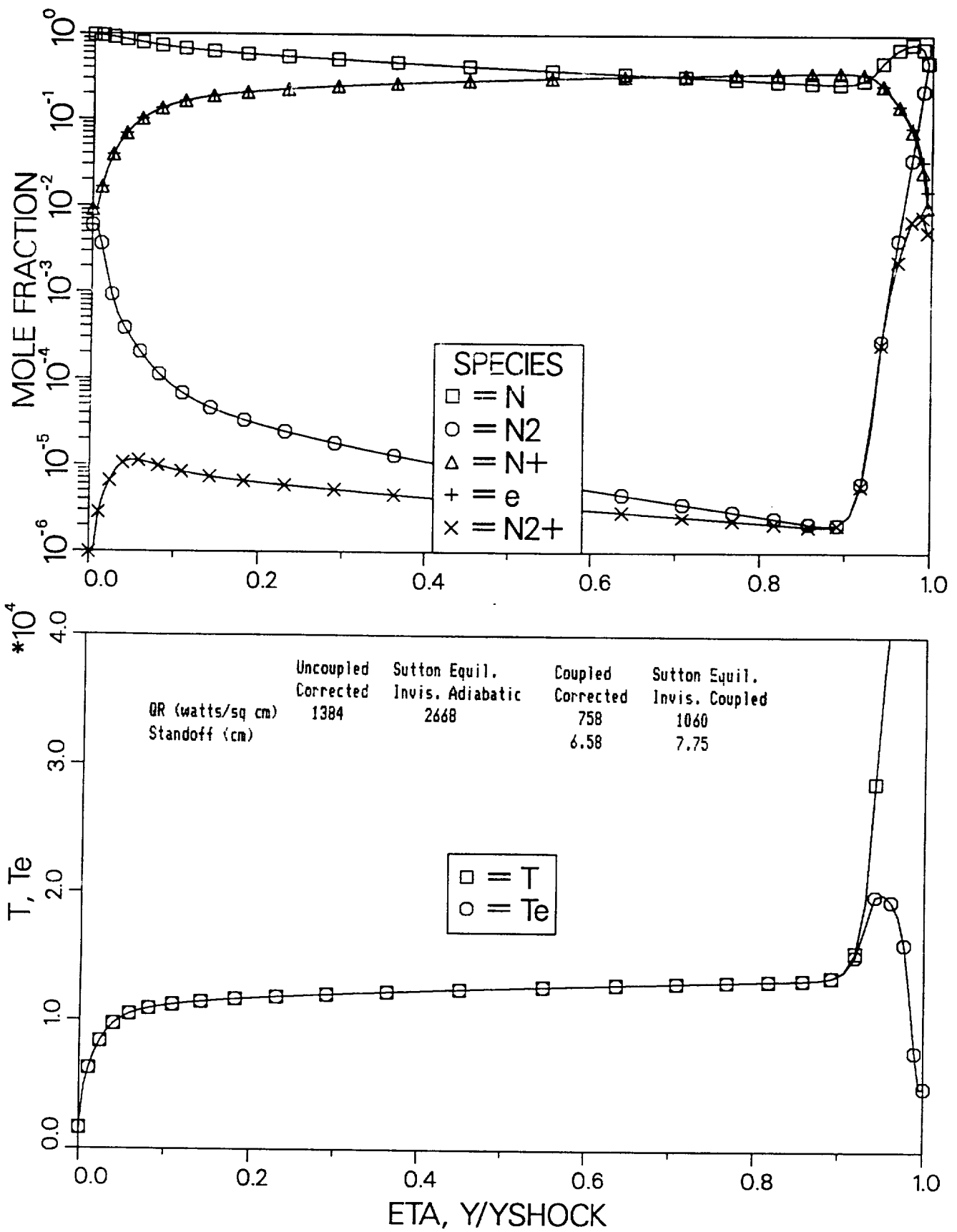
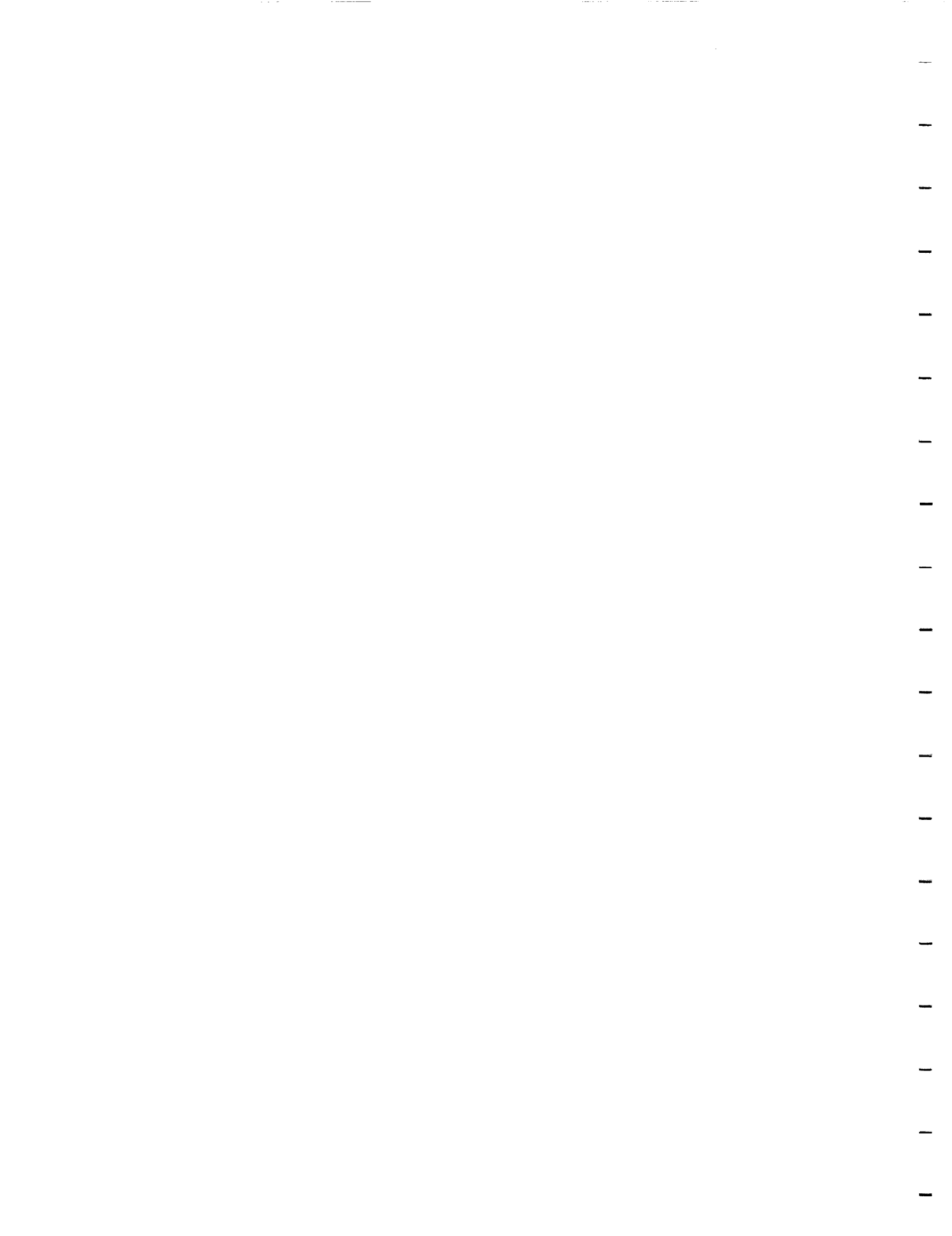


Fig. 12 -- Stagnation Profiles with Radiation Coupling and LTNE Effects
 $U = 16$ km/sec, $H = 72$ km, $R_{nose} = 2.3$ m
 $QR = 758$ watts/sq cm $\delta = 6.58$ cm



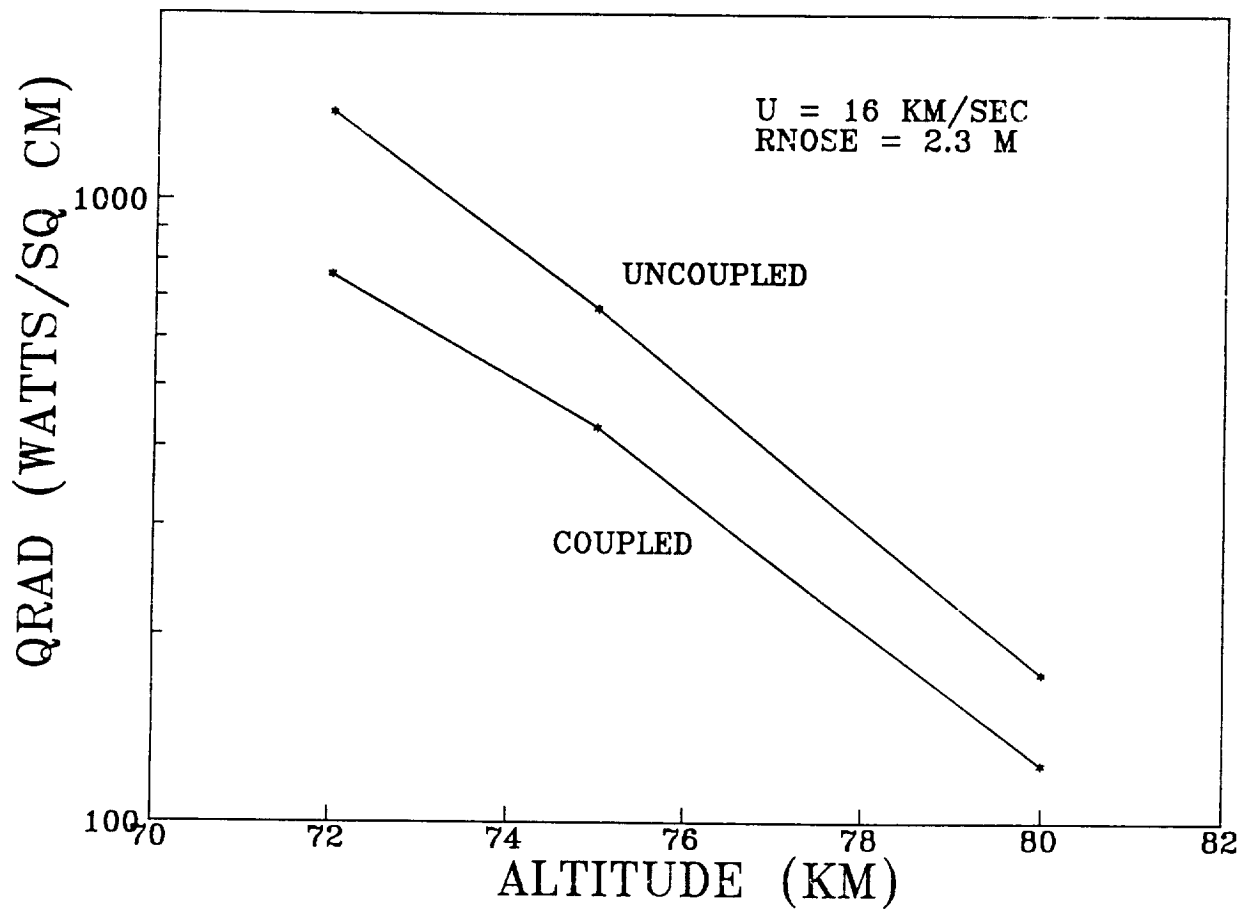
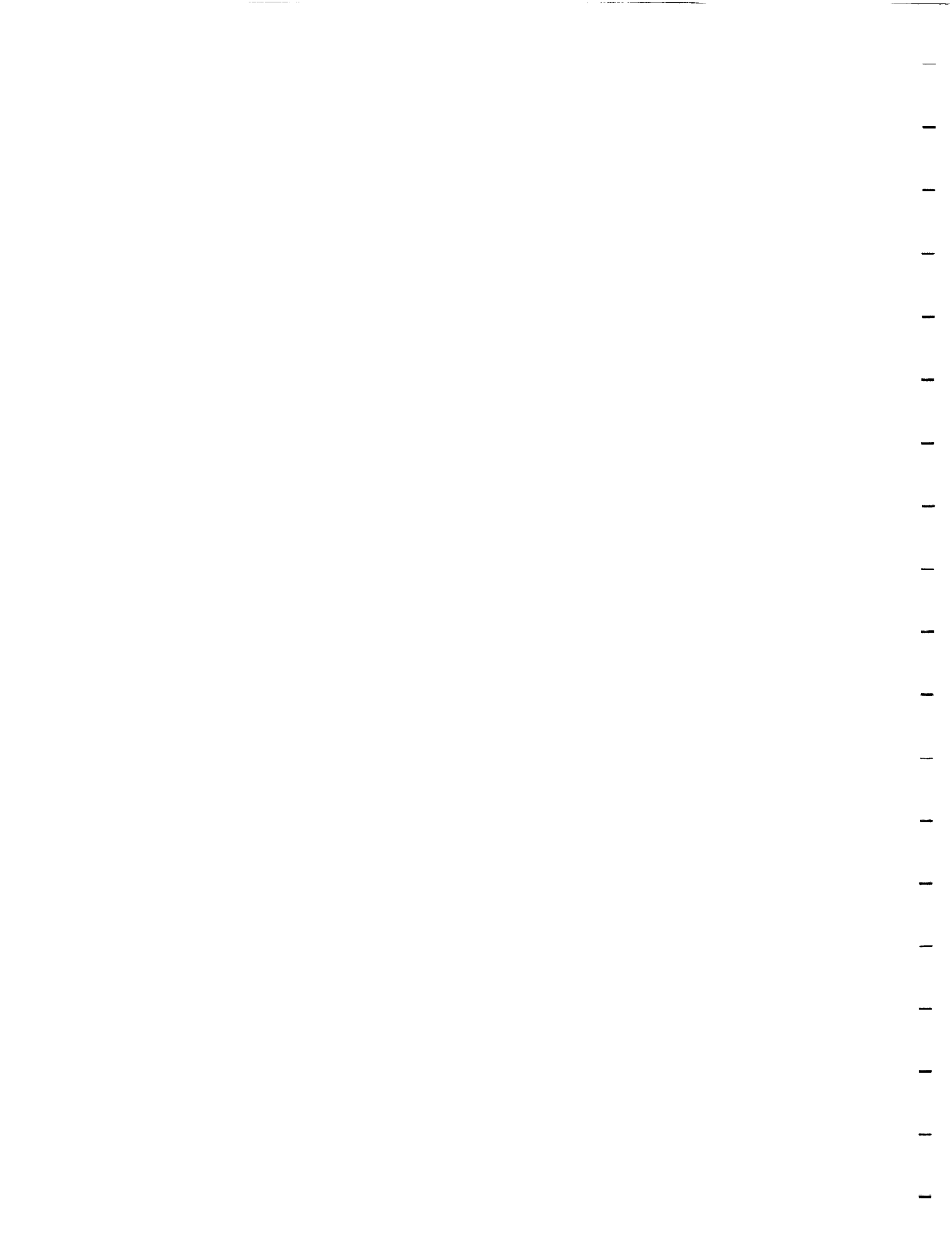


Figure 12(a)



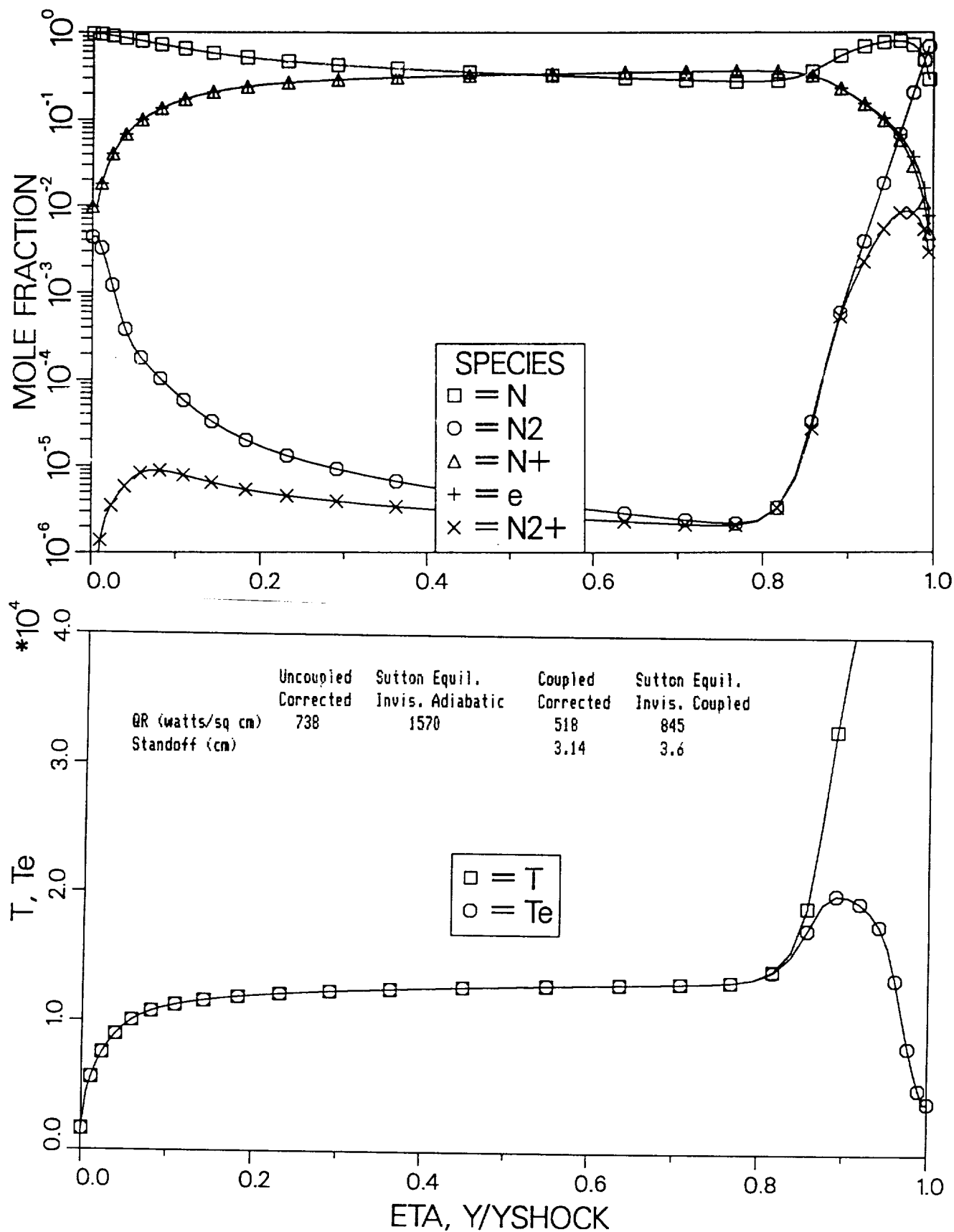


Fig. 13 -- Stagnation Profiles with Radiation Coupling and LTNE Effects
 $U = 16$ km/sec, $H = 72$ km, $R_{nose} = 1$ m
 $QR = 518$ watts/sq cm $\delta = 3.14$ cm



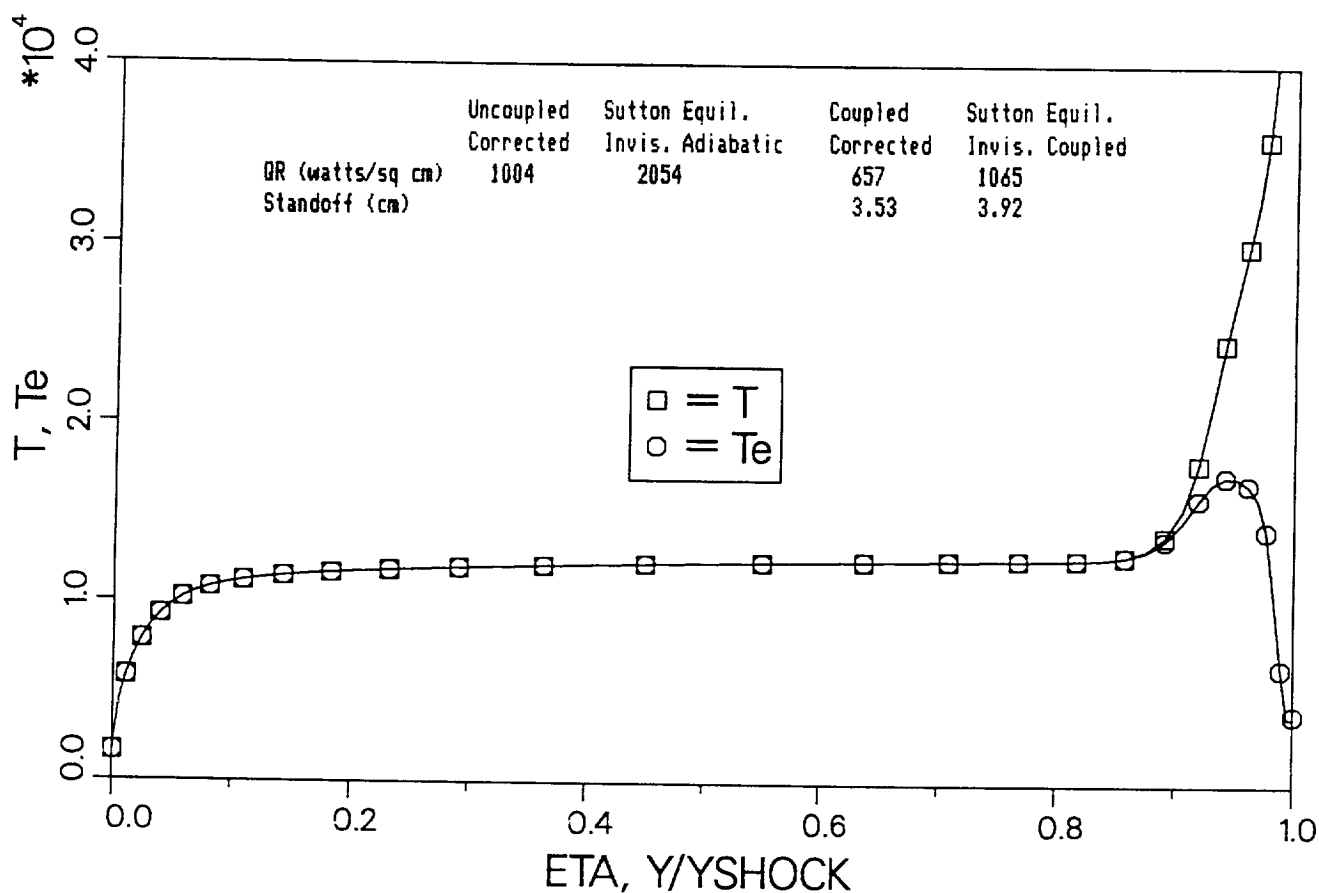
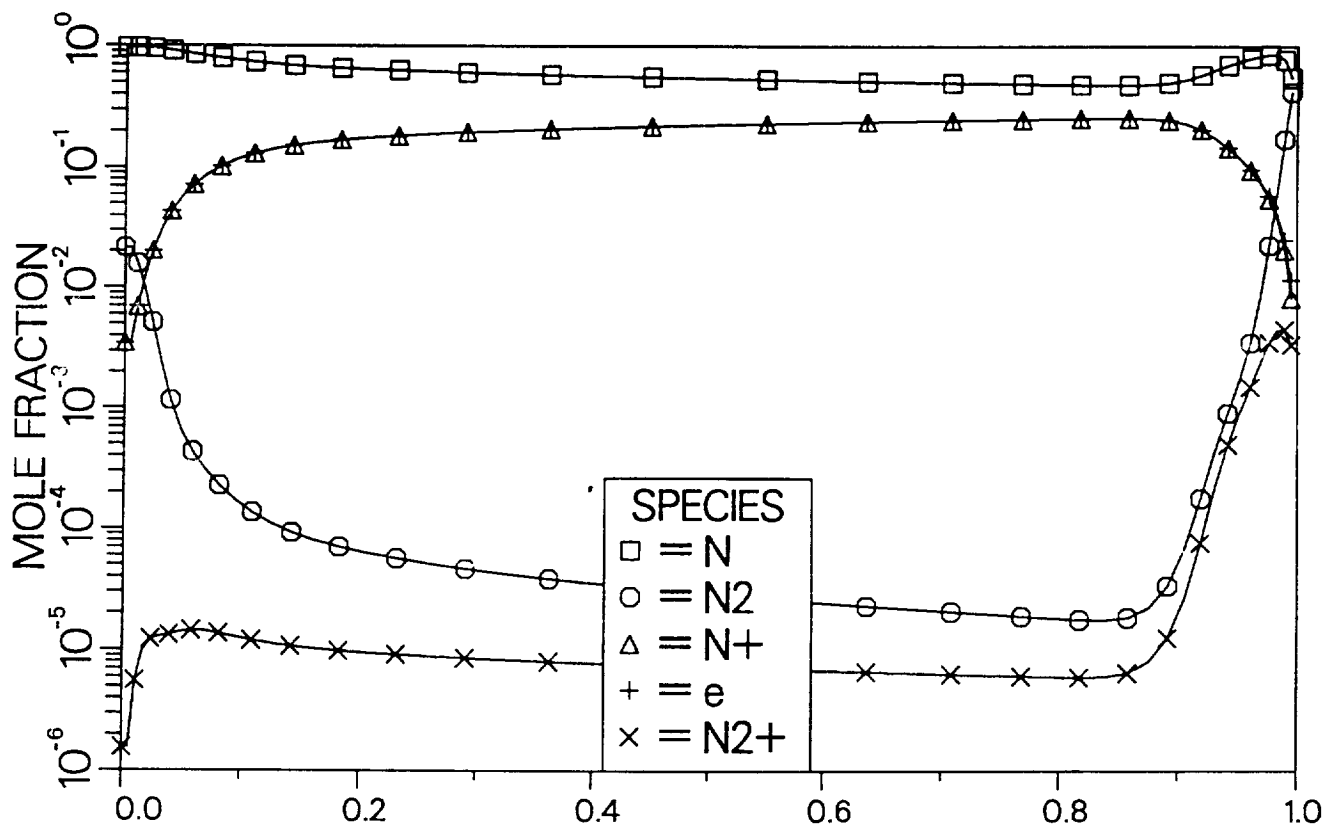


Fig. 14 -- Stagnation Profiles with Radiation Coupling and LTNE Effects
 $U = 14$ km/sec, $H = 66$ km, $R_{nose} = 1$ m
 $QR = 657$ watts/sq cm $\delta = 3.53$ cm

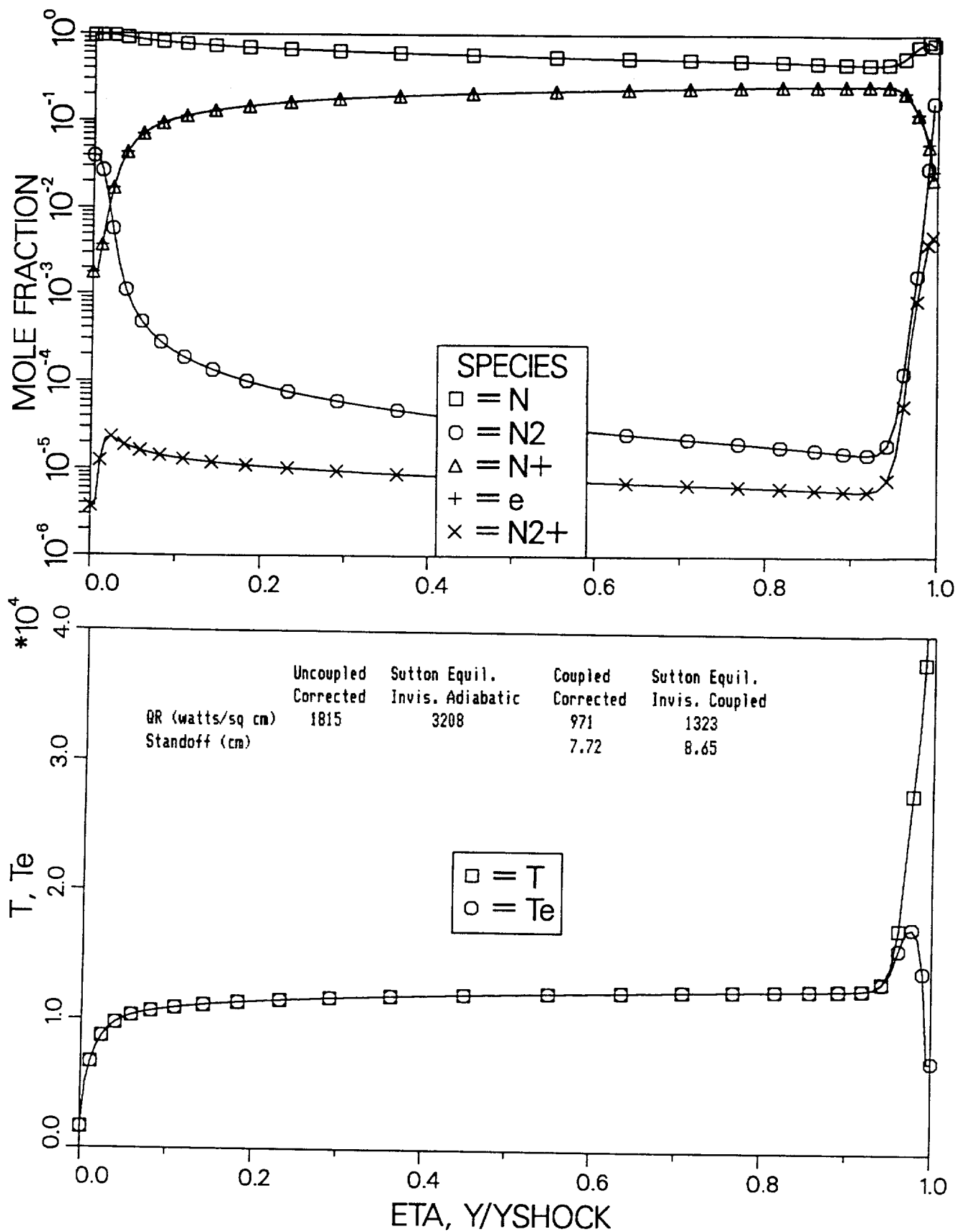


Fig. 15 -- Stagnation Profiles with Radiation Coupling and LTNE Effects

$U = 14$ km/sec, $H = 66$ km, $R_{nose} = 2.3$ m

QR = 971 watts/sq cm $\delta^* = 7.72$ cm



D

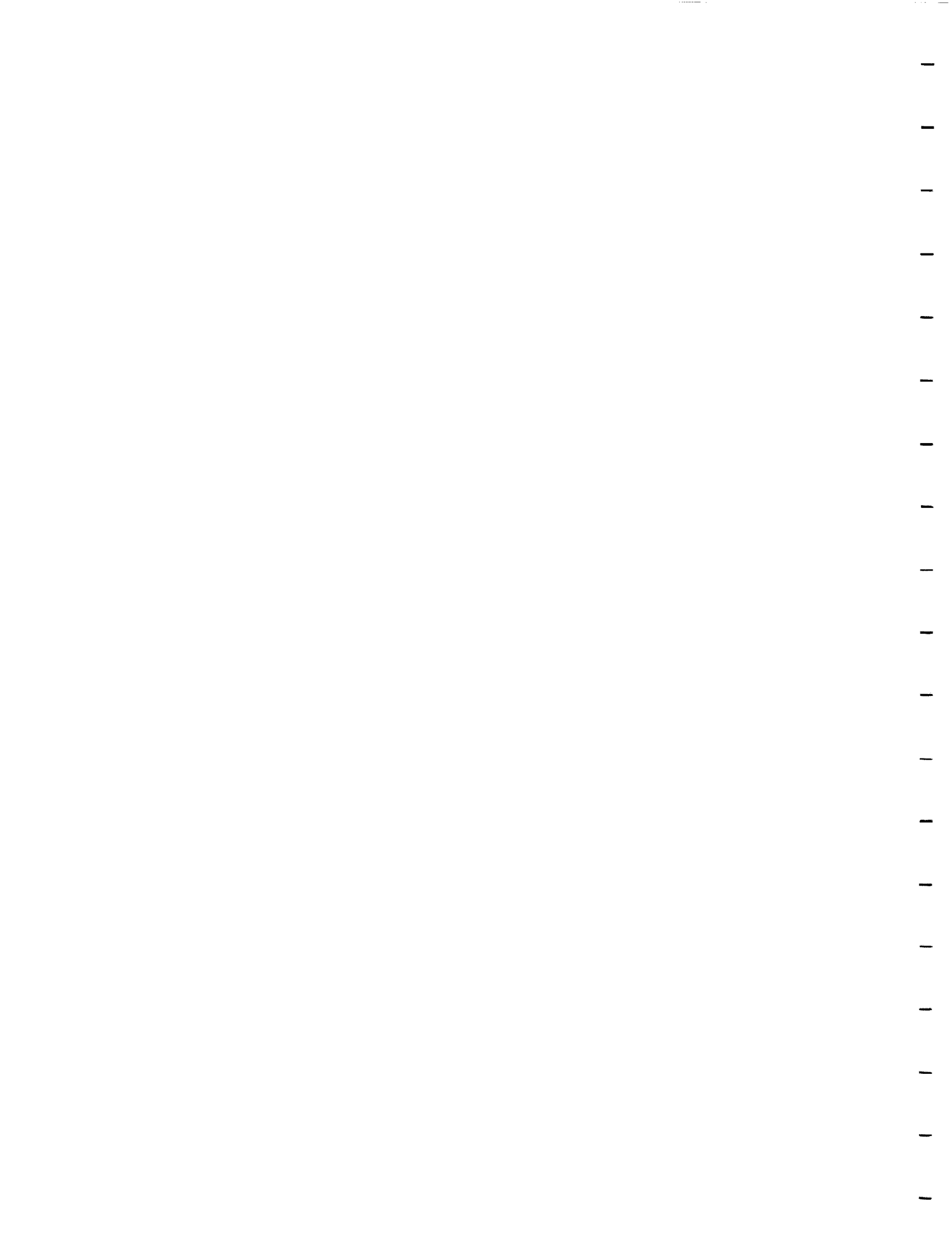
pres

APPENDIX II

Derivation of the Species Conservation Equations for Momentum and Energy

Howe

nota



APPENDIX II

DERIVATION OF THE SPECIES CONSERVATION EQUATIONS FOR MOMENTUM AND ENERGY

In Chapter II the general equation of change was presented as

$$\begin{aligned} \frac{\partial}{\partial t} (N_i \overline{\phi_i}) + \sum_{j=1}^3 \frac{\partial}{\partial x_j} (N_i \overline{\phi_i u_j}) - N_i \left\{ \frac{\partial \overline{\phi_i}}{\partial t} \right. \\ \left. + \sum_{j=1}^3 u_j \frac{\partial \overline{\phi_i}}{\partial x_j} + \sum_{j=1}^3 F_j \frac{\partial \overline{\phi_i}}{\partial u_j} \right\} = N_i \Delta \overline{\phi_i} \end{aligned} \quad (\text{I-1})$$

However the summation terms can be expressed in vector notation as

$$\begin{aligned} \sum_{j=1}^3 \frac{\partial}{\partial x_j} (N_i \overline{\phi_i u_j}) &= \frac{\partial}{\partial x_1} (N_i \overline{\phi_i u_1}) + \frac{\partial}{\partial x_2} (N_i \overline{\phi_i u_2}) \\ &+ \frac{\partial}{\partial x_3} (N_i \overline{\phi_i u_3}) = \frac{\partial}{\partial \vec{r}} \cdot (N_i \overline{\vec{v}_i \phi_i}) \end{aligned} \quad (\text{I-2})$$

$$\sum_{j=1}^3 F_j \frac{\partial \overline{\phi_i}}{\partial u_j} = \left(\vec{F} \cdot \frac{\partial}{\partial \vec{v}_i} \right) \overline{\phi_i} \quad (\text{I-3})$$



$$\begin{aligned}
 & + \frac{\partial}{\partial \vec{r}_i} \cdot [\rho_i \vec{u}; \vec{u}] \\
 & + \frac{\partial}{\partial \vec{r}_i} \cdot [\rho_i \vec{u}; \vec{V}_i] \\
 & = \frac{\partial}{\partial \vec{r}_i} \cdot [\rho_i \vec{V}_i; \vec{V}_i] + \frac{\partial}{\partial \vec{r}_i} \cdot [\rho_i \vec{V}_i; \vec{u}] \\
 & = \frac{\partial}{\partial \vec{r}_i} \cdot (\rho_i (\vec{V}_i + \vec{u})(\vec{V}_i + \vec{u})) \\
 & \sum_{j=1}^2 \frac{\partial}{\partial x_j} (N_i \phi_i u_j) = \frac{\partial}{\partial \vec{r}_i} \cdot (N_i (\vec{V}_i + \vec{u}) m_i (\vec{V}_i + \vec{u}))
 \end{aligned}$$

and

$$\frac{\partial}{\partial t} (N_i m_i (\vec{V}_i + \vec{u})) = \frac{\partial}{\partial \vec{r}_i} \cdot (\rho_i (\vec{u} + \vec{V}_i)) \quad (I-5)$$

Thus

$$\phi_i = m_i \vec{V}_i = m_i (\vec{V}_i + \vec{u}) \quad (I-4)$$

For the conservation of momentum

yield the correct result even if ϕ_i is a vector quantity.where the order of \vec{V}_i and ϕ_i given in Equation (I-2) will

135



However since the pressure tensor is

$$[P_i] = [\rho_i \overline{\vec{v}_i} ; \vec{v}_i] \quad (\text{I-7})$$

and

$$\overline{\vec{v}_i} = \vec{U}_i \quad (\text{I-8})$$

Equation (I-6) can be written

$$\begin{aligned} \sum_{j=1}^3 \frac{\partial}{\partial x_j} (N_i \overline{\phi_i u_j}) &= \frac{\partial}{\partial \vec{r}} \cdot [P_i] + \frac{\partial}{\partial \vec{r}} \cdot [\rho_i \vec{v}_i ; \vec{u}] \\ &+ \frac{\partial}{\partial \vec{r}} \cdot [\rho_i \vec{u} ; \vec{v}_i] + \frac{\partial}{\partial \vec{r}} \cdot [\rho_i \vec{u} ; \vec{u}] \end{aligned} \quad (\text{I-9})$$

Likewise since \vec{v}_1 , t , and \vec{r} are independent variables

$$\frac{\partial (m_i \vec{v}_i)}{\partial t} = 0 \quad (\text{I-10})$$

$$\sum_{j=1}^3 \overline{u_j \frac{\partial (m_i \vec{v}_i)}{\partial x_j}} = 0 \quad (\text{I-11})$$

By expressing \vec{F} as \vec{X}_i/m_1 the last term becomes



$$-N_i \left(\frac{\vec{X}_i}{m_i} \cdot \frac{\partial}{\partial \vec{v}_i} \right) m_i \vec{v}_i = -N_i \vec{X}_i \quad (\text{I-12})$$

Thus the species momentum equation can be written

$$\begin{aligned} \frac{\partial}{\partial t} (\rho_i \vec{a}) + \frac{\partial}{\partial t} (\rho_i \vec{v}_i) + \frac{\partial}{\partial \vec{r}} \cdot [\vec{P}_i] + \frac{\partial}{\partial \vec{r}} \cdot [\rho_i \vec{v}_i; \vec{u}] \\ + \frac{\partial}{\partial \vec{r}} \cdot [\vec{u}; \rho_i \vec{v}_i] + \frac{\partial}{\partial \vec{r}} \cdot [\rho_i \vec{u}; \vec{u}] - N_i \vec{X}_i \\ = N_i \Delta \phi_i \end{aligned} \quad (\text{I-13})$$

The various dyadics in this equation can be rewritten using the relationship that

$$\frac{\partial}{\partial \vec{r}} \cdot [\vec{a}; \vec{b}] = \vec{b} \left(\frac{\partial}{\partial \vec{r}} \cdot \vec{a} \right) + \left(\vec{a} \cdot \frac{\partial}{\partial \vec{r}} \right) \vec{b} \quad (\text{I-14})$$

Hence, Equation (I-13) becomes

$$\begin{aligned}
& \rho_i \frac{\partial \vec{u}}{\partial t} + \vec{u} \frac{\partial \rho_i}{\partial t} + \frac{\partial}{\partial t} (\rho_i \vec{U}_i) + \frac{\partial}{\partial \vec{r}} \cdot [\rho_i] + \vec{u} \left(\frac{\partial}{\partial \vec{r}} \cdot \rho_i \vec{U}_i \right) \\
& + \left(\rho_i \vec{U}_i \cdot \frac{\partial}{\partial \vec{r}} \right) \vec{u} + \rho_i \vec{U}_i \left(\frac{\partial}{\partial \vec{r}} \cdot \vec{u} \right) + \left(\vec{u} \cdot \frac{\partial}{\partial \vec{r}} \right) \rho_i \vec{U}_i \\
& + \vec{u} \left(\frac{\partial}{\partial \vec{r}} \cdot \rho_i \vec{u} \right) + \rho_i \left(\vec{u} \cdot \frac{\partial}{\partial \vec{r}} \right) \vec{u} - N_i \vec{X}_i \\
& = N_i \overline{\Delta \phi_i}
\end{aligned} \tag{I-15}$$

Now in general, assuming that the elastic collisions are binary in nature, the volumetric rate of change in average value of some property ϕ_1 can be expressed as

$$N_i \overline{\Delta \phi_i} = N_i \sum_j \Delta_j \overline{\phi_i} \tag{I-16}$$

where $N_i \Delta_j \overline{\phi_i}$ represents the change due to encounters between particles of type i and particles of type j .

According to Chapman and Cowling³⁴ the individual terms of Equation (I-16) can be expressed for elastic collisions as



229

$$N_i \Delta_j \bar{\phi}_i = \iiint (\phi_i' - \phi_i) f_i f_j g b db d\epsilon d\vec{v}_i d\vec{v}_j \quad (I-17)$$

where prime denotes the quantity after collision. The parameters b and ϵ describe the geometry of the encounter, while g is the magnitude of the relative velocity between the two particles. The respective velocity distribution functions are indicated by f_i and f_j . For the momentum equation the elastic portion of the collision term is determined from Equation (I-17) using $\phi_1 = m_1 \vec{V}_1$ and $\phi_1' = m_1 \vec{V}_1'$. The resulting expression will be designated as \vec{P}_{1j} .

Collisions involving charged particles, however, are characterized by small deflections and involve many particles at once. Thus, for electrons and ions the Boltzmann binary collision idea of Equation (I-17) is not strictly applicable. If, on the other hand, this fact is ignored and Equation (I-17) evaluated using an appropriate collision cross section, the result is the same as that obtained by using a more exact treatment such as the Fokker-Planck equation.³⁵ The reason is that the important deflections are small, simultaneous, and random and can be treated as if they were two-body sequential collisions. While this approach does encounter difficulties for like-particle interactions such as electron

[illegible]

self-equilibration, it should be adequate for the present analysis, which considers relaxation between species but assumes self-equilibration to be instantaneous. Now if the species continuity equation is multiplied by \vec{u}

$$\vec{u} \frac{\partial \rho_i}{\partial t} + \vec{u} \left(\frac{\partial}{\partial \vec{r}} \cdot \rho_i \vec{u} \right) + \vec{u} \left(\frac{\partial}{\partial \vec{r}} \cdot \rho_i \vec{U}_i \right) = \dot{w}_i \vec{u} \quad (\text{I-18})$$

then Equation (I-15) becomes

$$\begin{aligned} & \rho_i \frac{\partial \vec{u}}{\partial t} + \rho_i \left(\vec{u} \cdot \frac{\partial}{\partial \vec{r}} \right) \vec{u} + \frac{\partial}{\partial t} (\rho_i \vec{U}_i) + \left(\vec{u} \cdot \frac{\partial}{\partial \vec{r}} \right) \rho_i \vec{U}_i \\ & + \frac{\partial}{\partial \vec{r}} \cdot [\vec{P}_i] + \rho_i \vec{U}_i \left(\frac{\partial}{\partial \vec{r}} \cdot \vec{u} \right) + \rho_i \left(\vec{U}_i \cdot \frac{\partial}{\partial \vec{r}} \right) \vec{u} - N_i \vec{X}_i \\ & + \dot{w}_i \vec{u} = \sum_j \vec{P}_{ij} + \vec{J}_i \end{aligned} \quad (\text{I-19})$$

where the collision term has been represented by two parts -- one part representing effects due to elastic collisions and one part for inelastic collisions.

By defining

$$\frac{D}{Dt} = \frac{\partial}{\partial t} + \vec{u} \cdot \frac{\partial}{\partial \vec{r}} \quad (\text{I-20})$$



243

Equation (I-19) becomes identical with Equation (4) in Chapter II.

For the species energy equation the suitable property function is

$$\phi = \frac{1}{2} m_i v_i^2 = \frac{1}{2} m_i (\vec{v}_i + \vec{u})^2 \quad (\text{I-21})$$

where the first term in Equation (I-1) becomes

$$\frac{\partial}{\partial t} (N_i \overline{\phi_i}) = \frac{\partial}{\partial t} \left(\frac{1}{2} N_i \overline{m_i v_i^2} \right) = \frac{\partial}{\partial t} \left(\frac{1}{2} N_i m_i \overline{v_i^2} \right) \quad (\text{I-22})$$

$$+ \frac{\partial}{\partial t} (N_i m_i \overline{\vec{v}_i \cdot \vec{u}}) + \frac{\partial}{\partial t} (N_i \frac{1}{2} m_i \overline{u^2})$$

By definition

$$e_i = \overline{\frac{1}{2} v_i^2} \quad (\text{I-23})$$

so that

$$\frac{\partial (N_i \overline{\phi_i})}{\partial t} = \frac{\partial}{\partial t} (\rho_i e_i) + \frac{\partial}{\partial t} (\rho_i \vec{U}_i \cdot \vec{u}) + \frac{1}{2} \frac{\partial}{\partial t} (\rho_i u^2) \quad (\text{I-24})$$



The second term is

$$\begin{aligned} \frac{\partial}{\partial \vec{r}} \cdot (N_i \vec{v}_i \phi_i) &= \frac{\partial}{\partial \vec{r}} \cdot \left[N_i \vec{v}_i \frac{1}{2} m_i \overline{v_i^2} \right] \\ &+ \frac{\partial}{\partial \vec{r}} \cdot \left(m_i N_i \vec{v}_i (\overline{\vec{v}_i \cdot \vec{u}}) \right) + \frac{\partial}{\partial \vec{r}} \cdot \left(N_i \vec{v}_i \frac{1}{2} m_i \overline{u^2} \right) \end{aligned} \quad (\text{I-25})$$

By using the relationships

$$\vec{a} (\vec{b} \cdot \vec{c}) = \vec{c} \cdot (\vec{b}; \vec{a}) \quad (\text{I-26})$$

$$\vec{q}_i = \frac{1}{2} \rho_i \overline{v_i^2} \vec{v}_i \quad (\text{I-27})$$

this term becomes

$$\begin{aligned} \frac{\partial}{\partial \vec{r}} \cdot (N_i \vec{v}_i \phi_i) &= \frac{\partial}{\partial \vec{r}} \cdot \vec{q}_i + \frac{\partial}{\partial \vec{r}} \cdot (\rho_i \vec{e}_i \vec{u}) + \frac{\partial}{\partial \vec{r}} \cdot (\vec{u} \cdot [\rho_i]) \\ &+ \frac{\partial}{\partial \vec{r}} \cdot (\rho_i \vec{u} \cdot (\vec{v}_i; \vec{u})) + \frac{\partial}{\partial \vec{r}} \cdot \left(\frac{1}{2} \rho_i u^2 \vec{u}_i \right) \end{aligned} \quad (\text{I-28})$$

As in the case of the species momentum equation the third and fourth terms are zero because \vec{v}_1 , \vec{r} , and t are independent variables. The last term on the left-hand side of Equation (I-1) becomes

—

$$-N_i (\vec{F}_i \cdot \overline{\frac{\partial}{\partial \vec{v}_i}}) \phi_i = -N_i (\frac{\vec{X}_i}{m_i} \cdot \overline{\frac{\partial}{\partial \vec{v}_i}}) (\frac{1}{2} m_i v_i^2)$$

(I-29)

$$= -N_i \vec{X}_i \cdot \vec{U}_i - N_i \vec{X}_i \cdot \vec{u}$$

In this manner the species energy equation becomes

$$\frac{\partial}{\partial t} (\rho_i e_i) + \frac{\partial}{\partial t} (\rho_i \vec{U}_i \cdot \vec{u}) + \frac{1}{2} \frac{\partial}{\partial t} (\rho_i u^2) + \frac{\partial}{\partial \vec{r}} \cdot \vec{q}_i$$

$$+ \frac{\partial}{\partial \vec{r}} \cdot (\rho_i e_i \vec{u}) + \frac{\partial}{\partial \vec{r}} \cdot (\vec{u} \cdot [\rho_i]) + \frac{\partial}{\partial \vec{r}} \cdot (\rho_i \vec{u} \cdot (\vec{U}_i; \vec{u}))$$

(I-30)

$$+ \frac{\partial}{\partial \vec{r}} \cdot (\frac{1}{2} \rho_i u^2 \vec{u}) - N_i \vec{X}_i \cdot \vec{U}_i - N_i \vec{X}_i \cdot \vec{u}$$

$$= E_i$$

where E_i is used to represent the change in energy due to collisions. Now by using the fact that

$$\frac{\partial}{\partial \vec{r}} \cdot [\vec{u} \cdot [\rho_i]] = [\frac{\partial}{\partial \vec{r}} ; \vec{u}] : [\rho_i]$$

(I-31)

$$+ \vec{u} \cdot [\frac{\partial}{\partial \vec{r}} \cdot [\rho_i]]$$

and using the specie momentum equation to eliminate $N_i \vec{X}_i \cdot \vec{u}$,
the energy equation becomes (also use species continuity)



$$\begin{aligned}
& \frac{D}{Dt} (\rho_i e_i) + \frac{\partial}{\partial \vec{r}} \cdot \vec{q}_i + \rho_i e_i \left(\frac{\partial}{\partial \vec{r}} \cdot \vec{u} \right) + \rho_i \vec{U}_i \cdot \frac{D\vec{u}}{Dt} \\
& + \left[\frac{\partial}{\partial \vec{r}} \cdot \vec{u} \right] : [\rho_i] - N_i \vec{X}_i \cdot \vec{U}_i = E_i - \vec{u} \cdot \sum \vec{P}_{ij} \\
& + \dot{W}_i \frac{u^2}{2}
\end{aligned} \tag{I-32}$$

For the energy equation, Equation (I-17) yields for elastic collisions

$$N_i \Delta_j \bar{\phi}_i = \iiint \int \frac{1}{2} m_i (v_i'^2 - v_i^2) f_i f_j g b db d\epsilon d\vec{v}_i d\vec{v}_j \tag{I-33}$$

This equation can be divided into two terms as follows

$$\begin{aligned}
N_i \Delta_j \bar{\phi}_i = & \iiint \int \frac{1}{2} m_i \{ (\vec{v}_i' - \vec{u}_i)^2 - (\vec{v}_i - \vec{u}_i)^2 \} f_i f_j g b db d\epsilon d\vec{v}_i d\vec{v}_j \\
& + \vec{u}_i \cdot \left[\iiint \int m_i (\vec{v}_i' - \vec{v}_i) f_i f_j g b db d\epsilon d\vec{v}_i d\vec{v}_j \right]
\end{aligned} \tag{I-34}$$

where the first term represents the rate of energy gain by species i due to elastic encounters between species i and j because of thermal motion of the particles. The second part represents the rate at which work is done on species i due to elastic interactions between species i and j because of directed motion of the particles. In this work the first term will be denoted as $\dot{\mathcal{E}}_{ij}$ and the second as



$\vec{u}_i \cdot \vec{p}_{ij}$. Hence

$$E_i = \sum_j \xi_{ij} + \vec{u}_i \cdot \sum_j \vec{p}_{ij} + Q_i \quad (\text{I-35})$$

where the last term represents energy change due to elastic collisions.

Then breaking up the pressure tensor as

$$[P_i] = p_i [I] + [\gamma_i] \quad (\text{I-36})$$

and expressing internal energy in terms of enthalpy

$$e_i = h_i - p_i/\rho_i \quad (\text{I-37})$$

Equation (I-32) becomes

$$\begin{aligned} & \frac{D}{Dt} (\rho_i h_i) - \frac{D p_i}{Dt} + \frac{\partial}{\partial r} \cdot \vec{q}_i + \rho_i h_i \left(\frac{\partial}{\partial r} \cdot \vec{u} \right) \\ & + \rho_i \vec{U}_i \cdot \frac{D \vec{u}}{Dt} + [\gamma_i] : \left[\frac{\partial}{\partial r} ; \vec{u} \right] - N_i \vec{X}_i \cdot \vec{U}_i \\ & = \sum_j \xi_{ij} + \vec{U}_i \cdot \sum_j \vec{p}_{ij} + Q_i + \dot{W}_i \frac{u^2}{2} \end{aligned} \quad (\text{I-38})$$





